On the coexistence of Landau levels and superconductivity

Pacholski, M.J.

On the coexistence of Landau levels and superconductivity

Proefschrift

ter verkrijging van
de graad van doctor aan de Universiteit Leiden,
op gezag van rector magnificus prof. dr. ir. H. Bijl,
volgens besluit van het college voor promoties
te verdedigen op donderdag 30 september 2021
klokke 11.15 uur

door

Michał Jan Pacholski

geboren te Otwock (Polen) in 1993

Promotores:	Prof. dr. C. W. J. Beenakker
	Prof. dr. İ. Adagideli (Sabancı University, Istanbul)
Promotiecommissie:	Prof. dr. M. Franz (University of British Columbia, Vancouver, Canada)
	Prof. dr. F. Hassler (RWTH Aachen University, Aachen, Duitsland)
	Prof. dr. E. R. Eliel
	Prof. dr. ir. S. J. van der Molen
	Dr. A. Silvestri

Casimir PhD series, Delft-Leiden 2021-19
ISBN 978-90-8593-485-1
An electronic version of this thesis can be found
at https://openaccess.leidenuniv.nl

Cover: a watercolor painting of northern lights over an arctic landscape by Yevheniia Cheipesh. The northern lights, produced by charged particles swirling in the Earth's magnetic field, are depicted to form a striped pattern, resembling the density of a Landau level produced by electrons in the magnetic field in a two-dimensional topological superconductor (Fig. 5.4).

To my Mom, my Grandparents, and all my Family.

Contents

1 Introduction

1.1 Preface

Quantum states of electrons in a strong magnetic field are massively degenerate Landau levels – the quantized cyclotron orbits. Their presence results in many important phenomena, the most striking of which is the quantum Hall effect: accurate to an extraordinary precision quantization of the Hall conductance in the units of e^2/h.

In the presence of superconductivity, the formation of Landau levels is hindered, as the magnetic field is repelled from a superconductor as a result of the Meissner effect. It is possible for the magnetic field to penetrate the superconductor in the case of type-II superconductors. Then, however, the magnetic field is accompanied by supercurrents circulating around the Abrikosov vortices. In the case of the d-wave superconductors – an unconventional type of gapless superconductors which is postulated to encompass the high temperature superconductors – it was shown that these supercurrents spoil the degeneracy of the Landau levels, transforming them into dispersive magnetic Bloch bands [1–11]. In this thesis we consider a different kind of gapless superconductors: Weyl superconductors, which are formed when conventional s-wave superconductivity occurs in Weyl semimetals [12, 13]. We show that the chiral symmetry present in such systems gives rise to a zeroth Landau level, which persists even in the presence of the Abrikosov vortices. We study the properties of this superconducting Landau level. One of them is the universal chiral magnetic effect in equilibrium. It is a signature of the topological properties of the Weyl fermion that can only be accessed in the Weyl superconductors, as it requires the presence of a non-vanishing equilibrium current, which is forbidden in the absence of superconductivity.

We also study a different type of superconductors, which arises when superconductivity is induced in the surface states of topological insulators – the Fu-Kane model [14]. Under certain circumstances, the excitation of such a system can also become gapless, which was recently demonstrated experimentally [15]. This system also possesses chiral symmetry, which, like in the Weyl superconductor, gives rise to a topologically protected

zeroth Landau level, which is not spoiled by the vortices.

The cases above, discussed in detail in this thesis, are the first instances of the coexistence of Landau levels and superconductivity. They open up a path to a new range of possible effects that are only possible due to a combination of these two phenomena. In the remainder of this chapter we will introduce the basic concepts, which lie at the foundations of the results presented afterwards.

1.2 Landau levels

1.2.1 Particles in a magnetic field

When a charged particle is moving through a uniform magnetic field B, and its velocity v is perpendicular to the direction of the field, it follows the circular trajectory of a cyclotron orbit of radius

$$l_c = \frac{mv}{qB}\,, \tag{1.1}$$

where $q > 0$ is the particle's charge and m is its mass. If the particle is simultaneously moving parallel to the magnetic field, its motion in that direction is unaffected. As a result, the particle's trajectory will be a helix oriented along the magnetic field – Fig. 1.1. This phenomenon has striking consequences: for instance, when a charged particle coming from the Sun as a part of the solar wind reaches the Earth's magnetosphere, it is forced to follow the helical trajectory along the lines of the magnetic field, which guide it towards the Earth's poles. This provides the inhabitants of the Earth protection from the harmful effects of space radiation, as well as a marvelous spectacle of light produced once particles' motion is interrupted by the Earth's atmosphere.

This periodic cyclotron motion carries on to the lowest-level description of reality: quantum physics. There, however, due to the wave-like nature of particles, not all sizes of their orbits are permitted. The phase of a particle's wave must change by an integer multiple of 2π upon completion of one cycle, which puts a constraint that only allows orbits with energies equal to

$$E_n = \hbar\omega_c\left(n + \frac{1}{2}\right), \quad n = 0, 1, 2, \ldots \tag{1.2}$$

where $\omega_c = v/l_c = qB/m$ is the cyclotron frequency. The quantum states corresponding to these orbits are called the Landau levels. Noticeably,

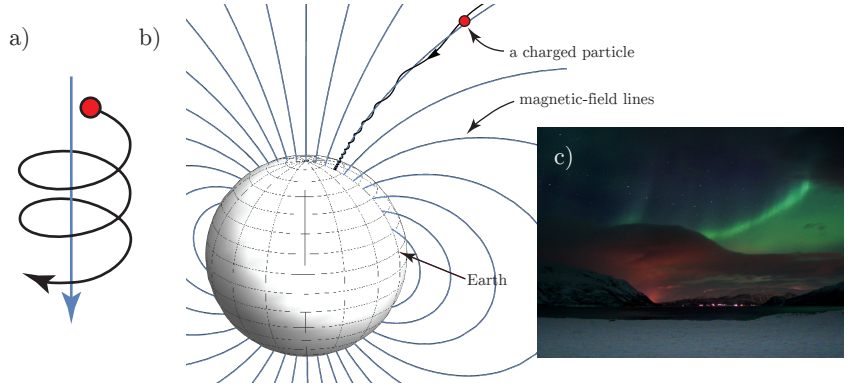

Figure 1.1: a) Trajectory of a charged particle in a uniform magnetic field, the direction of which is indicated by the blue arrow. The particle, represented as a red dot, can propagate freely along the magnetic field, however its motion in the perpendicular direction is confined. b) Trajectory of a charged particle in the Earth's magnetic field. The particle follows a helical path along the magnetic-field lines, until it reaches the atmosphere in the polar regions, where its kinetic energy is converted into radiation, producing the aurora. c) Picture of an aurora in Norway, taken by the author.

the lowest energy allowed for a particle $E_0 = \hbar\omega_c/2$ is greater than zero. This can be understood as the particle's zero-point motion.

The classical orbits can be centered at any point in the region of applied magnetic field. In a quantum case, this means that there are multiple states at each energy E_n. Their number, known as the degeneracy of a given energy level, is limited by the requirement that different quantum states must be orthogonal, and equals

$$\mathcal{N} = \frac{\Phi}{\Phi_0}\,, \tag{1.3}$$

where Φ is the total flux of applied magnetic field, and $\Phi_0 = h/q$ is the magnetic flux quantum.

As in the classical case, the motion of a particle parallel to the field remains unaffected. This manifests itself in a relation between the particle's momentum in that direction $p_\parallel$ and its energy, given by

$$E_n(p_\parallel) = \hbar\omega_c\left(n + \frac{1}{2}\right) + \frac{p_\parallel^2}{2m}\,, \tag{1.4}$$

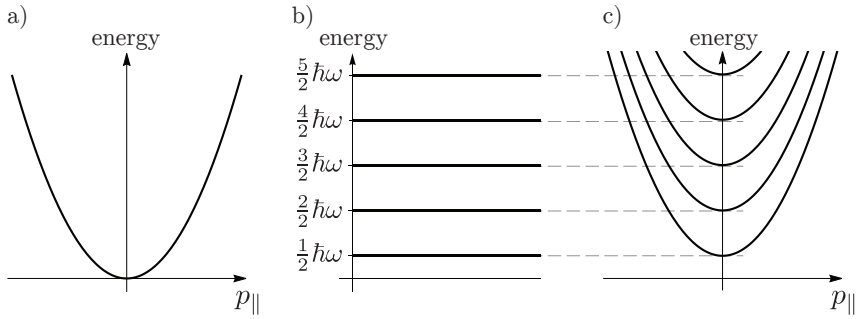

Figure 1.2: a) Dispersion relation of a free non-relativistic massive particle. b) Energies of the Landau levels at $p_\parallel = 0$. c) Dispersion relation of the Landau levels in the direction parallel to the magnetic field.

which is simply a sum of the energy of the Landau level, and the kinetic energy of motion in the direction parallel to the magnetic field – Fig. 1.2.

The group velocity of a particle equals to the derivative of its energy with respect to its momentum in the direction of motion. For the nth Landau level it then equals

$$v_n(p_\parallel) = \frac{\mathrm{d}E_n(p_\parallel)}{\mathrm{d}p_\parallel} = \frac{p_\parallel}{m}\,, \tag{1.5}$$

which is a result familiar from classical physics. Unsurprisingly, as the velocity can be positive or negative, depending on the sign of momentum $p_\parallel$, the particle is free to propagate in either direction along the magnetic field, however, as it will be shown in Sec. 1.2.4, this property should not be taken for granted.

1.2.2 Weyl semimetal

In this thesis, we will consider a more exotic type of particles: Weyl fermions. They are massless relativistic particles. Unlike massive non-relativistic particles, whose energy is given by $E = |\boldsymbol{p}|^2/2$, their dispersion relation reads

$$E(\boldsymbol{p}) = \pm v_\mathrm{F}|\boldsymbol{p}|\,, \tag{1.6}$$

similar to that of a photon. v_F is the Fermi velocity, and $\boldsymbol{p}$ is the three-component momentum vector. This dispersion relation forms a three-dimensional double cone in the energy-momentum space, called a Weyl cone. Such particles are the basic building blocks of the Standard Model

(in which case v_F is the speed of light), however, they are not found among fundamental particles, as the spontaneous symmetry breaking introduces coupling between different flavors of Weyl fermions, which gives rise to emergent particles of a different type – massive Dirac fermions[1].

Luckily, Weyl fermions can also be found as low-energy electronic excitations in certain types of materials: Weyl semimetals, which allows for an experimental study of their properties. In the following paragraphs, I will explain how this can happen. An electron propagating in a material undergoes scattering off the electrostatic potential of the crystalline lattice, thus its momentum is not conserved. However, due to the periodic structure of the lattice, a similar quantum number $\boldsymbol{k}$, called the quasi-momentum, is conserved. For each value of the quasi-momentum, the energy of an electron can take one of the enumerably many values $E_n(\boldsymbol{k})$, where n is called the band index. As a result, the set of all allowed energy values is split into energy bands labeled by n, which lies at the foundations of the electronic band theory – the basic tool for describing the vast majority of solid-state devices.

Typically, the energy bands are separated – if two of them are accidentally crossing at some values of $\boldsymbol{k}$, generally a perturbation to the system will make these crossings avoided. This, however, may not be the case if two bands are touching in an isolated point $\boldsymbol{k}_0$ in the quasi-momentum space. It can turn out that for quasi-momenta near $\boldsymbol{k}_0$ and up to a constant energy shift, the energies of the two bands touching are given by the relativistic dispersion relation of Eq. (1.6) with $\boldsymbol{p} = \boldsymbol{k} - \boldsymbol{k}_0$. Then the electronic excitations with energy and momentum close to the touching point, in this case called the Weyl point, are Weyl fermions.

The effective low-energy Hamiltonian that leads to the Weyl dispersion relation is

$$H = \chi v_\mathrm{F} \boldsymbol{p} \cdot \boldsymbol{\sigma}\,, \tag{1.7}$$

where $\boldsymbol{\sigma} = (\sigma_x, \sigma_y, \sigma_z)$ is the pseudo-spin operator, and $\chi \in \{+1, -1\}$ is called chirality. Apart from their unusual dispersion relation, the Weyl fermions have the property that they are topologically protected: there is no perturbation that can be added to the Hamiltonian (1.7) that will open an energy gap between the two bands that are touching. The only effect that a perturbation can have is to change the position of the Weyl point, or add anisotropy or tilting to the Weyl cone.

It is only possible to gap out a Weyl cone, if a pair of Weyl cones of opposite chirality occurs at a single point in the quasi-momentum space.

[1] An exception to this are the neutrinos, for which the origin of mass is currently unknown.

A situation like this is captured by a Hamiltonian

$$H = v_{\mathrm{F}} \tau_z \boldsymbol{p} \cdot \boldsymbol{\sigma} \,, \tag{1.8}$$

where τ_z is a Pauli matrix that distinguishes between the two Weyl fermions. Then, a perturbation $m\tau_x\sigma_0$ opens a gap of width $2m$, and the dispersion becomes

$$E(\boldsymbol{p}) = \pm v_{\mathrm{F}} \sqrt{m^2 + \boldsymbol{p}^2} \,, \tag{1.9}$$

which is that of a massive relativistic particle.

Another important property of a Weyl fermion is that its spin must always be oriented along its momentum – a phenomenon known as spin-momentum locking. In the context of a relativistic field theory it originates from the Lorentz invariance: the co-linear arrangement of spin and momentum is the only one that does not depend on the frame of reference. (Pseudo-)spin momentum-locking also applies to Weyl fermions in condensed-matter systems, even though the Lorentz invariance there is emergent and can be broken by perturbations. The universality of this phenomenon arises from the form of the Weyl Hamiltonian (1.7), which also determines the character of the spin-momentum locking, depending on the chirality χ: for $\chi = +1$ the spin and the momentum of a positive-energy Weyl fermion point in the same, while for $\chi = -1$ in the opposite direction.

1.2.3 Zeroth Landau level

Now we will turn our attention to the behavior of a Weyl fermion in the presence of the magnetic field. The classical picture is similar to that for a non-relativistic particle – the Lorentz force exerted on a moving Weyl fermion guides it along a circular, or helical, trajectory. The only difference is that in the expression for the radius of such trajectory, given in Eq. (1.1), the product mv must be replaced with the momentum component perpendicular to the magnetic field $p_\perp$, as the Weyl fermion is a massless particle.

When quantum mechanics is taken into account, however, the differences become more significant: as a result of the spin-momentum locking, when a Weyl fermion follows a closed cyclotron orbit and its velocity – and with it the quasi-momentum – makes a 360° rotation, so does its pseudo-spin. A full rotation of a spin-1/2 particle changes the phase of its wave by π. The same holds for the pseudo-spin. This results in a change in the wave-matching condition for the Landau level, with which

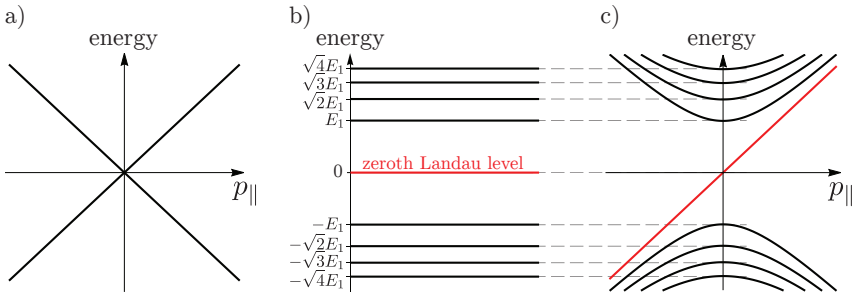

Figure 1.3: a) Dispersion relation of a Weyl fermion. b) Energies of the Landau levels at $p_\parallel = 0$. c) Dispersion relation of the Landau levels in the direction parallel to the magnetic field.

the quantized energy levels become

$$E_n = \mathrm{sign}(n) v_\mathrm{F} \sqrt{2e\hbar B|n|}\,, \qquad n \in \mathbb{Z}\,, \tag{1.10}$$

where we took $q = e$, the charge of an electron. The allowed energies are no longer just positive. This is a result of the fact that the Weyl cone extends to both positive and negative energies. Central to the work presented in this thesis is the $n = 0$ state, known as the zeroth Landau level, whose energy is exactly equal to zero (with respect to the Weyl point). Its apparent lack of zero-point motion is the direct effect of the spin-momentum locking discussed earlier. The zeroth Landau level is special – it is robust against a wide class of perturbations [16]. For instance, while for other Landau levels an inhomogeneity of the magnetic field results in a broadening of their energy band, the states in the zeroth Landau level remain all at zero energy. The cause of this is rooted in the topological nature of the Weyl fermion and is a consequence of the Atiyah-Singer index theorem [17].

1.2.4 Chiral anomaly

When the motion along the magnetic field is considered, the peculiarities of the zeroth Landau level become even more pronounced. The energies of the particle are then given by

$$E_n(p_\parallel) = \mathrm{sign}(n) v_\mathrm{F} \sqrt{2e\hbar B|n| + p_\parallel^2}\,, \qquad n \in \mathbb{Z} \setminus \{0\}\,. \tag{1.11}$$

and

$$E_0(p_\parallel) = \chi v_\mathrm{F} p_\parallel\,, \tag{1.12}$$

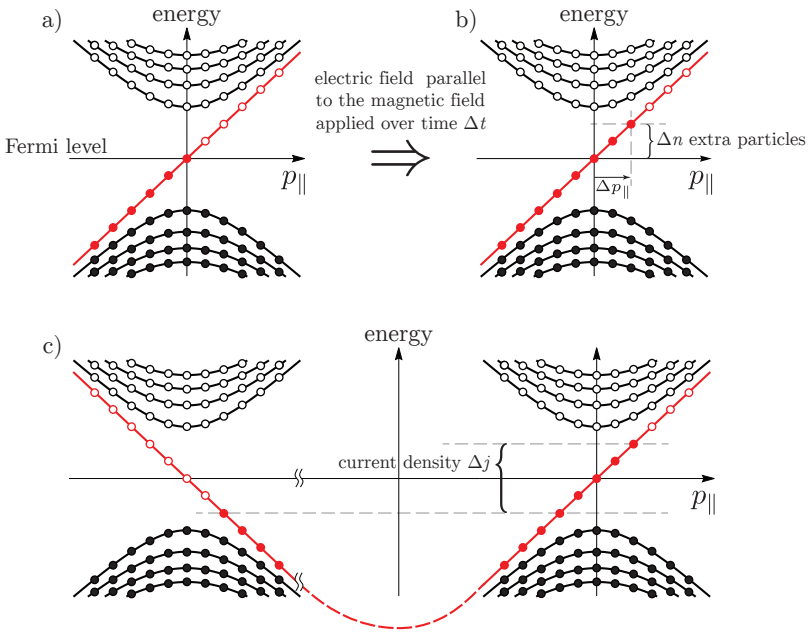

Figure 1.4: a) The distribution of electrons in the Landau levels of a Weyl fermion in the ground state. The filled circles represent states occupied by electrons, whereas the empty circles – unoccupied states. In the ground state all the states up the Fermi level are occupied and all those above it – empty. The velocity of each electron is given by the slope of the dispersion relation of the Landau level it lies in. For all but the zeroth Landau level, the current carried by electrons with positive velocity is cancelled by the current carried by electrons with negative velocity, resulting in zero net current. However, all the electrons in the zeroth Landau level are moving in the same direction, resulting in an infinite ground-state current. b) The distribution of electrons after applying a pulse of electric field parallel to the magnetic field over time Δt. Each electron acquires an additional momentum $\Delta p_\parallel$, which makes some of the previously unoccupied states, occupied. This produces a certain number of extra particles, violating the particle conservation – a phenomenon known as the chiral anomaly. c) A resolution to the lack of particle conservation 'paradox' in a Weyl semimetal. Each Weyl cone with chirality $+1$ is accompanied by a cone with chirality -1. When a certain number of electrons is produced in one of the Weyl cones, due to chiral anomaly, the same number vanishes from the other Weyl cone, ensuring total particle conservation. This results in a unequal number of left- and right-moving electrons, which produces a non-vanishing current density Δj. The appearance of this current is known as the chiral magnetic effect.

which means that the zeroth Landau level can only propagate in one direction along the magnetic field, depending on its chirality χ – Fig. 1.3. This has two puzzling consequences. Firstly, such a dispersion relation leads to an infinite current in the ground state: at zero temperature, electrons occupy all the lowest-energy states up to a certain energy, called the Fermi level. Then for all Landau levels with $n \neq 0$, at each energy there is the same number of electrons propagating in either direction along the magnetic field, thus the net current they carry vanishes. All the electrons in the zeroth Landau level, however, propagate in the same direction, so their total contribution to the current diverges. In quantum field theories, diverging ground-state (also called the vacuum in this context) properties, such as energy or charge density, are not unusual. A common practice is to define all the observables with respect to the vacuum, by subtracting their – possibly infinite – vacuum expectation values. In the condensed-matter context, however, there is no such freedom, as the ground state properties are directly accessible experimentally. The non-vanishing ground-state current thus constitutes a contradiction as it is not allowed by the Bloch theorem[2] [18–21].

A second problem arises when, in addition to the magnetic field, an electric field $\boldsymbol{\mathcal{E}}$ is applied in the same direction for some finite time Δt. It will exert a force $\boldsymbol{F} = e\boldsymbol{\mathcal{E}}$ on each electron, which will change its momentum by $\Delta p_{\parallel} = e\mathcal{E}\Delta t$. If the Fermi level was originally between the $n = -1$ and $n = 1$ Landau levels, it will effectively shift by $\Delta\mu = \chi v_{\mathrm{F}} e\mathcal{E}\Delta t$, which implies that the number of particles in the system will change. This change is equal to

$$\Delta n = \chi \frac{e\mathcal{E}\Delta t}{h/L} \frac{\Phi}{\Phi_0} = \chi \frac{e^2}{h^2} \boldsymbol{\mathcal{E}} \cdot \boldsymbol{B} V \Delta t \,, \tag{1.13}$$

where V is the total volume of the system [55]. This violation of particle-number conservation is known as the chiral anomaly. In particle physics, the chiral anomaly affects the decay rate of the neutral pion π^0, which was first explained by Adler [22], and Bell and Jackiw [23]. In the condensed-matter context, however, the Weyl fermions arise from ordinary electrons, the number of which must be conserved, which, once again, leads to a contradiction.

The resolution to both of the issues discussed above is the same: in the electronic band structure of a material, there must always be an even number of Weyl points, and the number of those with $+1$ chirality must be equal to those with -1 chirality. In that case the ground-state current

[2] The theorem allows for persistent currents, however their magnitude vanishes in the thermodynamic limit.

carried by the electrons in the zeroth Landau level of the Weyl fermions with $+1$ chirality is canceled by that of the Weyl fermions with -1 chirality, in agreement with the Bloch theorem – Fig. 1.4. In the same way, the total change of the number of electron due to the chiral anomaly for all the Weyl fermions is zero, as expected: the electric field simply pumps the electrons from one Weyl fermion to the other.

1.2.5 Chiral magnetic effect

Even though the total number of electrons is conserved, the chiral anomaly can still lead to observable consequences, as it creates an imbalance between the Weyl fermions of opposite chiralities. Since the current carried by electrons in the zeroth Landau level depends on its chirality, such imbalance produces an electric current. This phenomenon is known as the chiral magnetic effect (CME). For each Weyl fermion, the resulting current density is equal to

$$\Delta j = \chi \frac{e^2}{h} \Delta\mu \,, \tag{1.14}$$

where the proportionality coefficient only depends on the fundamental constants: e – the elementary charge, and h – the Planck's constant. This independence of any details of the system is a case of universality. Universal responses are often found in systems with topological properties. The most prominent example of such a response is the quantized Hall conductance in the quantum Hall effect, which, similarly, assumes values of integer multiples of e^2/h – independent of the sample. The accuracy of this result lead to establishing a new definition of the kilogram in 2019, based on the value of Planck's constant, rather than a physical artifact.

Unfortunately, the chiral magnetic effect – a universal response of the Weyl semimetal – is difficult to access: the electric field applied brings the system out of equilibrium – a state, which must decay once the electric field is removed, due to random scattering processes. In order to maintain the imbalance of chiralities, the electric field must be applied continuously, which keeps the system in a steady state in which the rate of scattering between the Weyl cones balances out the pumping of electrons. Then, if the characteristic relaxation time associated with this scattering is τ, the current density contribution of a single Weyl cone can be shown to be

$$\Delta j = \chi v_F \frac{e^3}{h^2} \boldsymbol{\mathcal{E}} \cdot \boldsymbol{B} \tau \,. \tag{1.15}$$

This results in an appearance of negative magnetoresistance in Weyl semimetals – an increase in conductance proportional to the applied magnetic

field, regarded as the basic transport signature of Weyl fermions in condensed matter systems [24, 25]. It has been demonstrated experimentally in agreement with the presented theory [26, 27]. In this phenomenon, however, the universality of CME becomes obscured, as the observed effect depends on the relaxation time τ, which is an effective parameter depending on the microscopic details of the system.

1.3 Superconductivity

1.3.1 Bogoliubov-de Gennes formalism

In normal materials the electric current must vanish in equilibrium, which prevents the access to the chiral magnetic effect in such a situation. Superconductors, however, can support a non-vanishing current in equilibrium. This opens a tantalizing possibility that in such systems the equilibrium CME can be accessed. It would then allow for a direct observation of the universal coefficient e^2/h of Eq. (1.14). This possibility was the main motivation for the work presented in this thesis.

To demonstrate how it can happen, I will first explain the effect of superconductivity on Weyl semimetals. In the ground state of a superconductor, the electrons form a condensate of Cooper pairs, which allows for a frictionless flow of the current. The presence of the condensate modifies the dynamics of excitations in a superconductor: if energy is supplied to the system, a Cooper pair can split into two independent electrons. A converse process is also possible, in which two electrons combine and form a Cooper pair, which becomes a part of the condensate. In the simplest case, a Cooper pair consists of two electrons of opposite quasi-momenta and spin. This is the case in the s-wave superconductors. In the mean-field approximation, these processes are captured by the Bogoliubov-de Gennes (BdG) formalism, in which the number of degrees of freedom is doubled: in addition to electrons, one introduces new particles – holes. Then, for an s-wave superconductor, a given state of the system can be represented in two ways: the electron at energy E (with respect to the Fermi level), quasi-momentum $\boldsymbol{k}$ and spin $\boldsymbol{s}$, is equivalent to the absence of a hole at energy $-E$, quasi-momentum $-\boldsymbol{k}$ and spin $-\boldsymbol{s}$. With this redundancy, a multi-particle process of a decay of a Cooper pair, which results in the creation of two electrons of opposite quasi-momenta and spins, is equivalently described as a scattering process of a hole at quasi-momentum $\boldsymbol{k}$ and spin $\boldsymbol{s}$ into an electron with the same quasi-momentum and spin, which is a single-particle process – Fig. 1.5. In this formal-

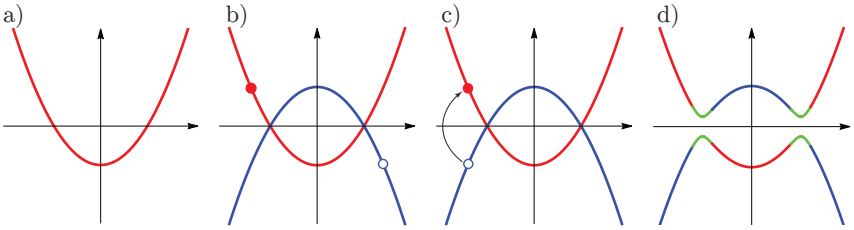

Figure 1.5: a) Dispersion relation of an electron in a normal material. b) Dispersion relation for a normal material in the BdG formalism: dispersion relation of an electron is in red, and that of a hole is in blue. Electron at energy E, quasi-momentum $\boldsymbol{k}$ and spin $\boldsymbol{s}$ (marked by a red dot), can be equivalently described as absence of a hole at energy $-E$, quasi-momentum $-\boldsymbol{k}$ and spin $-\boldsymbol{s}$ (marked by a blue circle). c) Decay of a Cooper pair: a hole at quasi-momentum $\boldsymbol{k}$ and spin $\boldsymbol{s}$ is scattered into an electron with the same quasi-momentum and spin. d) Resulting dispersion relation of a superconductor, given by Eq. (1.18)

ism, the dynamics of the system is captured by a single-body Bogoliubov de-Gennes Hamiltonian

$$\mathcal{H}(\boldsymbol{k}) = \begin{pmatrix} H_0(\boldsymbol{k}) & \Delta \\ \Delta^\dagger & -s_y H_0^*(-\boldsymbol{k}) s_y \end{pmatrix}, \tag{1.16}$$

where the top block describes the behavior of electrons, the bottom block that of the holes and Δ – the superconducting pairing – introduces the scattering between them induced by the Cooper pair condensate. Operator s_y is the Pauli matrix acting on the spin.

1.3.2 Weyl superconductor

Typically, the superconducting pairing induces an energy gap in the system. For instance, if an electron is described by a simple quadratic Hamiltonian

$$H_0 = \frac{k^2}{2m} - \mu\,, \tag{1.17}$$

the BdG Hamiltonian results in the dispersion

$$E = \pm\sqrt{\left(\frac{k^2}{2m^*} - \mu\right)^2 + \Delta^2}\,, \tag{1.18}$$

which is gapped. This gap is in fact a crucial feature of the superconductors, as the lack of low-energy excitations means that they cannot

participate in the dissipation of energy, which suppresses the production of heat when the current is passing through the system.

However, if the superconducting pairing is present in a Weyl semimetal, in which case the system is dubbed a Weyl superconductor [12, 13], the appearance of such a gap can be generally avoided. This is due to the topological protection of the Weyl cones. As explained in Sec. 1.2.2, it is only possible for a small perturbation to open a gap of a Weyl cone if there are two Weyl cones of opposite chirality at the same quasi-momentum $\boldsymbol{k}_0$. In the BdG formalism, the band structure is doubled, thus additional Weyl cones appear originating from the dispersion relation of the holes. A hole Weyl cone at quasi-momentum $\boldsymbol{k}_0$ with chirality χ appears as a redundant representation of an electronic Weyl cone at quasi-momentum $-\boldsymbol{k}_0$ and chirality $-\chi$. Thus, in the BdG formalism, two Weyl cones of opposite chirality – one for electron and one for hole – occur at the same quasi-momentum, in which case a small superconducting pairing can open a gap, only if two Weyl cones of the same chirality occur at opposite quasi-momenta, $\boldsymbol{k}_0$ and $-\boldsymbol{k}_0$, in the original electronic band structure of a Weyl semimetal. Such a configuration requires either fine-tuning, or the presence of certain symmetry – in this case time-reversal symmetry, combined with a broken inversion symmetry. Thus, generically the band structure of a Weyl superconductor remains gapless.

In normal materials, the current from CME vanishes in equilibrium, because there is the same number of Weyl cones of each chirality. Then, if the chemical potential is changed by $\Delta\mu$, it changes by the same amount for all the Weyl cones, and the contributions – given by Eq. (1.14) – from the Weyl cones of opposite chiralities cancel out. If the superconducting pairing fails to open a gap of any of the Weyl cones in the Weyl superconductor, the situation is the same there. However, as explained before, a gap can open for a given electronic Weyl cone at momentum $\boldsymbol{k}_0$, if there also exists another one with the same chirality at the opposite momentum. The superconducting pairing then opens a gap in both of these two Weyl cones simultaneously. Alternatively, a gap can also open for a single Weyl cone, if it occurs at $\boldsymbol{k}_0 = 0$. Such a gap is analogous to the Majorana mass in the high-energy physics context. In either of these situations, the number of Weyl fermions of a single chirality is reduced – by either 2 or 1, depending on the number of Weyl cones involved. While for an infinitesimal Δ such a case is only possible with fine-tuning, it is not so when Δ is finite – the regime with an unequal number of Weyl fermions with different chiralities occurs in finite regions in the parameter space. In such a regime then, if the zeroth Landau level forms when the magnetic field is applied, the chiral magnetic effect should manifest itself

in equilibrium.

1.3.3 Vortex lattice

As discovered by Meissner in 1933, a magnetic field is repelled from a superconductor. This poses both practical and conceptual difficulties in the observation of the equilibrium CME: if the magnetic field cannot penetrate the superconductor, the Landau levels cannot develop and CME will not occur. A way around this is to consider a thin sample, as the magnetic field can penetrate the superconductor up to a certain distance called the penetration depth λ. For a superconducting slab much thinner than λ, the magnetic field applied parallel to its surface will penetrate it almost uniformly. Such a situation was considered by O'Brien et al. [47] who found that when a Weyl superconductor is driven into a regime with just a single Weyl cone present, the equilibrium CME occurs, with the current given by

$$\Delta j = \kappa \frac{e^2}{h} \Delta\mu \,, \tag{1.19}$$

where κ is a non-universal coefficient describing the effective charge κe of the low-energy excitations. This factor appears due to change in the degeneracy of the Landau level, in which the electron charge is replaced by the effective charge.

If a sample is thicker, and the magnetic field is strong enough, the superconductor may enter a mixed phase, in which the magnetic field penetrates the superconductor in the form of vortices of circulating supercurrent – Abrikosov vortices. In each vortex core, the size of which is approximately equal to the superconducting coherence length ξ, the superconductivity is destroyed, whereas the magnetic field decays exponentially with the distance from the vortex core, with the decay length λ. The number of vortices is equal to the number of superconducting flux quanta $h/(2e) = \frac{1}{2}\Phi_0$ of the applied magnetic field. If $\lambda > \xi/\sqrt{2}$, the mixed phase is energetically favorable to the Meissner effect, which is the defining property of a type-II superconductor. Moreover, if $\lambda \gg \sqrt{h/(eB)} \gg \xi$, the vortex cores occupy a negligible volume of the system, and the distances between them are small compared to λ, which yields an almost homogeneous magnetic field.

One can ask whether the Landau levels can develop in this mixed phase. A similar question was considered in the context of unconventional d-wave superconductors, whose superconducting pairing depends on the quasi-momentum, and vanishes on certain lines in the quasi-momentum space.

On these lines the superconducting gap closes, which gives rise to a linear dispersion relation around certain points in the quasi-momentum space, similar to that of a Weyl fermion. The robustness of the zeroth Landau level of massless relativistic fermions lead Gor'kov and Schrieffer [29] to a conclusion that the zeroth Landau level would also occur in the d-wave superconductor. The same prediction was also made by Anderson [30]. This, however, turned out not to be the case. Franz and Tešanović [1] showed that scattering of the quasiparticles from circulating vortex currents broadens the zeroth Landau level, leading to a dispersive magnetic Bloch band.

One of the questions considered in this thesis was whether the same fate awaits the zeroth Landau level in Weyl superconductors. If that was the case, it would close the way to access the equilibrium CME in the mixed phase. It turned out, however, otherwise: in the Weyl superconductors, the topological protection of the zeroth Landau level holds up against the effects of the vortices. Moreover, this leads to a CME current given by Eq. (1.14) with the universal coefficient e^2/h, independent of the effective charge κe, as it was in a thin slab.

1.4 Outline of this thesis

Chapter 2

In this chapter, we address the question whether Landau levels can emerge in a superconductor in the presence of Abrikosov vortices, induced by the applied magnetic field. We show that in a Weyl superconductor – a type of gapless superconductor, in which the low-energy excitations are Weyl fermions – it is possible. This is a surprising result, as the quasiparticle scattering off the superconducting vortices is known to spoil the Landau levels in a different type of gapless superconductors, the d-wave superconductor. We show that in the Weyl superconductor the situation is different: as a result of topological properties of the Weyl fermions, the zeroth Landau level is robust against such scattering. The particles in the zeroth Landau level can propagate along the magnetic field lines, which allows them to carry energy in that direction. This manifests itself in a contribution to the thermal conductance, which takes a universal value $G = \frac{1}{2} g_0 \Phi/\Phi_0$, where g_0 is the thermal conductance quantum, Φ_0 is the superconducting flux quantum, and Φ is the total flux of the applied magnetic field.

Chapter 3

In this chapter we further explore the consequences of the formation of the zeroth Landau level in a Weyl superconductor. We study how it affects electric and thermoelectric transport properties along the applied magnetic field. We show that the vortex lattice carries an electric current $I = \frac{1}{2}(Q_{\text{eff}}^2/h)(\Phi/\Phi_0)V$ between two normal metal contacts at voltage difference V, with Φ the magnetic flux through the system, Φ_0 the superconducting flux quantum, and $Q_{\text{eff}} < e$ the renormalized charge of the Weyl fermions in the superconducting Landau level. Because the charge renormalization is energy-dependent, a nonzero thermo-electric coefficient appears even in the absence of energy-dependent scattering processes.

Chapter 4

In this chapter we study the chiral magnetic effect in the zeroth Landau level in the Weyl superconductor: the appearance of current I along the lines of magnetic flux Φ, due to an imbalance between Weyl fermions of opposite chirality. In Weyl semimetals, the presence of such a current is only possible out of equilibrium, which makes it only accessible through indirect observations, e.g. through the negative magnetoresistance measurements. We show that in a Weyl superconductor, the chiral magnetic effect is accessible in equilibrium, manifesting itself as a universal current contribution $dI/d\Phi = (e/h)^2\mu$ (at equilibrium chemical potential μ relative to the Weyl point), when quasiparticles of one of the two chiralities are confined in vortex cores. The confined states are charge-neutral Majorana fermions.

Chapter 5

Shared contribution with Gal Lemut, who was responsible for the numerical simulations.

In this chapter we consider a different type of a superconductor: the Fu-Kane heterostructure, which consists of a superconductor on top of the surface of a topological insulator. The gapless surface excitations of a topological insulator acquire an energy gap in the presence of superconductivity. It is known that when a vortex-forming magnetic field is applied perpendicular to the surface, each vortex binds a zero-energy Majorana mode exponentially localized at its core. We examine the consequences of applying a supercurrent parallel to the surface. When the magnitude of the supercurrent exceeds a critical value, the surface quasiparticle gap closes, which drives a deconfinement transition of the Majorana bound

states. In the deconfined phase at zero chemical potential, the Majorana fermions form a dispersionless Landau level, protected by chiral symmetry against broadening due to vortex scattering. The coherent superposition of electrons and holes in the Majorana Landau level is detectable as a local density of states oscillation with a known wave vector. The striped pattern also provides a means to measure the chirality of the Majorana fermions.

Chapter 6

Shared contribution with Gal Lemut, who was responsible for the numerical simulations.

In this chapter we study a mathematical problem of discretizing the single-cone Dirac equation. Such a problem arises when performing a computer simulation of gapless excitations on the surface of a topological insulator or superconductor. The simplest approach results in so-called fermion doubling: appearance of an additional gapless low energy excitations in the simulated system. It is known that this cannot be avoided without breaking locality or chiral symmetry of the model. In this chapter we examine a special staggered discretization by Stacey [110], which avoids the fermion doubling. In this approach the Dirac equation is discretized as a generalized eigenvalue problem $\mathcal{H}\psi = E\mathcal{P}\psi$. While maintaining the chiral symmetry, this formulation breaks locality, as it can be cast in the form of an ordinary eigenvalue problem with a non-local Hamiltonian. We show that despite this shortcoming, the resulting theory possesses a locally-conserved particle current. As the discretization maintains the symmetries of the original Dirac equation, this permits the study of the spectral statistics of Dirac fermions in each of the four symmetry classes A, AII, AIII and D of random-matrix theory.

2 Topologically protected Landau level in the vortex lattice of a Weyl superconductor

2.1 Introduction

In 1998 Gor'kov, Schrieffer [29], and Anderson [30] made the remarkable prediction that the excitation spectrum in the mixed phase of a high-T_c superconductor (with massless quasiparticles at nodal points of the d-wave pair potential) has the Landau levels of the relativistic Dirac equation. This was nearly a decade before the quantum Hall effect of massless electrons was measured in graphene [31, 32], and it would have marked the first appearance in the solid state of a magnetic-field independent zeroth Landau level.

It did not turn out that way: The spatially varying supercurrent in the Abrikosov vortex lattice strongly scatters the quasiparticles [33], even if the vortices overlap and produce a uniform magnetic field. Since Franz and Tešanović [1] we know that the quasiparticles in the mixed phase of a d-wave superconductor retain the zero-field Dirac cone, the main effect of the magnetic field being a renormalization of the Fermi velocity [2–11]. Recent proposals [34–36] use strain to mimic the effect of a magnetic field in a d-wave superconductor without breaking time-reversal symmetry, but the coexistence of Landau levels and a vortex lattice has remained elusive.

Here we propose that Weyl superconductors can make it happen. A Weyl semimetal with induced s-wave superconductivity has massless nodal quasiparticles in a 3D Weyl cone [12, 13], with the same linear dispersion as the 2D Dirac cone of a d-wave superconductor [37, 38]. We compare the band structures in Fig. 2.1[1]. In zero magnetic field the gapless nodal

[1] See the appendices, which includes Refs. [39–46], for: (A) the derivation of the boundary condition at the vortex core; (B) details of the tight-binding calculation; (C) demonstration of the power law scaling of the quasiparticle density near the

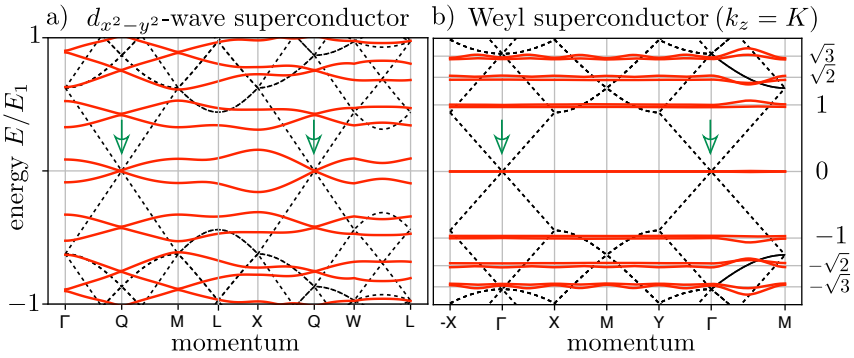

Figure 2.1: Excitation spectrum of a nodal superconductor in zero magnetic field (black dashed curves) and in the mixed phase with a square lattice of Abrikosov vortices (red solid curves)[2]. Panel a) is for a 2D d-wave superconductor, panel b) for a 3D Weyl superconductor (with $k_z = \pi/3$ at the Weyl point). The momentum follows a path through the magnetic Brillouin zone of Fig. 2.2. The location of the zero-field Dirac and Weyl points is indicated by green arrows. The n-th Landau level is expected at $E_n = \sqrt{n}\, E_1$, with $E_1 = 2\sqrt{\pi}\, v_\mathrm{F}/d_0$. In the d-wave superconductor the Landau levels are destroyed by the vortex lattice [1], while in the Weyl superconductor they are protected by chiral symmetry.

points at the Fermi level ($E = 0$) are qualitatively the same in both superconductors. But the response to a vortex lattice is fundamentally different: While in the d-wave superconductor the dispersive Dirac cones persist, as expected [1], in the Weyl superconductor a zeroth Landau level appears that is completely dispersionless in the plane perpendicular to the magnetic field.

We will return to these numerical calculations later on, but first we want to explain why the zeroth Landau level in a Weyl superconductor is not broadened by the vortex lattice, as it is in a d-wave superconductor.

vortex core. The appendices also include a demonstration of the robustness of our results to: (D) anisotropic Weyl cones and arbitrary orientation of the magnetic field; (E) tilting of the Weyl cones, all the way up to the type-I–II transition.

[2] In dimensionless units ($t_0, a_0, \hbar \equiv 1$) the parameters for the band structure of Fig. 2.1a are: $\Delta_0 = 1$ ($d_{x^2-y^2}$ pairing), $v_\mathrm{F} = v_\Delta = 2\sqrt{2}$ (isotropic Dirac cone), $\mu = 4$ (band center), $d_0 = 49$, $E_1 = 4\sqrt{2\pi}/d_0$; for Fig. 2.1b they are: $\Delta_0 = 1$ (s-wave pairing), $\beta = \sqrt{2}$, $v_\mathrm{F} = 1$ (isotropic Weyl cone), $\mu = 0$ (Weyl point), $d_0 = 49$, $E_1 = 2\sqrt{\pi}/d_0$. In the Weyl semimetal with a vortex lattice we increased μ slightly from 0 to 0.0031, to line up with the crossing point of the zeroth Landau levels of opposite chirality.

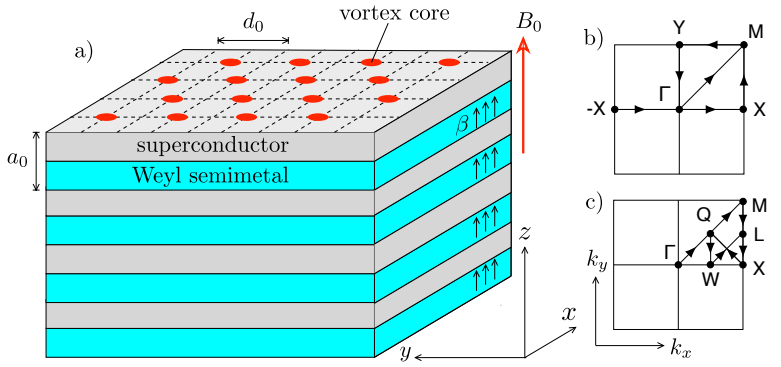

Figure 2.2: Weyl superconductor in the mixed phase. Panel a) shows a Weyl semimetal–superconductor heterostructure (layers of a topological insulator, with perpendicular magnetization β, separated by s-wave superconducting spacer layers [12]). A magnetic field B_0 is applied perpendicular to the layers. The heterostructure has lattice constant a_0, while the square vortex array has lattice constant d_0 (with two $h/2e$ vortices per unit cell). Panels b) and c) show two different paths through the magnetic Brillouin zone of the vortex array.

We have traced the origin of the difference to the topological protection of the zero-mode enforced by an index theorem for Hamiltonians with chiral symmetry [17]. For this explanation we will use an effective low-energy Hamiltonian. The numerics uses the full Hamiltonian and serves as a test of our analytics. We conclude with a discussion of the universal thermal conductance supported by the zero-mode.

2.2 Weyl superconductor in the mixed phase

We start quite generally from the Bogoliubov-De Gennes (BdG) Hamiltonian in the Anderson gauge [30],

$$\begin{aligned}\mathcal{H}(\boldsymbol{k}) &= U^\dagger \begin{pmatrix} H_0(\boldsymbol{k}-e\boldsymbol{A}) & \Delta \\ \Delta^* & -\sigma_y H_0^*(-\boldsymbol{k}-e\boldsymbol{A})\sigma_y \end{pmatrix} U \\ &= \begin{pmatrix} H_0(\boldsymbol{k}+\boldsymbol{a}+m\boldsymbol{v}_s) & \Delta_0 \\ \Delta_0 & -\sigma_y H_0^*(-\boldsymbol{k}-\boldsymbol{a}+m\boldsymbol{v}_s)\sigma_y \end{pmatrix}, \end{aligned} \tag{2.1}$$

with the definitions ($\hbar \equiv 1$, electron charge $+e$, mass m):

$$U = \begin{pmatrix} e^{i\phi} & 0 \\ 0 & 1 \end{pmatrix}, \quad \boldsymbol{a} = \tfrac{1}{2}\nabla\phi, \quad m\boldsymbol{v}_s = \tfrac{1}{2}\nabla\phi - e\boldsymbol{A}. \tag{2.2}$$

The 2×2 matrix structure of H refers to electron and hole quasiparticles, with single-particle Hamiltonian H_0 and its time-reverse in the diagonal blocks, coupled by the superconducting pair potential $\Delta = \Delta_0 e^{i\phi}$ in the off-diagonal blocks. The unitary transformation U removes the spatially dependent phase $\phi(x, y)$ from the pair potential into the single-particle Hamiltonian, where it combines with the vector potential $\boldsymbol{A}(x, y)$ in the x–y plane, corresponding to the magnetic field $\boldsymbol{B} = \nabla \times \boldsymbol{A}$ along z.

Both the gauge field $\boldsymbol{a}(x, y)$ and the supercurrent velocity $\boldsymbol{v}_s(x, y)$ wind around the positions $\boldsymbol{R}_n$ of the vortex cores, according to

$$\nabla \times \nabla\phi = 2\pi\hat{z}\textstyle\sum_n \delta(\boldsymbol{r} - \boldsymbol{R}_n). \tag{2.3}$$

(For definiteness we assume the field points in the *positive* z-direction.) A spatial average over the vortices gives a vanishing supercurrent velocity, $\overline{\boldsymbol{v}}_s = 0$, while the average $\overline{\nabla \times \boldsymbol{a}} = e\bar{\boldsymbol{B}}$ gives the average magnetic field. The field is approximately uniform, equal to B_0, in the mixed phase $H_{c1} \ll B_0 \ll H_{c2}$ of a type-II superconductor with overlapping vortices. In this regime the vortex cores occupy only a small fraction $B_0/H_{c2} \ll 1$ of the volume, so the amplitude Δ_0 of the pair potential is also approximately uniform and only the phase ϕ is strongly position dependent.

We now specify to a Weyl superconductor, in the heterostructure configuration of Meng and Balents [12][3]: a stack in the z-direction of layers of Weyl semimetal alternating with an s-wave superconductor. A magnetization β perpendicular to the layers separates the Weyl cones in the Brillouin zone along k_z. The Weyl points are at $\boldsymbol{k} = (0, 0, \pm K)$, $v_{\mathrm{F}}^2 K^2 = \beta^2 - \Delta_0^2$, with v_{F} the Fermi velocity (assumed isotropic for simplicity). The Weyl cones remain gapless as long as $\Delta_0 < \beta$[4].

In the BdG Hamiltonian (2.1) each Weyl cone is doubled into an electron and hole cone, mixed by the pair potential. We describe this mixing following Ref. 47, in the simplest case that the Weyl cones are close to the center $\boldsymbol{k} = 0$ of the Brillouin zone and we may linearize the momenta. (All nonlinearities in the full Brillouin zone are included in our numerics.) The single-particle Weyl Hamiltonian H_0 is a 4×4 matrix,

$$H_0(\boldsymbol{k}) = v_{\mathrm{F}}\tau_z \boldsymbol{k} \cdot \boldsymbol{\sigma} + \beta\tau_0\sigma_z - \mu\tau_0\sigma_0, \tag{2.4}$$

[3] We use the heterostructure model of Ref. 12 for concreteness, but we have checked that the Landau levels appear as well in the model of Ref. 13, which refers to a Weyl semimetal with intrinsic superconductivity. The difference between the two models, scalar versus pseudoscalar pairing [28], does not affect the topological protection.

[4] A supercurrent perpendicular to the layers can gap out the Weyl cones even if $\Delta_0 < \beta$, but for now we only consider supercurrents flowing in the plane of the layers. In the presence of time-reversal symmetry, for $\beta = 0$, the Weyl superconductor is gapped except at the vortex cores, so no Landau level can exist in the bulk.

with μ the chemical potential. It is composed from Pauli matrices σ_α and τ_α that act on the spin and orbital degree of freedom, respectively. We also need a third set of Pauli matrices ν_α in the electron-hole basis. (The corresponding 2×2 unit matrices are σ_0, τ_0, ν_0.)

A unitary transformation $\mathcal{H} \mapsto V^\dagger \mathcal{H} V$ with

$$V = \exp(\tfrac{1}{2} i\theta \nu_y \tau_z \sigma_z), \quad \tan\theta = -\frac{\Delta_0}{v_\mathrm{F} k_z}, \quad \theta \in (0, \pi), \tag{2.5}$$

followed by a projection onto the $\nu = \tau = \pm 1$ blocks, gives for the Weyl cones an effective 2×2 low-energy Hamiltonian[5]:

$$\begin{aligned} H_\pm(\boldsymbol{k}) &= v_\mathrm{F} \textstyle\sum_{\alpha=x,y} (k_\alpha + a_\alpha \pm \kappa m v_{s,\alpha}) \sigma_\alpha \\ &\quad + (\beta - m_{k_z}) \sigma_z \mp \kappa \mu \sigma_0, \end{aligned} \tag{2.6}$$

$$m_{k_z} = \sqrt{\Delta_0^2 + v_\mathrm{F}^2 k_z^2}, \quad \kappa = -v_\mathrm{F} k_z / m_{k_z}. \tag{2.7}$$

The electron-like and hole-like cones have opposite sign of the effective charge $q_\mathrm{eff} = \pm\kappa e$, with $|q_\mathrm{eff}| \to e\sqrt{1 - \Delta_0^2/\beta^2}$ for $|k_z| \to K$, smaller than the bare charge e due to the mixing of electrons and holes by the pair potential [48]. The velocity $v_z = \partial m_{k_z}/\partial k_z$ perpendicular to the layers is also renormalized by the superconductivity: $v_z \to v_\mathrm{F}^2 K/\beta$ for $|k_z| \to K$.

At the Weyl point, for $\mu = 0$ and $|k_z| = K$, the Hamiltonian (2.6) anticommutes with σ_z. This socalled chiral symmetry gives a formal correspondence with a problem first studied 40 years ago by Aharonov and Casher [16], as an application of an index theorem from supersymmetric quantum mechanics [17]. The problem of Ref. 16, to determine the zeroth Landau level of a two-dimensional massless electron in an inhomogeneous magnetic field, has also been studied more recently in the context of graphene [49–51]. We need to adapt the calculation here to account for the fractionally charged quasiparticles, but the basic approach carries through.

[5]The low-energy Hamiltonian (2.6) does not include virtual transitions to higher bands, of second order in μ and v_s. These are included in the numerics, which is based on the full Hamiltonian.

2.3 Calculation of the zero-modes

To study the effect of chiral symmetry on the Landau level spectrum we set $\mu = 0$, $|k_z| = K$ and focus our attention on the chiral Hamiltonian

$$\begin{aligned} &H_{\text{chiral}} = v_{\text{F}} \begin{pmatrix} 0 & \mathcal{D} \\ \mathcal{D}^\dagger & 0 \end{pmatrix}, \;\; \mathcal{D} = \Pi_x - i\Pi_y, \\ &\boldsymbol{\Pi} = -i\nabla + e\mathcal{A}, \;\; e\mathcal{A} = \boldsymbol{a} \pm \kappa m \boldsymbol{v}_s. \end{aligned} \tag{2.8}$$

(We omit the $\pm$ subscript for ease of notation.) The effective vector potential $\mathcal{A}$ describes the effective magnetic field

$$\mathcal{B} = \partial_x \mathcal{A}_y - \partial_y \mathcal{A}_x = \Phi_0(1 \pm \kappa) \textstyle\sum_n \delta(\boldsymbol{r} - \boldsymbol{R}_n) \mp \kappa B \tag{2.9}$$

felt by the Weyl fermions in the vortex lattice.

For what follows it is convenient to choose a gauge such that $\nabla \cdot \mathcal{A} = 0$ and to assume that the external magnetic field B_0 is imposed on a large but finite area S. Because there are $N_{\text{vortex}} = B_0 S/\Phi_0$ vortices in that area (with $\Phi_0 = h/2e$ the superconducting flux quantum), the flux $\Phi = \int d\boldsymbol{r}\, \mathcal{B} = B_0 S$ through the system corresponding to the effective field equals the real flux. (The κ-dependence of $\mathcal{B}$ drops out upon spatial integration.)

A zero-mode ψ of H_{chiral} is either a spinor $\binom{u}{0}$ with $\mathcal{D}^\dagger u = 0$ or it is a spinor $\binom{0}{v}$ with $\mathcal{D}v = 0$. The general solution of these two differential equations has the form [16, 50][6]:

$$\begin{aligned} &u = f(\zeta) e^{W}, \;\; v = f(\zeta^*) e^{-W}, \;\; \zeta = x + iy, \\ &W(\boldsymbol{r}) = \frac{1}{2\Phi_0} \int dx' \int dy'\, \mathcal{B}(\boldsymbol{r}') \ln|\boldsymbol{r} - \boldsymbol{r}'|. \end{aligned} \tag{2.10}$$

The difference $\mathcal{N} = N_u - N_v$ in the number of normalizable solutions for u and v is called the index of H_{chiral}. The absolute value $|\mathcal{N}|$ is a lower bound on the degeneracy of the zero-mode and the sign of $\mathcal{N}$ determines the chirality: whether the zero-mode is an eigenstate of σ_z with eigenvalue $+1$ or -1.

To determine the index of H_{chiral} we proceed as follows. In the absence of vortices the function $f(\zeta)$ is analytic in the entire complex plane and

[6] To verify Eq. (2.10), first note that $(-i\partial_x \pm \partial_y) f(x \pm iy) = 0$, so we only need to consider derivatives of W. For that purpose it is helpful to write $\mathcal{A} = \nabla \times \hat{z}\omega$ (which is possible in the gauge where $\nabla \cdot \mathcal{A} = 0$), then note that $\mathcal{B} = -\nabla^2 \omega$ and use the identity $\nabla^2 \ln|\boldsymbol{r} - \boldsymbol{r}'| = 2\pi\delta(\boldsymbol{r} - \boldsymbol{r}')$, to derive that $W = -(\pi/\Phi_0)\omega = -e\omega$ and $(-i\partial_x \pm \partial_y)W = \mp e\mathcal{A}_x - ie\mathcal{A}_y$. Hence one concludes that $(\Pi_x \pm i\Pi_y)e^{\pm W} = 0$.

we can use a basis of polynomials. A polynomial $f(\zeta)$ of degree $N-1$ then produces N linearly independent zero-modes — provided u or v is normalizable, $\int r dr\, |\psi|^2 < \infty$. For large r one has asymptotically

$$W \to \tfrac{1}{2}(\Phi/\Phi_0) \ln |\boldsymbol{r}| \Rightarrow e^W \to |\boldsymbol{r}|^{N_{\rm vortex}/2}, \tag{2.11}$$

so if only the decay at infinity would be an issue we would conclude that $N_u = 0$, $N_v = \mathrm{Int}\,[N_{\rm vortex}/2]$. This is the answer in the absence of vortices [16], when the degeneracy of the zero-mode is determined by the enclosed flux in units of $h/e = 2\Phi_0$, while the chirality is set by the sign of the magnetic field (which we have assumed positive). As we will now show, the presence of vortices introduces a dependence of the chirality on the sign of the fractional charge $q_{\rm eff} = \pm\kappa e$ of the quasiparticles, while the degeneracy remains given by the bare electron charge e.

With vortices the function $f(\zeta)$ may have poles at the vortex cores $\zeta_n = x_n + iy_n$. We use this freedom to re-express the solution (2.10) as

$$u = g(\zeta) e^W \textstyle\prod_n (\zeta - \zeta_n)^{-1}, \;\; v = f(\zeta^*) e^{-W}. \tag{2.12}$$

If for f and g we take polynomials of degree $N-1$, with $N = \mathrm{Int}\,[N_{\rm vortex}/2]$, then both the functions u and v decay sufficiently rapidly at infinity. The boundary condition at the vortex cores now determines which of the two solutions is realized.

Near a vortex at position $\boldsymbol{r}_n$ the asymptotics is

$$|u|^2 \to |\boldsymbol{r} - \boldsymbol{r}_n|^{-1+q_{\rm eff}/e}, \;\; |v|^2 \to |\boldsymbol{r} - \boldsymbol{r}_n|^{-1-q_{\rm eff}/e}. \tag{2.13}$$

Since $|q_{\rm eff}| < e$ both solutions $\psi_u = \binom{u}{0}$ and $\psi_v = \binom{0}{v}$ remain square integrable at the vortex core. The boundary condition[1]

$$\sigma_z \psi = (\mathrm{sign}\, q_{\rm eff})\, \psi, \;\; \text{for } \boldsymbol{r} \to \boldsymbol{r}_n. \tag{2.14}$$

selects the most weakly divergent solution in Eq. (2.13): $\psi = \psi_u$ with positive chirality for $q_{\rm eff} > 0$ and $\psi = \psi_v$ with negative chirality for $q_{\rm eff} < 0$.

All of this was for $\mu = 0$, $|k_z| = K$, but both terms $\mu\sigma_0$ and $(\beta - m_{k_z})\sigma_z$ from Eq. (2.6) can be immediately reinstated since the zero-mode is an eigenstate of σ_z. The resulting μ and k_z-dependence of the zeroth Landau level is

$$E_\pm(k_z) = \mp\kappa\mu + (\mathrm{sign}\, q_{\rm eff})(\beta - m_{k_z}). \tag{2.15}$$

We have thus seen how the chiral symmetry protects the zeroth Landau level from being destroyed by the vortex lattice. To complete this

analytical treatment, we point out why the d-wave superconductor lacks a similar protection. In the Anderson gauge, the low-energy Hamiltonian near the nodal point of a d-wave pair potential reads [1, 6, 30]

$$H_{d\text{-wave}} = v_{\mathrm{F}}(k_x + a_x)\sigma_z + v_\Delta(k_y + a_y)\sigma_x + mv_{s,x}\sigma_0. \tag{2.16}$$

There are inessential differences with H_{chiral} from Eq. (2.8) — the Dirac cone is anisotropic and the basis of Pauli matrices is rotated — but the essential difference is that the superfluid velocity breaks the chiral symmetry: $H_{d\text{-wave}}$ anticommutes with σ_y only if $v_{s,x} = 0$. In the d-wave superconductor the superfluid velocity enters as a chirality-breaking scalar potential, while in the Weyl superconductor it is a chirality-preserving vector potential. The former is a strong scatterer, which effectively destroys the Landau levels, while the latter cannot by force of the topological index theorem.

2.4 Comparison with numerics

To test our analytical theory we have numerically calculated the spectrum of a Weyl superconductor with a vortex lattice, using the *Kwant* tight-binding code [52]. The 8×8 Hamiltonian has the BdG form (2.1) with [12, 13, 28]

$$\begin{aligned} H_0(\boldsymbol{k}) = t_0 \sum_{\alpha=x,y,z} &[\tau_z\sigma_\alpha \sin k_\alpha a_0 + \tau_x\sigma_0(1 - \cos k_\alpha a_0)] \\ &+ \beta\tau_0\sigma_z - \mu\tau_0\sigma_0. \end{aligned} \tag{2.17}$$

Near the center of the Brillouin zone this reduces to the linearized Hamiltonian (2.4), but now we will not make any linearization. Results are shown in Figs. 2.1b, 2.3, and 2.4[1]. They are fully consistent with the analytics.

2.5 Thermal conductance

The chiral zeroth Landau level governs the thermal transport properties of the Weyl superconductor, in the direction parallel to the magnetic field. The degeneracy $eB_0S/h = \frac{1}{2}\Phi/\Phi_0$ of the zeroth Landau level implies a thermal conductance

$$G_{=\frac{1}{2}g_0\Phi/\Phi_0}, \quad g_0 = \mathcal{L}Te^2/h, \tag{2.18}$$

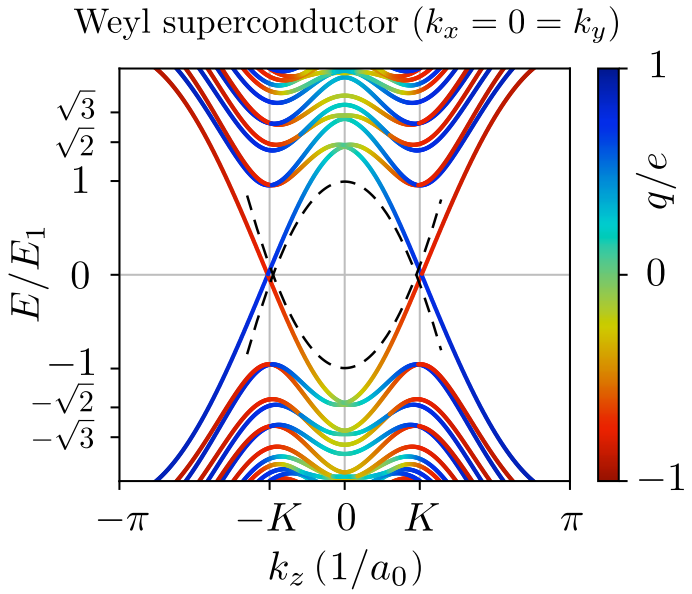

Figure 2.3: Same as Fig. 2.1b, but now as a function of k_z for $k_x = 0 = k_y$ at the center of the Brillouin zone[7]. The color scale indicates the charge expectation value. The dashed curve is the dispersion (2.15) of the zeroth Landau level, calculated analytically for $K \ll 1$ (which explains the deviation from the numerics). The effective charge at $E = 0$ is ± 0.73, close to the analytical prediction of $\pm\kappa = \pm 1/\sqrt{2}$.

with $\mathcal{L} = \frac{1}{3}(\pi k_B/e)^2$ the Lorenz number. In words, each vortex contributes half a thermal conductance quantum to the heat transport — the factor 1/2 being a reminder that the quasiparticles in the Weyl superconductor are Majorana fermions [48]. Do note that the states in the zeroth Landau level are extended over the x–y plane, the current flow is not confined to the vortex cores (see Fig. 2.4)[8]. We expect the universal thermal conductance (2.18) to be robust against non-magnetic disorder, which in the effective Hamiltonian would enter as a term $\propto \sigma_z$ that does not couple Landau levels of opposite chirality.

[7] The parameters for the band structure of Fig. 2.3 are the same as those of Fig. 2.1b, except that we took a larger magnetic field ($d_0 = 10$) so that the Landau level splitting is more clearly visible on this scale.

[8] As we will discuss in Chapter 4, it is possible to concentrate the heat flow to the vortex cores by applying a flux bias, and in that way realize a situation reminiscent of the axion insulator of Ref. 84.

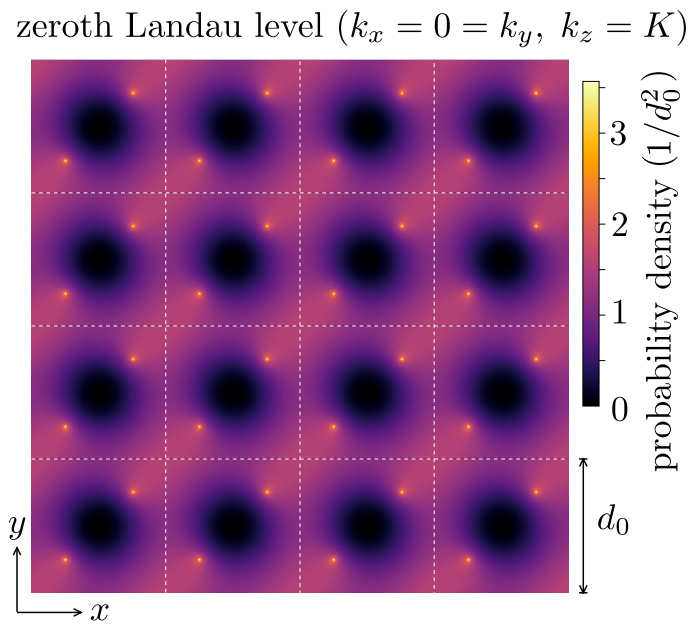

Figure 2.4: Color scale plot of $|\psi(x, y)|^2$ in the zeroth Landau level of the Weyl superconductor[9]. The white dashed lines indicate the vortex array, with a pair of $h/2e$ vortices in each unit cell. On approaching a vortex core, when the separation $\delta r \to 0$, the density diverges as a power law $|\psi|^2 \propto \delta r^{1/\sqrt{2}-1}$, in accord with Eq. (2.13).

2.6 Conclusion

In this work we have revisited the celebrated question [29, 30] whether quasiparticles in the vortex lattice of a gapless superconductor can condense into Landau levels. We have shown that Weyl superconductors can accomplish what d-wave superconductors could not [1]: The chirality of Weyl fermions protects the zeroth Landau level from broadening due to scattering by the vortices. We have developed the analytical argument for a simple low-energy Hamiltonian and supported it by numerical calculations for a heterostructure model of the Weyl superconductor [12]. We anticipate that the Landau levels will govern the thermodynamic and

[9] The wave function in Fig. 2.4 is evaluated for the same parameters as Fig. 2.1b, but at a smaller magnetic field ($d_0 = 202$), to have a smaller overlap of the vortices. There are two zero-modes of opposite effective charge $q_{\text{eff}} = \pm\kappa e$, with identical density profile so we only show one of them.

transport properties of the vortex lattice, finally allowing for the observation of quantum effects that proved elusive in the d-wave context.

Appendices

2.A Boundary condition at the vortex core

We consider the chiral Hamiltonian (2.8) near a vortex at the origin,

$$H_{\text{vortex}} = v_{\text{F}} \sum_{\alpha=x,y} (p_\alpha + e\mathcal{A}_\alpha)\sigma_\alpha + M(\boldsymbol{r})\sigma_z, \tag{2.19}$$

retaining only the singular contribution to the vector potential,

$$\nabla \times e\mathcal{A} = (e + q_{\text{eff}})\Phi_0 \hat{z}\delta(\boldsymbol{r}) \Rightarrow e\mathcal{A} = \frac{(e + q_{\text{eff}})\Phi_0}{2\pi r}\hat{\theta}. \tag{2.20}$$

A similar eigenvalue problem has been studied in the context of graphene [39], but without the fractional charge $q_{\text{eff}} = \pm\kappa e$ characteristic of the Weyl superconductor.

We model the delta-function vortex singularity by a mass term $M(\boldsymbol{r}) = M_0\theta(d_{\text{vortex}} - r)$, in the limit $M_0 \to \infty$, $d_{\text{vortex}} \to 0$ with $M_0 d_{\text{vortex}}^2$ finite. In that limit the effective charge tends to the bare charge, $q_{\text{eff}} \to \pm e$, within the vortex core.

In polar coordinates (r, θ) one has

$$\frac{\partial}{\partial x} + i\frac{\partial}{\partial y} = e^{i\theta}\left(\frac{\partial}{\partial r} + \frac{i}{r}\frac{\partial}{\partial \theta}\right), \tag{2.21a}$$

$$e\mathcal{A}_x + ie\mathcal{A}_y = \frac{\lambda}{r} ie^{i\theta}, \quad \lambda = \tfrac{1}{2} + q_{\text{eff}}/2e \in (0, 1). \tag{2.21b}$$

(Recall that $e\Phi_0/2\pi = \hbar/2 \equiv 1/2$.) The Dirac Hamiltonian then takes the form

$$H_{\text{vortex}} = \begin{pmatrix} M & D_- \\ D_+ & -M \end{pmatrix}, \tag{2.22a}$$

$$D_\pm = v_{\text{F}} e^{\pm i\theta}\left(-i\frac{\partial}{\partial r} \pm \frac{1}{r}\frac{\partial}{\partial \theta} \pm \frac{i\lambda}{r}\right). \tag{2.22b}$$

Since H_{vortex} commutes with the angular momentum operator $J = -i\partial_\theta + \frac{1}{2}\sigma_z$, with eigenvalues $m - 1/2$ for integer m, the eigenstates of

$H_{\rm vortex}$ can be chosen as eigenstates of J,

$$\psi_m(r,\theta) = e^{im\theta}\begin{pmatrix} e^{-i\theta}u_m(r) \\ iv_m(r)\end{pmatrix}, \tag{2.23a}$$

$$(M-E)u_m + v_{\rm F}[\partial_r + (m+\lambda)r^{-1}]v_m = 0, \tag{2.23b}$$

$$(M+E)v_m + v_{\rm F}[\partial_r - (m-1+\lambda)r^{-1}]u_m = 0. \tag{2.23c}$$

We take $E=0$ and consider the solutions outside the vortex core ($r > d_{\rm vortex}$, where $M=0$) and inside the vortex core ($r < d_{\rm vortex}$, $M = M_0 > 0$). Outside the vortex core the solutions for u_m and v_m decouple,

$$u_m = C_1 r^{m-1+\lambda}, \;\; v_m = C_2 r^{-m-\lambda}, \tag{2.24}$$

with independent coefficients C_1, C_2. Inside the vortex core we have, in view of the Bessel function identities

$$\partial_r I_\alpha(r) \pm (\alpha/r) I_\alpha(r) = I_{\alpha\mp1}(r), \tag{2.25a}$$

$$\partial_r K_\alpha(r) \pm (\alpha/r) K_\alpha(r) = -K_{\alpha\mp1}(r), \tag{2.25b}$$

the general solution

$$\begin{aligned} u_m(r) &= C_3\, I_{m-1+\lambda}(M_0\, r/v_{\rm F}) + C_4 K_{m-1+\lambda}(M_0\, r/v_{\rm F}), \\ v_m(r) &= -C_3\, I_{m+\lambda}(M_0\, r/v_{\rm F}) + C_4 K_{m+\lambda}(M_0\, r/v_{\rm F}). \end{aligned} \tag{2.26}$$

We may set $C_4 = 0$ to obtain a regular solution at $r=0$ for $q_{\rm eff} = \pm e \Rightarrow \lambda \in \{0,1\}$.

The global solution (2.12) has outside the vortex at $\boldsymbol{r}_n \equiv 0$ the asymptotics

$$\psi_{\rm outside} = \begin{pmatrix} C_1 e^{-i\theta} r^{-1/2+q_{\rm eff}/2e} \\ C_2 i r^{-1/2-q_{\rm eff}/2e}\end{pmatrix}, \tag{2.27}$$

since $\zeta - \zeta_n = e^{i\theta} r$. This corresponds to the local solution $\psi_m(r,\theta)$ outside the vortex core for quantum number $m=0$. We need to match this to the $m=0$ solution inside the vortex core. In the large-M_0 limit, for $M_0 \gg v_{\rm F}/r$, this has the asymptotics

$$\psi_{\rm inside} = \frac{C_3\, e^{M_0 r/v_{\rm F}}}{\sqrt{2\pi M_0 r/v_{\rm F}}}\begin{pmatrix} e^{-i\theta} \\ -i\end{pmatrix}, \tag{2.28}$$

since the Bessel-K function becomes exponentially small $\propto \exp(-M_0 r/v_{\rm F})$.

Equating $\psi_{\rm outside}$ and $\psi_{\rm inside}$ at $r = d_{\rm vortex}$ gives the ratio of coefficients

$$C_2/C_1 = -(d_{\rm vortex})^{q_{\rm eff}/e}. \tag{2.29}$$

If we finally send $d_{\rm vortex} \to 0$, we find that $C_2 \to 0$ for $q_{\rm eff} > 0$, while $C_1 \to 0$ for $q_{\rm eff} < 0$. This corresponds to the boundary condition (2.14) in the main text.

2.B Details of the tight-binding calculations

2.B.1 Weyl superconductor

We discretize the BdG Hamiltonian (2.1) in the Anderson gauge on a square lattice, lattice constant $a_0 \equiv 1$, nearest-neigbor hopping energy $t_0 \equiv 1$. For the diagonal block $H_0(\boldsymbol{k})$ we take the four-band model of Eq. (2.17). The tight-binding Hamiltonian is

$$\begin{aligned}\mathcal{H} = &\sum_{\boldsymbol{n}} \begin{pmatrix} h(k_z) & \Delta_0 \\ \Delta_0 & -\sigma_y h(-k_z)^* \sigma_y \end{pmatrix} |\boldsymbol{n}\rangle\langle\boldsymbol{n}| \\ &+ \frac{1}{2}\sum_{\boldsymbol{n},\hat{\boldsymbol{\delta}}} \begin{pmatrix} \exp\Big(i\int_{\boldsymbol{n}}^{\boldsymbol{n}+\hat{\boldsymbol{\delta}}} e\boldsymbol{A}\cdot d\boldsymbol{l} - i\phi_{\boldsymbol{n}+\hat{\boldsymbol{\delta}}} + i\phi_{\boldsymbol{n}}\Big) & 0 \\ 0 & -\exp\Big(-i\int_{\boldsymbol{n}}^{\boldsymbol{n}+\hat{\boldsymbol{\delta}}} e\boldsymbol{A}\cdot d\boldsymbol{l}\Big) \end{pmatrix} \\ &\times (i\tau_z \boldsymbol{\sigma}\cdot\hat{\boldsymbol{\delta}} - \tau_x\sigma_0)|\boldsymbol{n}+\hat{\boldsymbol{\delta}}\rangle\langle\boldsymbol{n}|, \\ h(k_z) = &\tau_z\sigma_z \sin k_z + \tau_x\sigma_0(3-\cos k_z) + \beta\tau_0\sigma_z - \mu\tau_0\sigma_0. \end{aligned} \tag{2.30}$$

The vector $\boldsymbol{n}$ labels the lattice sites and the unit vector $\hat{\boldsymbol{\delta}}$ points to the four nearest neighbors. We denote by $\phi_{\boldsymbol{n}}$ the superconducting phase $\phi(\boldsymbol{r})$ at site $\boldsymbol{n}$.

We assume a uniform magnetic field $\boldsymbol{B} = B_0\hat{z}$ (appropriate for the strong-type-II regime $H_{c1} \ll B_0 \ll H_{c2}$), with vector potential

$$\boldsymbol{A}(x,y) = -\frac{2\pi}{eN^2}(y,0,0) \tag{2.31}$$

corresponding to a flux h/e through a supercell of $N\times N$ unit cells (square magnetic unit cell, lattice constant $d_0 = Na_0$). The conjugate vector potential

$$\bar{\boldsymbol{A}}(x,y) = -\frac{2\pi}{eN^2}(0,x,0) \tag{2.32}$$

is defined such that $\boldsymbol{\Pi} = \boldsymbol{p} - e\boldsymbol{A}$ and $\bar{\boldsymbol{\Pi}} = \boldsymbol{p} - e\bar{\boldsymbol{A}}$ commute, $[\Pi_\alpha, \Pi_\beta] = 0$. It enters in the magnetic periodic boundary conditions [40–42]

$$\begin{aligned} \psi(N,y) &= e^{iN[k_x - e\bar{A}_x(0,y)]}\psi(0,y) = e^{ik_xN}\psi(0,y), \\ \psi(x,N) &= e^{iN[k_y - e\bar{A}_y(x,0)]}\psi(x,0) = e^{ik_yN + 2\pi i x/N}\psi(x,0), \end{aligned} \tag{2.33}$$

for $x, y \in \{0, 1, \ldots, N-1\}$.

In each supercell we place a pair of $h/2e$ vortices, at positions

$$\begin{aligned} x^{(1)}_{\text{vortex}} &= y^{(1)}_{\text{vortex}} = \text{Int}\,[N/4] + 1/2, \\ x^{(2)}_{\text{vortex}} &= y^{(2)}_{\text{vortex}} = N - 1/2 - \text{Int}\,[N/4], \end{aligned} \tag{2.34}$$

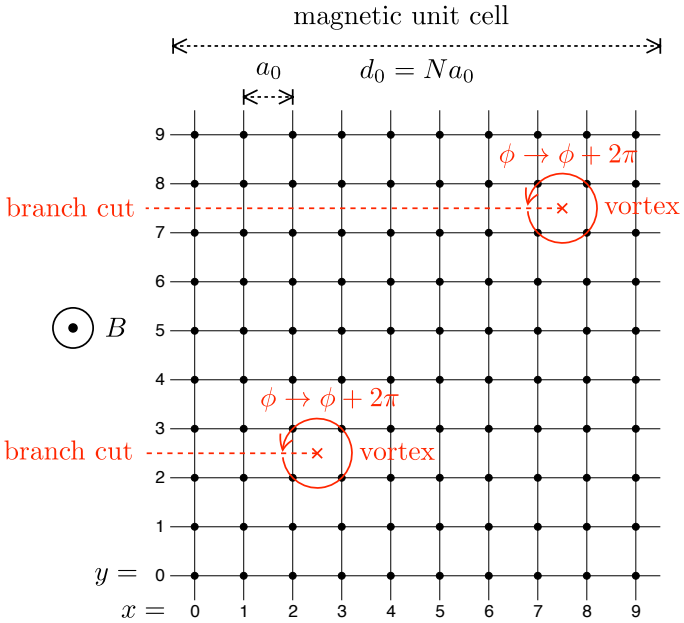

Figure 2.5: Magnetic unit cell for $N = 10$, containing a pair of $h/2e$ vortices at the positions specified by Eq. (2.34). The superconducting phase winds by 2π upon encircling a vortex, producing a branch cut. At the two sides $(x, y \pm \epsilon)$ of a branch cut one has $\phi(x, y + \epsilon) = \phi(x, y - \epsilon) + 2\pi$.

see Fig. 2.5. This produces a square vortex array consisting of two sublattices with lattice constant d_0.

2.B.2 Superconducting phase

In the continuum description the phase $\phi(\boldsymbol{r})$ of the superconducting order parameter is determined by

$$\nabla \times \nabla\phi = \sum_n 2\pi\, \delta(\boldsymbol{r} - \boldsymbol{r}_n), \quad \nabla \cdot \nabla\phi = 0. \tag{2.35}$$

The first equation specifies a 2π winding of the phase around each vortex, at position $\boldsymbol{r}_n$, and the second equation ensures that the supercurrent velocity $m\boldsymbol{v}_s = \frac{1}{2}\nabla\phi - e\boldsymbol{A}$ has vanishing divergence. (Note that $\nabla \cdot \boldsymbol{A} = 0$ for our choice of gauge.)

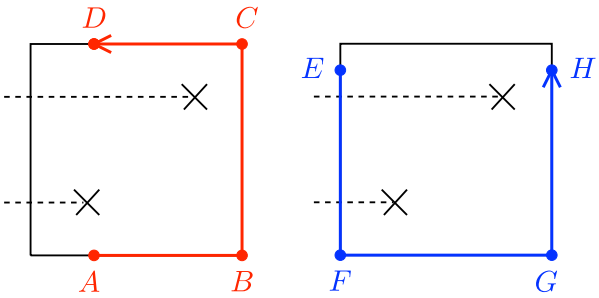

Figure 2.6: Two integration paths C along the boundary of the magnetic unit cell for which $\int_C \boldsymbol{v}_s \cdot d\boldsymbol{l} = 0$, as a consequence of Eq. (2.38). Vortices are indicated by crosses, the branch cuts in the phase by dashed lines. For the red path the integral along segment BC vanishes, while the contributions from the segments AB and CD cancel. For the blue path the segment FG does not contribute and EF cancels with GH.

We discretize Eq. (2.35) in the $N \times N$ magnetic unit cell of Fig. 2.5. To each of the two vortices in this supercell we assign a branch cut running from $(x_{\text{vortex}}, y_{\text{vortex}})$ to $(0, y_{\text{vortex}})$, at which the phase jumps by 2π. The discrete version of Eq. (2.35) then reads

$$\begin{aligned} &\phi(x, y-1) + \phi(x+1, y) + \phi(x-1, y) + \phi(x, y+1) \\ &-4\phi(x, y) = \begin{cases} \pm 2\pi & \text{if } (x, y) \to (x, y \pm 1) \\ & \text{crosses a branch cut,} \\ 0 & \text{otherwise,} \end{cases} \end{aligned} \tag{2.36}$$

for $x, y \in \{0, 1, 2, \ldots N-1\}$.

We need to supplement Eq. (2.36) by periodic boundary conditions at the edges of the magnetic unit cell. To determine these we integrate

$$\phi(\boldsymbol{r}) - \phi(\boldsymbol{r}') = 2 \int_{\boldsymbol{r}'}^{\boldsymbol{r}} (m\boldsymbol{v}_s + e\boldsymbol{A}) \cdot d\boldsymbol{l} + 2\pi n \tag{2.37}$$

along a path C from $\boldsymbol{r}'$ to $\boldsymbol{r}$. The discontinuity of ϕ when C crosses a branch cut is accounted for by the $2\pi n$ offset: The integer n equals the number of branch cut lines crossed from below minus those crossed from above.

The trick is to choose a path such that the integral of the supercurrent velocity vanishes. The combination of periodicity and inversion symmetry

implies that

$$\begin{aligned} \boldsymbol{v}_s(x,y) &= \boldsymbol{v}_s(x+N,y) = \boldsymbol{v}_s(x,y+N), \\ \boldsymbol{v}_s(x,y) &= -\boldsymbol{v}_s(-x,-y) \\ &\Rightarrow \boldsymbol{v}_s(N,y) = -\boldsymbol{v}_s(N,N-y), \\ &\quad \boldsymbol{v}_s(x,0) = -\boldsymbol{v}_s(N-x,0). \end{aligned} \tag{2.38}$$

As a consequence, the integral $\int_C \boldsymbol{v}_s \cdot d\boldsymbol{l} = 0$ vanishes for the two paths of Fig. 2.6. Integration of the vector potential gives the boundary conditions.

$$\phi(x, y_0 + N) = \phi(x, y_0) + 4\pi(1 - x/N)\,, \tag{2.39a}$$

$$\phi(x_0 + N, y) = \phi(x_0, y) - 2\pi \times (\text{number of branch cuts below } y)\,, \tag{2.39b}$$

where $x_0, y_0 \in \{0, -1\}$.

The set of equations (2.36) and (2.39) can be written in a matrix form, $\sum_j M_{ij}\phi_j = b_i$ for a real symmetric matrix M, which we solved using the conjugate gradient method.

2.B.3 *d*-wave superconductor

A 2D superconductor with spin-singlet $d_{x^2-y^2}$ pairing symmetry has BdG Hamiltonian

$$\begin{aligned} \mathcal{H} &= \begin{pmatrix} \frac{1}{2m}(\boldsymbol{k} - e\boldsymbol{A})^2 - \mu & (\boldsymbol{k} - e\boldsymbol{A}) \cdot \boldsymbol{\Delta} \cdot (\boldsymbol{k} + e\boldsymbol{A}) \\ (\boldsymbol{k} + e\boldsymbol{A}) \cdot \boldsymbol{\Delta}^\dagger \cdot (\boldsymbol{k} - e\boldsymbol{A}) & -\frac{1}{2m}(\boldsymbol{k} + e\boldsymbol{A}) - \mu \end{pmatrix}, \\ \boldsymbol{k} &= (k_x, k_y) = -i\hbar(\partial_x, \partial_y), \quad \boldsymbol{\Delta}(\boldsymbol{r}) = \Delta_0 e^{i\phi(\boldsymbol{r})} \begin{pmatrix} 1 & 0 \\ 0 & -1 \end{pmatrix}. \end{aligned} \tag{2.40}$$

Our choice of symmetrization of the pair potential follows Ref. 43. One checks that the choice (2.40) satisfies the requirement of gauge invariance,

$$\begin{pmatrix} e^{-i\chi} & 0 \\ 0 & e^{i\chi} \end{pmatrix} \mathcal{H}(e\boldsymbol{A}, \boldsymbol{\Delta}) \begin{pmatrix} e^{i\chi} & 0 \\ 0 & e^{-i\chi} \end{pmatrix} = \mathcal{H}(e\boldsymbol{A} - \nabla\chi, e^{-2i\chi}\boldsymbol{\Delta}). \tag{2.41}$$

Following Ref. 43 we discretize $\mathcal{H}$ on a square lattice (lattice constant $a_0 \equiv 1$, nearest neighbor hopping energy $t_0 = \hbar^2/2ma_0^2$). At the end we carry out the Anderson gauge transformation,

$$\mathcal{H} \mapsto \begin{pmatrix} e^{-i\phi} & 0 \\ 0 & 1 \end{pmatrix} \mathcal{H} \begin{pmatrix} e^{i\phi} & 0 \\ 0 & 1 \end{pmatrix}. \tag{2.42}$$

The resulting tight-binding Hamiltonian

$$\mathcal{H} = \sum_{\boldsymbol{m},\boldsymbol{n}} \begin{pmatrix} t_{ee}(\boldsymbol{m},\boldsymbol{n}) & t_{eh}(\boldsymbol{m},\boldsymbol{n}) \\ t_{he}(\boldsymbol{m},\boldsymbol{n}) & t_{hh}(\boldsymbol{m},\boldsymbol{n}) \end{pmatrix} |\boldsymbol{m}\rangle\langle\boldsymbol{n}| \tag{2.43}$$

has nonzero matrix elements for $\boldsymbol{m} = \boldsymbol{n}$ and $\boldsymbol{m} = \boldsymbol{n} + \hat{\boldsymbol{\delta}}$, with $\hat{\boldsymbol{\delta}} \in \{\pm\hat{\boldsymbol{x}}, \pm\hat{\boldsymbol{y}}\}$, given by

$$t_{ee}(\boldsymbol{n},\boldsymbol{n}) = -t_{hh}(\boldsymbol{n},\boldsymbol{n}) = 4t_0 - \mu, \tag{2.44a}$$

$$\begin{aligned} t_{eh}(\boldsymbol{n},\boldsymbol{n}) &= t_{he}^*(\boldsymbol{n},\boldsymbol{n}) \\ &= \tfrac{1}{2}\Delta_0 \Bigg[\exp\left(-2i \int_{\boldsymbol{n}}^{\boldsymbol{n}+\hat{\boldsymbol{x}}} e\boldsymbol{A}\cdot d\boldsymbol{l} + i\phi_{\boldsymbol{n}+\hat{\boldsymbol{x}}} - i\phi_{\boldsymbol{n}} \right) \\ &\quad + \exp\left(-2i \int_{\boldsymbol{n}}^{\boldsymbol{n}-\hat{\boldsymbol{x}}} e\boldsymbol{A}\cdot d\boldsymbol{l} + i\phi_{\boldsymbol{n}-\hat{\boldsymbol{x}}} - i\phi_{\boldsymbol{n}} \right) \\ &\quad - \exp\left(-2i \int_{\boldsymbol{n}}^{\boldsymbol{n}+\hat{\boldsymbol{y}}} e\boldsymbol{A}\cdot d\boldsymbol{l} + i\phi_{\boldsymbol{n}+\hat{\boldsymbol{y}}} - i\phi_{\boldsymbol{n}} \right) \\ &\quad - \exp\left(-2i \int_{\boldsymbol{n}}^{\boldsymbol{n}-\hat{\boldsymbol{y}}} e\boldsymbol{A}\cdot d\boldsymbol{l} + i\phi_{\boldsymbol{n}-\hat{\boldsymbol{y}}} - i\phi_{\boldsymbol{n}} \right) \Bigg], \end{aligned} \tag{2.44b}$$

$$t_{ee}(\boldsymbol{n}+\hat{\boldsymbol{\delta}},\boldsymbol{n}) = -t_0 \exp\left(i \int_{\boldsymbol{n}}^{\boldsymbol{n}+\hat{\boldsymbol{\delta}}} e\boldsymbol{A}\cdot d\boldsymbol{l} - i\phi_{\boldsymbol{n}+\hat{\boldsymbol{\delta}}} + i\phi_{\boldsymbol{n}} \right), \tag{2.44c}$$

$$t_{hh}(\boldsymbol{n}+\hat{\boldsymbol{\delta}},\boldsymbol{n}) = -t_0 \exp\left(-i \int_{\boldsymbol{n}}^{\boldsymbol{n}+\hat{\boldsymbol{\delta}}} e\boldsymbol{A}\cdot d\boldsymbol{l} \right), \tag{2.44d}$$

$$\begin{aligned} t_{eh}(\boldsymbol{n}+\hat{\boldsymbol{\delta}},\boldsymbol{n}) &= t_{he}^*(\boldsymbol{n},\boldsymbol{n}+\hat{\boldsymbol{\delta}}) \\ &= \tfrac{1}{2}\Delta_0 \Bigg[\exp\left(i \int_{\boldsymbol{n}}^{\boldsymbol{n}+\hat{\boldsymbol{\delta}}} e\boldsymbol{A}\cdot d\boldsymbol{l} - i\phi_{\boldsymbol{n}+\hat{\boldsymbol{\delta}}} + i\phi_{\boldsymbol{n}} \right) \\ &\quad + \exp\left(-i \int_{\boldsymbol{n}}^{\boldsymbol{n}+\hat{\boldsymbol{\delta}}} e\boldsymbol{A}\cdot d\boldsymbol{l} \right) \Bigg] \times \begin{cases} -1 & \text{if } \hat{\boldsymbol{\delta}} = \pm\hat{\boldsymbol{x}}, \\ +1 & \text{if } \hat{\boldsymbol{\delta}} = \pm\hat{\boldsymbol{y}}. \end{cases} \end{aligned} \tag{2.44e}$$

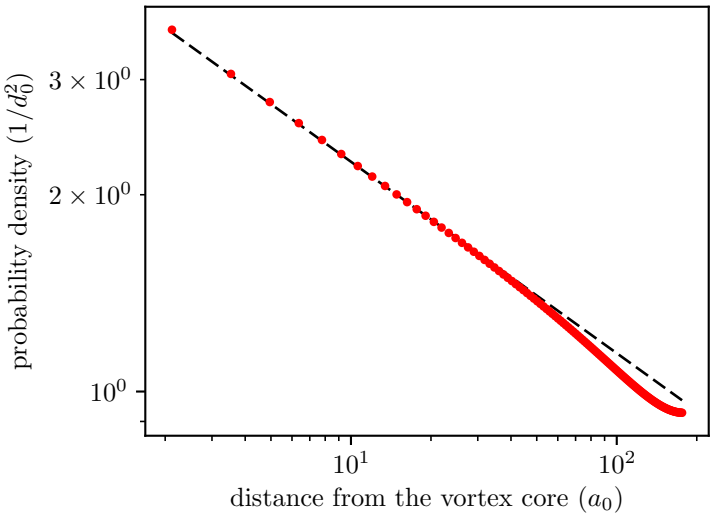

Figure 2.7: Red data points: Dependence of the probability density $|\psi(x, y)|^2$ on the distance from a vortex core along the line $x = y$, calculated in the zeroth Landau level at momentum $\boldsymbol{k} = (\pi/2, \pi/2, \pi/3)$, for parameters $\Delta_0 = 1$, $\beta = \sqrt{2}$, $\mu = 0$, $d_0 = 502\, a_0$. We took a weaker magnetic field than in Fig. 2.4 (which had a vortex array with lattice constant $d_0 = 202\, a_0$), so that the vortices are more widely separated and we can extract the single-vortex asymptotics more easily. The slope of the dashed line is the analytical prediction (2.46).

2.C Quasiparticle density profile near the vortex core

In the main text we showed that our numerical simulations reproduce the dispersion relation expected from the analytical theory: The dispersionless zeroth Landau level in the plane perpendicular to the applied magnetic field, see Fig. 2.2b, and the linear dispersion along the field, see Fig. 2.3. We also checked that the numerical result $q_{\text{eff}} \approx \pm 0.73\, e$ for the effective charge of the quasiparticles at the Weyl point is close to the analytical prediction:

$$|q_{\text{eff}}/e| = \sqrt{1 - \Delta_0^2/\beta^2} = 1/\sqrt{2} \approx 0.71. \tag{2.45}$$

As a further test, we compare in Fig. 2.7 the dependence of the quasiparticle density $|\psi|^2$ on the distance δr from a vortex core. The analytical

prediction from Eq. (2.13),

$$|\psi|^2 \simeq \delta r^{-1+|q_{\rm eff}|/e} = \delta r^{-1+1/\sqrt{2}}, \tag{2.46}$$

is in excellent agreement with the numerics.

2.D Arbitrary angle between internal magnetization and external magnetic field

The four-band Hamiltonian (2.17) of the Weyl semimetal has an internal magnetization β pointing in the z-direction, parallel to the external magnetic field $\boldsymbol{B} = B_0\hat{z}$. If instead the magnetization vector $\boldsymbol{\beta} = (\beta_x, \beta_y, \beta_z)$ points in an arbitrary direction, the Hamiltonian becomes

$$\begin{aligned} H_0(\boldsymbol{k}) = t_0 \sum_{\alpha=x,y,z} &[\tau_z\sigma_\alpha \sin k_\alpha a_0 + \tau_x\sigma_0(1-\cos k_\alpha a_0)] \\ &+ \tau_0\, \boldsymbol{\beta}\cdot\boldsymbol{\sigma} - \mu\tau_0\sigma_0. \end{aligned} \tag{2.47}$$

Numerical results for the spectrum are shown in Fig. 2.8 for a magnetization at a 45° degree angle and at a 90° angle with the magnetic field. The zeroth Landau level remains dispersionless in the x–y plane.

We note that now the Weyl cone is anisotropic in the x–y plane, but that also does not spoil the protection of the zeroth Landau level.

2.E Tilting of the Weyl cones

To further explore the robustness of the zeroth Landau level, we consider what happens if we break Lorentz invariance by tilting the Weyl cones. Following Ref. 44 one distinguishes type-I from type-II Weyl cones, depending on whether the equi-energy contours are closed elliptic (type-I) or open hyperbolic (type-II). In the absence of superconductivity, it is known that the topological protection of the zeroth Landau level persists all the way up to the Lifshitz transition from a type-I to a type-II Weyl semimetal [45, 46]. Here we show that the same applies in the superconducting vortex lattice.

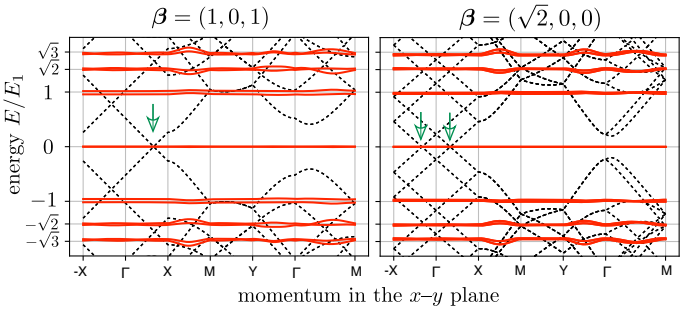

Figure 2.8: Same as Fig. 2.1b, but for an internal magnetization $\boldsymbol{\beta}$ that is rotated away from the magnetic field $\boldsymbol{B}$ in the z-direction. The Weyl points are at $\boldsymbol{K} = \pm(0.684, 0, 0.684)$ for $\beta = (1,0,1)$ and at $\boldsymbol{K} = \pm(\pi/3, 0, 0)$ for $\beta = (\sqrt{2},0,0)$, in each case aligned along the magnetization. The (k_x, k_y) momentum is varied along the path through the magnetic Brillouin zone of Fig. 2.2b, at fixed $k_z = K_z$, so it passes through one Weyl point for $\beta = (1,0,1)$ and through two Weyl points for $\beta = (\sqrt{2},0,0)$ (green arrows). The flatness of the Landau levels in the vortex lattice is essentially unaffected by the rotation of the magnetization, but the energies themselves are shifted because of the anisotropic Fermi velocity: $E_n = \sqrt{n}\, E_1$, with $E_1 = (2/d_0)\sqrt{\pi v_x v_y}$, and $v_x = 1$, $v_y = 0.774$ for $\beta = (1,0,1)$; $v_x = 1$, $v_y = 0.612$ for $\beta = (\sqrt{2},0,0)$.

2.E.1 Hamiltonian of a type-I Weyl supserconductor

We break Lorentz-invariance (particle-hole symmetry) of the Hamiltonian (2.4) by adding momentum dependent terms proportional to the unit matrix,

$$H_0(\boldsymbol{k}) = v_{\mathrm{F}}\tau_z \boldsymbol{k}\cdot\boldsymbol{\sigma} + \beta\tau_0\sigma_z - \mu\tau_0\sigma_0 - v_{\mathrm{F}}(\boldsymbol{\eta}\cdot\boldsymbol{k})\tau_0\sigma_0. \tag{2.48}$$

The Weyl cones are tilted in the direction of the vector $\boldsymbol{\eta}$. To simplify the equations we orient the x–y axes so that the cones are tilted in the x–z plane, hence without loss of generality we may set $\eta_y = 0$ (allowing for both η_x and η_z to be nonzero). The equi-energy contours are closed elliptic (type-I Weyl cone) for $|\boldsymbol{\eta}| < 1$.

The low-energy Hamiltonian, obtained by the unitary transformation (2.5) followed by a projection on the $\nu = \tau = \pm 1$ subspace, is

$$\begin{aligned} H_\pm(\boldsymbol{k}) = {} & v_{\mathrm{F}}\textstyle\sum_{\alpha=x,y}(k_\alpha + a_\alpha \pm \kappa m v_{\mathrm{s},\alpha})(\sigma_\alpha - \eta_\alpha\sigma_0) \\ & + (\beta - m_{k_z})\sigma_z \mp \kappa\mu\sigma_0 - v_{\mathrm{F}} k_z \eta_z \sigma_0. \end{aligned} \tag{2.49}$$

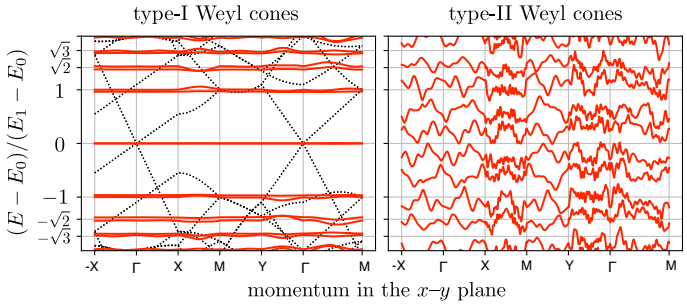

Figure 2.9: Same as Fig. 2.1b, but for tilted Weyl cones with $\boldsymbol{\eta} = (0.5, 0, 0.05)$ (left panel) and $\boldsymbol{\eta} = (1.1, 0, 0)$ (right panel). The energies are shifted by $E_0 = -v_\mathrm{F}\eta_z \sin K$. The energy E_1 of the first Landau level was calculated numerically. In the type-I regime $|\boldsymbol{\eta}| < 1$ the Landau levels remain intact. For $|\boldsymbol{\eta}| > 1$ the Weyl superconductor goes through a Lifshitz transition to type-II Weyl cones and the Landau levels disappear.

For $|k_z| = K$ at the Weyl point, this reduces to

$$H_\pm(\boldsymbol{k}) = H_\mathrm{chiral} + E_\pm \sigma_0, \quad E_\pm = \mp\kappa\mu - v_\mathrm{F} K \eta_z, \tag{2.50}$$

where H_chiral differs from Eq. (2.8) by the appearance of diagonal terms,

$$H_\mathrm{chiral} = v_\mathrm{F} \begin{pmatrix} -\eta_x \Pi_x & \Pi_x - i\Pi_y \\ \Pi_x + i\Pi_y & -\eta_x \Pi_x \end{pmatrix}. \tag{2.51}$$

2.E.2 Generalized chiral symmetry protects the zeroth Landau level

The Hamiltonian (2.51) no longer anticommutes with σ_z, so chiral symmetry is broken. However, following Refs. 45, 46, for $|\eta_x| < 1$ we can generalize the chiral symmetry relation by means of the non-Hermitian operator

$$\gamma = \lambda^{-1} \sigma_z (\sigma_0 - \eta_x \sigma_x), \quad \lambda = \sqrt{1 - \eta_x^2}, \tag{2.52}$$

such that

$$\gamma^\dagger H_\mathrm{chiral} + H_\mathrm{chiral} \gamma = 0, \quad \gamma^2 = 1. \tag{2.53}$$

The right eigenvectors of γ are

$$\begin{aligned} |+\rangle &= \frac{1}{\sqrt{2+2\lambda}} \begin{pmatrix} 1+\lambda \\ \eta_x \end{pmatrix}, \\ |-\rangle &= \frac{1}{\sqrt{2+2\lambda}} \begin{pmatrix} \eta_x \\ 1+\lambda \end{pmatrix}, \end{aligned} \tag{2.54}$$

with $\gamma|\pm\rangle = \pm|\pm\rangle$. The generalized chirality relation (2.53) implies that

$$\langle +|H_{\rm chiral}|+\rangle = 0 = \langle -|H_{\rm chiral}|-\rangle. \tag{2.55}$$

Upon substitution of $|\psi\rangle = \psi_+|+\rangle + \psi_-|-\rangle$ the zero-mode equation $H|\psi\rangle = 0$ takes the form

$$\begin{pmatrix} 0 & \tilde{\mathcal{D}} \\ \tilde{\mathcal{D}}^\dagger & 0 \end{pmatrix} \begin{pmatrix} \psi_+ \\ \psi_- \end{pmatrix} = 0, \;\; \tilde{\mathcal{D}} = \frac{1}{v_{\rm F}\lambda}\langle +|H_{\rm chiral}|-\rangle. \tag{2.56}$$

The matrix elements on the diagonal vanish in view of Eq. (2.55). The off-diagonal term $\tilde{\mathcal{D}}$ equals

$$\tilde{\mathcal{D}} = \lambda\Pi_x - i\Pi_y. \tag{2.57}$$

This is almost of the form (2.8), except for the factor-λ rescaling of Π_x. If rescale the coordinates as $x' = x/\lambda$, $y' = y$, and the gauge potential as $\mathcal{A}'_x = \lambda\mathcal{A}_x$, $\mathcal{A}'_y = \mathcal{A}_y$, we have equivalently

$$\tilde{\mathcal{D}} = \Pi'_x - i\Pi'_y, \;\; \mathbf{\Pi}' = -i\nabla' + e\mathcal{A}'. \tag{2.58}$$

The rescaling does not affect the existence of the zeroth Landau level, nor its degeneracy, since the enclosed flux is unchanged:

$$\begin{aligned} \Phi' &= \int dx' \int dy' \, (\partial_{x'}\mathcal{A}'_y - \partial_{y'}\mathcal{A}'_x) \\ &= \int \frac{dx}{\lambda} \int dy \, (\lambda\partial_x\mathcal{A}_y - \partial_y\lambda\mathcal{A}_x) \\ &= \int dx \int dy \, (\partial_x\mathcal{A}_y - \partial_y\mathcal{A}_x) = \Phi. \end{aligned} \tag{2.59}$$

We conclude that the zeroth Landau level remains topologically protected against scattering by the superconducting vortex lattice even if Lorentz invariance is broken by tilting the Weyl cones — up to the Lifshitz transition at $|\boldsymbol{\eta}| = 1$ from type-I to type-II Weyl cones[10]. In Fig. 2.9 we show numerical data that confirms this conclusion from the analytics.

[10] Because the generalized chiral symmetry of tilted Weyl cones requires $\eta_x^2 + \eta_y^2 < 1$, irrespective of the tilt η_z in the z-direction, the protection of the zeroth Landau level for nonzero η_z extends somewhat beyond the Lifshitz transition at $\eta_x^2+\eta_y^2+\eta_z^2 = 1$.

2.E.3 Chiral dispersion along the magnetic field

To complete the calculation we examine the dispersion of the zeroth Landau level in the k_z-direction, parallel to the magnetic field. We go back to the Hamiltonian (2.49), without setting $k_z = K$. In the basis (2.54) the eigenvalue equation $(H - E)|\psi\rangle = 0$ takes the form

$$\begin{pmatrix} \mathcal{E}_2 + \lambda\mathcal{E}_1 & v_\mathrm{F}\lambda\tilde{\mathcal{D}} + \eta_x\mathcal{E}_2 \\ v_\mathrm{F}\lambda\tilde{\mathcal{D}}^\dagger + \eta_x\mathcal{E}_2 & \mathcal{E}_2 - \lambda\mathcal{E}_1 \end{pmatrix} \begin{pmatrix} \psi_+ \\ \psi_- \end{pmatrix} = 0,$$
$$\mathcal{E}_1 = \beta - m_{k_z}, \quad \mathcal{E}_2 = \mp\kappa\mu - v_\mathrm{F}k_z\eta_z - E. \tag{2.60}$$

We seek a solution

$$\begin{pmatrix} \psi_+ \\ \psi_- \end{pmatrix} = \begin{pmatrix} \exp(ix\eta_x\mathcal{E}_1/v_\mathrm{F}\lambda)\phi_+ \\ \exp(-ix\eta_x\mathcal{E}_1/v_\mathrm{F}\lambda)\phi_- \end{pmatrix} \tag{2.61}$$

with either $\phi_+ \equiv 0$ or $\phi_- \equiv 0$. Substitution into Eq. (2.60) gives

$$\begin{aligned} \text{either } \ \phi_+ \equiv 0 \Rightarrow \tilde{\mathcal{D}}\phi_- = 0 \ \text{ and } \ \mathcal{E}_2 = \lambda\mathcal{E}_1, \\ \text{or } \ \phi_- \equiv 0 \Rightarrow \tilde{\mathcal{D}}^\dagger\phi_+ = 0 \ \text{ and } \ \mathcal{E}_2 = -\lambda\mathcal{E}_1. \end{aligned} \tag{2.62}$$

The boundary condition (2.14) on the vortex core selects one of these two solutions, depending on the sign of the effective charge q_eff.

We conclude that the zeroth Landau level has the k_z-dispersion

$$E_\pm(k_z) = (\operatorname{sign} q_\mathrm{eff})(\lambda\beta - \lambda m_{k_z}) \mp \kappa\mu - v_\mathrm{F}k_z\eta_z. \tag{2.63}$$

For $\boldsymbol{\eta} = 0$, $\lambda = 1$ we recover the dispersion (2.15) for untilted Weyl cones. The Landau level remains dispersionless in the k_x–k_y plane for any k_z.

3 Effect of charge renormalization on electric and thermo-electric transport along the vortex lattice of a Weyl superconductor

3.1 Introduction

Weyl superconductors are nodal superconductors with topological protection [12, 53]: They have nodal points of vanishing excitation gap, just like d-wave superconductors [54], but in contrast to those the gapless states are not restricted to high-symmetry points in the Brillouin zone and can appear for conventional s-wave pairing. The nodal points (Weyl points) at $\pm K$ in a Weyl superconductor are protected by the conservation of a topological invariant: the Berry flux of $\pm 2\pi$ at Weyl points of opposite chirality [55, 56].

The distinction between symmetry and topology has a major consequence for the stability of Landau levels in a magnetic field. While in a d-wave superconductor the strong scattering of nodal fermions by vortices in the order parameter prevents the formation of Landau levels [1], in a Weyl superconductor an index theorem for chiral fermions protects the zeroth Landau level from broadening [57]. The appearance of chiral Landau levels in a superconducting vortex lattice produces a quantized thermal conductance parallel to the magnetic field, in units of $1/2$ times the thermal quantum per $h/2e$ vortex [57]. The factor of $1/2$ reminds us that Bogoliubov quasiparticles are Majorana fermions, "half a Dirac fermion" [58, 59].

In this chapter we turn from thermal transport to electrical transport, by studying the geometry of Fig. 3.1 and addressing the question "What

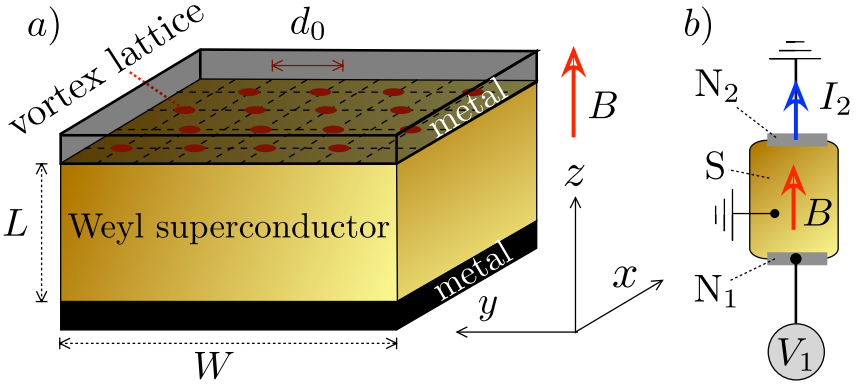

Figure 3.1: a) Vortex lattice in a Weyl superconductor sandwiched between metal electrodes; b) Circuit to measure the electrical transport along the vortex lines. The nonlocal conductance $G_{12} = dI_2/dV_1$ gives the current carried through the vortex lattice by nonequilibrium Weyl fermions in a chiral Landau level.

is the charge transported along the vortices in a chiral Landau level?" It is known [48] that the charge of Weyl fermions in a superconductor (pair potential Δ_0) is reduced by a factor $\kappa = K(\Delta_0)/K(0)$. We find a direct manifestation of this charge renormalization in the electrical conductance, which is quantized at $\frac{1}{2}(e\kappa)^2/h$ per vortex. Because the charge renormalization is energy dependent, a coupling between thermal and electrical transport appears even without any energy-dependent scattering mechanism — resulting in a nonzero thermo-electric effect in a chiral Landau level.

In the next section 3.2 we summarize the effective low-energy theory of the superconducting vortex lattice [57], on which we base our scattering theory in Sec. 3.3, followed by a calculation of electrical and thermo-electric transport properties in Sec. 3.4. These analytical results are compared with numerical simulations of a tight-binding model in Sec. 3.5. We conclude in Sec. 3.6.

3.2 Landau level Hamiltonian in the vortex lattice

We summarize the findings of Ref. 57 for the Landau level Hamiltonian of Weyl fermions in a superconducting vortex lattice, which we will need

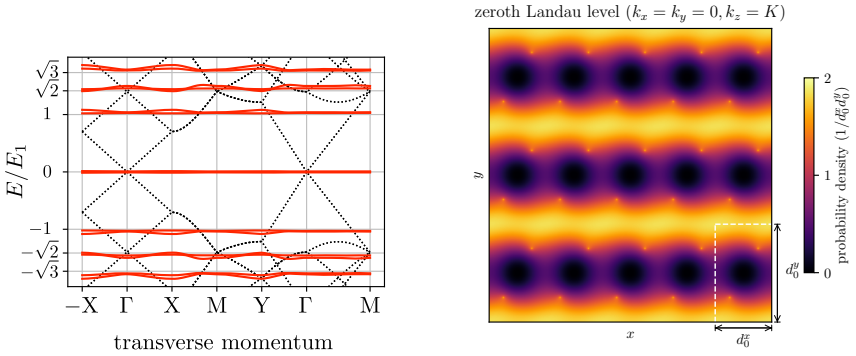

Figure 3.2: *Left panel:* The red solid curves show the dispersion of Landau levels in the k_x–k_y plane perpendicular to the magnetic field (energy E normalized by the energy E_1 of the first Landau level). The black dotted curves show the dispersion in zero magnetic field, with a Weyl cone at the Γ point of the magnetic Brillouin zone. *Right panel:* Particle density profile in the zeroth Landau level, in the x–y plane perpendicular to the magnetic field, for a wave vector at the Weyl point ($\boldsymbol{k} = K\hat{z}$). The magnetic unit cell is indicated by a white dashed rectangle. Both panels are calculated numerically for a Weyl superconductor with a triangular vortex lattice. The vortex cores are located at the bright points in the density profile. Similar plots for a square vortex lattice are in Ref. 57.

to calculate the transport properties.

3.2.1 Dispersion relation

A Landau level is a dispersionless flat band in the plane perpendicular to the magnetic field. The lowest (zeroth) Landau level is protected by chiral symmetry from scattering by the vortices, see Fig. 3.2. This is the Landau level on which we focus our analysis. It is a celebrated result of Nielsen and Ninomiya [55] that Weyl fermions in the zeroth Landau level have a definite chirality $\chi = \pm 1$, defined as the sign of the velocity $v_z = \partial E/\partial k_z$, parallel or antiparallel to B. To account for the electron-hole degree of freedom the number of bands is doubled for each chirality, so that we have four bands in total. Electron-like and hole-like bands are related related by the charge-conjugation symmetry relation $E_\chi(k_z) = -E_\chi(-k_z)$.

The effect of a superconducting vortex lattice on this four-band disper-

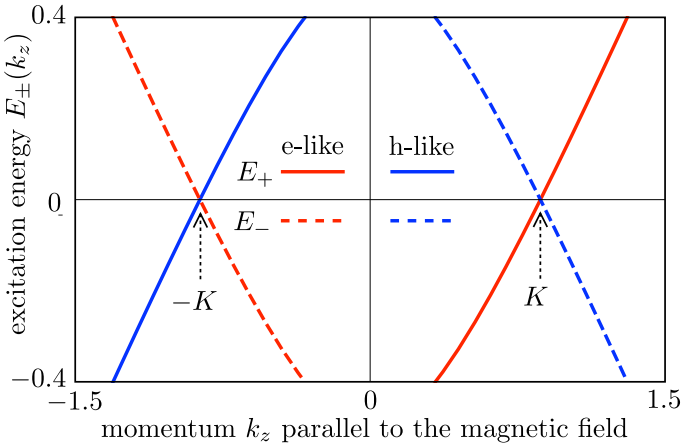

Figure 3.3: Dispersion relation of the zeroth Landau level in a superconducting vortex lattice, plotted from Eq. (3.1) for $\mu = 0$, $\Delta_0 = 0.5$, $\beta = 1$. Only the dependence on the momentum k_z along the magnetic field B is shown, the dispersion is flat in the x–y plane (see Fig. 3.2). The four branches are distinguished by the sign of the chirality (solid or dashed) and by the sign of the electric charge (red or blue). The zero-field Weyl points at $k_z = \pm K$ are indicated by arrows. Each branch has a degeneracy $N_{\text{Landau}} = e\Phi/h$ set by the enclosed flux $\Phi = BW^2$.

sion is given by [57]

$$\begin{aligned} E_\chi(k_z) &= -(\operatorname{sgn} k_z)\chi M(k_z) - \chi\mu\kappa(k_z), \\ M(k_z) &= \beta - \sqrt{\Delta_0^2 + k_z^2}, \quad \kappa(k_z) = \frac{d}{dk_z} M(k_z), \end{aligned} \tag{3.1}$$

plotted in Fig. 3.3. (We have set $\hbar$ and the Fermi velocity v_{F} equal to unity, so κ is dimensionless.) The magnitude of the superconducting pair potential outside of the vortex cores is denoted by Δ_0 and β is an internal magnetization along the z-direction that breaks time-reversal symmetry even in the absence of any external magnetic field. In Eq. (3.1) we have assumed that β is parallel to B, but we will later relax this assumption (see Sec. 3.5.3).

Provided that $\Delta_0 < \beta$ there is a pair of Landau levels for each chirality, located in the magnetic Brillouin zone near the Weyl points at $k_z = K$ and $k_z = -K$, with [12]

$$K(\Delta_0) = \sqrt{\beta^2 - \Delta_0^2}. \tag{3.2}$$

The charge expectation value

$$Q_\chi = -e\frac{\partial E_\chi}{\partial \mu} = e\chi\kappa(k_z) = -\frac{e\chi k_z}{\sqrt{\Delta_0^2 + k_z^2}} \tag{3.3}$$

for a given chirality has the opposite sign at the two Weyl points. (We say that the chiral Landau levels near $k_z = \pm K$ are charge-conjugate.) When $k_z = \pm K$ is at the Weyl point, the charge renormalization factor equals $\mp\kappa_0$, with

$$\kappa_0 = K(\Delta_0)/K(0) = \sqrt{1 - \Delta_0^2/\beta^2}, \tag{3.4}$$

while $\kappa(k_z)$ varies linearly with energy away from the Weyl point [48].

3.2.2 Effective Hamiltonian

The dispersion (3.1) follows from the effective low-energy Hamiltonian [57]

$$\mathcal{H} = U\begin{pmatrix} H_+ & 0 & 0 & 0 \\ 0 & \cdot & \cdot & 0 \\ 0 & \cdot & \cdot & 0 \\ 0 & 0 & 0 & H_- \end{pmatrix}U^\dagger, \tag{3.5a}$$

$$H_\chi = (k_x + e\mathcal{A}_{\chi,x})\sigma_x + (k_y + e\mathcal{A}_{\chi,y})\sigma_y + M\sigma_z - \chi\mu\kappa\sigma_0, \tag{3.5b}$$

$$U = \exp(\tfrac{1}{2}i\theta\nu_y\tau_z\sigma_z), \quad \theta = \arccos\kappa. \tag{3.5c}$$

The 2×2 Pauli matrices ν_α, τ_α, and σ_α (with $\alpha = 0$ the corresponding unit matrix) act on, respectively, the electron-hole, orbital, and spin degrees of freedom. The full Hamiltonian $\mathcal{H}$ is an 8×8 matrix and the 2×2 matrices $H_\pm$ act on the σ index in the $\nu = \tau = \pm1$ sector.

The central block in Eq. (3.5a) indicated by dots refers to higher-lying bands that are approximately decoupled from the low-energy bands. Virtual transitions to these higher bands contribute order μ^2 terms that remove the discontinuity in the derivative $\partial E/\partial k_z$ at $k_z = 0$ for $\mu \neq 0$. No such decoupling approximations are made in the numerics of Sec. 3.5.

The gauge field $\mathcal{A}_\chi(\boldsymbol{r})$, dependent on the position $\boldsymbol{r} = (x, y)$ in the x–y plane, defines the effective magnetic field $\mathcal{B}_\chi = \nabla\times\mathcal{A}_\chi$ in the z-direction felt by the Weyl fermions in the lattice of vortices at positions $\boldsymbol{R}_n$,

$$\mathcal{B}_\chi = (1 + \chi\kappa)\Phi_0\sum_n \delta(\boldsymbol{r} - \boldsymbol{R}_n) - \chi\kappa B. \tag{3.6}$$

There are $N_{\text{vortex}} = BW^2/\Phi_0$ vortices of flux $\Phi_0 = h/2e$ in an area W^2 perpendicular to the applied magnetic field B, so the spatial average $\int \mathcal{B}_\chi d\boldsymbol{r} = \Phi$ equals the total enclosed flux $\Phi = BW^2$ independent of κ or of the lattice of vortices. (In the numerics that follows we will use a square lattice for definiteness.)

3.2.3 Zeroth Landau level wave functions

As shown in Ref. 57, the Aharonov-Casher index theorem [16, 49, 50], together with the requirement that the wave functions are square-integrable at a vortex core, implies that the zeroth Landau level eigenstates ψ_χ of H_χ, which are rank-two spinors, are also eigenstates $|\pm\rangle_\sigma$ of σ_z,

$$\sigma_z \psi_\chi = (\operatorname{sgn} Q_\chi)\psi_\chi. \tag{3.7}$$

The eigenvalue is determined by the sign of the effective quasiparticle charge (3.3).

It follows that the eigenstates Ψ_χ of the full Hamiltonian $\mathcal{H}$, which are rank-eight spinors, have the form

$$\begin{aligned}\Psi_\chi &= e^{ik_z z} f_\chi(x,y) e^{\frac{1}{2} i\theta \nu_y \tau_z \sigma_z} |\operatorname{sgn}\chi\rangle_\nu |\operatorname{sgn}\chi\rangle_\tau |\operatorname{sgn} Q_\chi\rangle_\sigma \\ &= e^{ik_z z} f_\chi(x,y)\big[\cos(\theta/2)|\operatorname{sgn}\chi\rangle_\nu|\operatorname{sgn}\chi\rangle_\tau|\operatorname{sgn} Q_\chi\rangle_\sigma \\ &\quad - \sin(\theta/2)(\operatorname{sgn} Q_\chi)|-\operatorname{sgn}\chi\rangle_\nu|\operatorname{sgn}\chi\rangle_\tau|\operatorname{sgn} Q_\chi\rangle_\sigma\big].\end{aligned} \tag{3.8}$$

The spatial density profile $f_\chi(x,y)$ is peaked at the vortex cores, with a power law decay $|f_\chi|^2 \propto \delta r^{-1+|Q_\chi|/e}$ at a distance δr from the core [57]. The renormalization of the quasiparticle charge does not affect the degeneracy of the zeroth Landau level: each of the four chiral modes in Fig. 3.3 has a degeneracy

$$N_{\text{Landau}} = e\Phi/h \tag{3.9}$$

set by the bare charge e.

Although the spatial density profile of these chiral modes is nonuniform, the wave functions extend over the entire x–y plane — they are not exponentially confined to the vortex cores (see Fig. 3.2). This is a qualitative difference between the zeroth Landau level of a Weyl superconductor and zero-modes bound to vortices in topological superconductors [14, 60].

3.3 Transmission through the NSN junction

Refering to the geometry of Fig. 3.1, we seek the transmission matrix t_{NSN} for propagating modes of electrons and holes transmitted from the first

metal contact N_1 in the region $z < 0$, through the Weyl superconductor in the region $0 < z < L$, into the second metal contact N_2 in the region $z > L$.

3.3.1 Renormalized charge transfer

We start by examining a single NS interface, to study how a chiral mode in the superconductor injects a renormalized charge into the normal metal.

On the superconducting side $z < L$ of the NS interface at $z = L$ the incident modes have positive chirality $\chi = +1$. There is a mode Ψ_{S} with perpendicular momentum k_z near K and a mode Ψ'_{S} with k'_z near $-K$. We do not specify the transverse momentum $\boldsymbol{k}_{\parallel} = (k_x, k_y)$, which gives each mode a degeneracy of $N_{\mathrm{Landau}} = e\Phi/h$, see Eq. (3.9).

According to Eq. (3.8), the spinor structure of the chiral modes is

$$\begin{aligned} \Psi_{\mathrm{S}} &\propto \cos(\theta/2)|{+}{+}{-}\rangle_{\nu\tau\sigma} + \sin(\theta/2)|{-}{+}{-}\rangle_{\nu\tau\sigma}, \\ \Psi'_{\mathrm{S}} &\propto \cos(\theta'/2)|{+}{+}{+}\rangle_{\nu\tau\sigma} - \sin(\theta'/2)|{-}{+}{+}\rangle_{\nu\tau\sigma}. \end{aligned} \tag{3.10}$$

We have abbreviated $|\pm\pm\pm\rangle_{\nu\tau\sigma} = |\pm\rangle_{\nu}|\pm\rangle_{\tau}|\pm\rangle_{\sigma}$ and denote $\theta = \theta(k_z)$, $\theta' = \theta(k'_z)$.

For the normal metal we take the free-electron Hamiltonian

$$H_{\mathrm{N}} = \frac{1}{2m}(k^2 - k_{\mathrm{F}}^2)\nu_z\tau_0\sigma_0, \tag{3.11}$$

isotropic in the spin and valley degrees of freedom, in the high Fermi-momentum limit $k_{\mathrm{F}}l_m \to \infty$ when the effect of the magnetic field on the spectrum may be neglected ($l_m = \sqrt{\hbar/eB}$ is the magnetic length).

Because of the large potential step experienced upon traversing the NS interface, the perpendicular momentum k_z is boosted to $+k_{\mathrm{F}}$ for the electron component of the state and to $-k_{\mathrm{F}}$ for the hole component. A state in N moving away from the NS interface of the form

$$\begin{aligned} \Psi_{\mathrm{N}} \propto\ & e^{ik_{\mathrm{F}}(z-L)}\cos(\theta/2)|{+}{+}{-}\rangle_{\nu\tau\sigma} \\ & + e^{-ik_{\mathrm{F}}(z-L)}\sin(\theta/2)|{-}{+}{-}\rangle_{\nu\tau\sigma} \end{aligned} \tag{3.12a}$$

can be matched to the incident state Ψ_S in S, while the state

$$\begin{aligned} \Psi'_{\mathrm{N}} \propto\ & e^{ik_{\mathrm{F}}(z-L)}\cos(\theta'/2)|{+}{+}{+}\rangle_{\nu\tau\sigma} \\ & - e^{-ik_{\mathrm{F}}(z-L)}\sin(\theta'/2)|{-}{+}{+}\rangle_{\nu\tau\sigma} \end{aligned} \tag{3.12b}$$

can be matched to Ψ'_S.

The charge transferred through the interface when $\Psi_S \mapsto \Psi_N$ equals the renormalized charge from Eq. (3.3),

$$Q_N = \langle \Psi_N | e\nu_z | \Psi_N \rangle = e\cos\theta = e\kappa = \frac{-ek_z}{\sqrt{\Delta_0^2 + k_z^2}}, \tag{3.13}$$

dependent on the perpendicular momentum k_z in S, before the boost to k_F in N. When $k_z = K$, this gives

$$Q_N = -e\sqrt{1 - \Delta_0^2/\beta^2} = -\kappa_0 e \equiv -Q_{\text{eff}}. \tag{3.14}$$

This is for the transmission $\Psi_S \mapsto \Psi_N$. The other transmission $\Psi'_S \mapsto \Psi'_N$ transfers for $k'_z = -K$ a charge $Q'_N = +Q_{\text{eff}}$.

Similarly, at the opposite NS interface $z = 0$ the chiral Landau level modes in S moving away from the interface are matched to incoming states in N of the form

$$\begin{aligned} \Phi_N \propto\ & e^{ik_F z}\cos(\theta/2)|{+}{+}{-}\rangle_{\nu\tau\sigma} \\ & + e^{-ik_F z}\sin(\theta/2)|{-}{+}{-}\rangle_{\nu\tau\sigma}, \end{aligned} \tag{3.15a}$$

$$\begin{aligned} \Phi'_N \propto\ & e^{ik_F z}\cos(\theta'/2)|{+}{+}{+}\rangle_{\nu\tau\sigma} \\ & - e^{-ik_F z}\sin(\theta'/2)|{-}{+}{+}\rangle_{\nu\tau\sigma}. \end{aligned} \tag{3.15b}$$

3.3.2 Transmission matrix

At a given energy E relative to the Fermi level the perpendicular momenta k_z and k'_z of the chiral Landau levels in S moving in the $+z$ direction are determined by the dispersion relation (3.1) with $\chi = +1$. For $\mu = 0$ the expressions are simple,

$$k_z = K + (\beta/K)E, \quad k'_z = -K + (\beta/K)E. \tag{3.16}$$

For any μ, particle-hole symmetry ensures that

$$k_z(E) = -k'_z(-E). \tag{3.17}$$

The Landau level Ψ_S propagating from $z = 0$ to $z = L$ accumulates a phase $k_z L$, and similarly Ψ'_S accumulates a phase $k'_z L$. The full transmission matrix of the NSN junction at energy E can thus be written as

$$t_{NSN}(E) = e^{ik_z L}|\Psi_N\rangle\langle\Phi_N| + e^{ik'_z L}|\Psi'_N\rangle\langle\Phi'_N|, \tag{3.18}$$

with k_z and k'_z determined by Eq. (3.16).

We can rewrite Eq. (3.18) in the basis of propagating electron modes in the normal metal. In the region $z < 0$ one has the basis states

$$|\Psi_\uparrow\rangle = \begin{pmatrix} |e\uparrow\rangle \\ |h\uparrow\rangle \end{pmatrix}, \quad |\Psi_\downarrow\rangle = \begin{pmatrix} |e\downarrow\rangle \\ |h\downarrow\rangle \end{pmatrix}, \tag{3.19a}$$

$$|e\uparrow\rangle = e^{ik_\mathrm{F}z}|{+}{+}{+}\rangle_{\nu\tau\sigma}, \quad |h\uparrow\rangle = e^{-ik_\mathrm{F}z}|{-}{+}{+}\rangle_{\nu\tau\sigma},$$
$$|e\downarrow\rangle = e^{ik_\mathrm{F}z}|{+}{+}{-}\rangle_{\nu\tau\sigma}, \quad |h\downarrow\rangle = e^{-ik_\mathrm{F}z}|{-}{+}{-}\rangle_{\nu\tau\sigma}, \tag{3.19b}$$

and similarly for $z > L$ with $k_\mathrm{F}z$ replaced by $k_\mathrm{F}(z-L)$.

The transmission matrix is block diagonal in the spin degree of freedom,

$$t_\mathrm{NSN}(E) = \begin{pmatrix} t_\uparrow(E) & 0 \\ 0 & t_\downarrow(E) \end{pmatrix}, \tag{3.20a}$$

$$t_\uparrow = e^{ik'_z L}\begin{pmatrix} \cos^2(\theta'/2) & -\cos(\theta'/2)\sin(\theta'/2) \\ -\cos(\theta'/2)\sin(\theta'/2) & \sin^2(\theta'/2) \end{pmatrix},$$
$$t_\downarrow = e^{ik_z L}\begin{pmatrix} \cos^2(\theta/2) & \cos(\theta/2)\sin(\theta/2) \\ \cos(\theta/2)\sin(\theta/2) & \sin^2(\theta/2) \end{pmatrix}. \tag{3.20b}$$

The 2×2 matrix $t_\uparrow$ acts on the electron-hole spinor $|\Psi_\uparrow\rangle$ and $t_\downarrow$ acts on $|\Psi_\downarrow\rangle$. We may write this more compactly as

$$\begin{aligned} t_\uparrow &= \tfrac{1}{2}e^{ik'_z L}\Big(\nu_0 + \nu_z e^{-i\theta'\nu_y}\Big), \\ t_\downarrow &= \tfrac{1}{2}e^{ik_z L}\big(\nu_0 + \nu_z e^{i\theta\nu_y}\big). \end{aligned} \tag{3.21}$$

These are each rank-one matrices, one eigenvalue equals 0 and the other equals 1 in absolute value. The unit transmission eigenvalue is N_Landau-fold degenerate in the transverse momentum $\boldsymbol{k}_\parallel$.

At the Fermi level $E = 0$ the particle-hole symmetry relation (3.17) implies $k'_z = -k_z$, $\theta' = \pi - \theta$, hence

$$t_\mathrm{NSN}(0) = \tfrac{1}{2}e^{-ik_z L\sigma_z}\big(\nu_0 - \nu_z\sigma_z e^{i\theta\nu_y}\big). \tag{3.22}$$

One verifies that

$$t_\mathrm{NSN}(0) = \nu_y\sigma_y t^*_\mathrm{NSN}(0)\nu_y\sigma_y, \tag{3.23}$$

as required by particle-hole symmetry.

3.4 Transport properties

The transmission matrix allows us to calculate the transport properties of the NSN junction, under the assumption that there is no backscattering of

the chiral modes in the Weyl superconductor. To simplify the notation, we write t for the Fermi-level transmission matrix $t_{\mathrm{NSN}}(0)$. The submatrices of electron and hole components are denoted by t_{ee}, t_{hh}, t_{he}, and t_{eh}. We define the combinations

$$\mathcal{T}_\pm = t_{ee}^\dagger t_{ee} \pm t_{he}^\dagger t_{he}, \tag{3.24a}$$

$$\mathcal{T}_+ = \tfrac{1}{2}(\nu_0 + \nu_z) t^\dagger t, \quad \mathcal{T}_- = \tfrac{1}{2}(\nu_0 + \nu_z) t^\dagger \nu_z t. \tag{3.24b}$$

3.4.1 Thermal conductance

As a check, we first recover the result of Ref. 57 for the quantization of the thermal conductance.

The thermal conductance $G_{\mathrm{thermal}} = J_{12}/\delta T$ gives the heat current J_{12} transported at temperature T_0 from contact N_1 to N_2 via the superconductor, in response to a small temperature difference δT between the contacts. It follows from the total transmitted quasiparticle current,

$$G_{\mathrm{thermal}} = \tfrac{1}{2} g_0 N_{\mathrm{Landau}} \operatorname{Tr} t^\dagger t = g_0 \frac{e\Phi}{h}, \tag{3.25}$$

with $N_{\mathrm{Landau}} = e\Phi/h$ the Landau level degeneracy and $g_0 = \frac{1}{3}(\pi k_{\mathrm{B}})^2 (T_0/h)$ the thermal conductance quantum. The factor $1/2$ in the first equation appears because the quasiparticles in the Weyl superconductor are Majorana fermions. It is cancelled by the factor of two from $\operatorname{Tr} t t^\dagger = 2$, in view of Eq. (3.22).

3.4.2 Electrical conductance

Referring to the electrical circuit of Fig. 3.1b, we consider the electrical conductance $G_{12} = dI_2/dV_1$, given by

$$\begin{aligned} G_{12} &= \frac{e^2}{h} N_{\mathrm{Landau}} \operatorname{Tr} \mathcal{T}_- \\ &= \frac{e^2}{h} N_{\mathrm{Landau}} \tfrac{1}{2} \operatorname{Tr} (\nu_0 + \nu_z) t^\dagger \nu_z t. \end{aligned} \tag{3.26}$$

In the linear response limit $V_1 \to 0$ we substitute t from Eq. (3.22), which gives

$$G_{12}(0) = \cos^2\theta \frac{e^2}{h} N_{\mathrm{Landau}} = \frac{(e\kappa)^2}{h} \frac{e\Phi}{h}. \tag{3.27}$$

The conductance quantum e^2/h is renormalized by the effective charge $e \mapsto e\kappa$. At $\mu = 0$, when $k_z = K$, the renormalization factor is $\kappa_0^2 =$

$(Q_{\text{eff}}/e)^2 = 1 - \Delta_0^2/\beta^2$ from Eq. (3.14). Note that the conductance per $h/2e$ vortex is $\frac{1}{2}(e\kappa_0)^2/h$, with an additional factor $1/2$ to signal the Majorana nature of the quasiparticles.

At finite $E = eV_1$ we must use the energy-dependent transmission matrix (3.20), which gives

$$G_{12}(E) = \tfrac{1}{2}\frac{e^2}{h} N_{\text{Landau}}\big(\cos\theta + \cos\theta' + \cos^2\theta + \cos^2\theta'\big). \tag{3.28}$$

Substituting Eq. (3.13) for $\cos\theta$ and $\cos\theta'$ at k_z and k_z', given as a function of E by Eq. (3.16), we find

$$G_{12}(E) = G_{12}(0)\left(1 - \frac{\Delta_0^2 E}{(\beta^2 - \Delta_0^2)^{3/2}} + \mathcal{O}(E^2)\right). \tag{3.29}$$

The energy dependence of the differential conductance comes entirely from the energy dependence of the effective charge: At $E = 0$ the electron-like and hole-like chiral Landau levels have precisely opposite effective charge $\pm Q_{\text{eff}}$, but for $E \neq 0$ the effective charges differ in absolute value by an amount $\propto dk_z/dE$.

3.4.3 Shot noise

At temperatures small compared to the applied voltage V_2, the time dependent fluctuations in the current I_2 are due to shot noise. The formula for the shot noise power is [61]

$$P_{12} = \frac{e^3 V_1}{h}\,\mathrm{Tr}\,(\mathcal{T}_+ - \mathcal{T}_-^2). \tag{3.30}$$

This can again be written in terms of the Pauli matrix τ_z and evaluated using Eq. (3.22),

$$P_{12} = \frac{e^3 V_1}{h}\big(1 - \tfrac{1}{2}\kappa^2 - \tfrac{1}{2}\kappa^4\big). \tag{3.31}$$

The shot noise vanishes when $\kappa \to 1$, it is fully due to the charge renormalization.

The Fano factor F, the dimensionless ratio of shot noise power and average current, results as

$$F = \frac{P_{12}}{eV_1 G_{12}} = \frac{1}{\kappa^2} - \tfrac{1}{2}(1 + \kappa^2). \tag{3.32}$$

3.4.4 Thermo-electricity

Because of the energy dependence of the effective charge, a temperature difference δT between contacts 1 and 2 will produce an electrical current $I_{12} = \alpha_{12}\delta T$ in addition to a heat current. The thermo-electric coefficient α_{12} is given by [62]

$$\alpha_{12} = \frac{\pi^2}{3e} k_{\mathrm{B}}^2 T_0 \lim_{E\to 0} \frac{d}{dE} G_{12}(E). \tag{3.33}$$

Substitution of Eq. (3.29) gives

$$\begin{aligned}
\alpha_{12} &= -\frac{\pi^2}{3e} k_{\mathrm{B}}^2 T_0 G_{12}(0) \frac{\Delta_0^2}{(\beta^2 - \Delta_0^2)^{3/2}} \\
&= -g_0 e \kappa_0^2 N_{\mathrm{Landau}} \frac{\Delta_0^2}{(\beta^2 - \Delta_0^2)^{3/2}} \\
&= -g_0 e N_{\mathrm{Landau}} \frac{(\Delta_0/\beta)^2}{(\beta^2 - \Delta_0^2)^{1/2}}.
\end{aligned} \tag{3.34}$$

3.5 Numerical simulations

To test these analytical results, we have carried out numerical calculations in a tight-binding model of the Weyl superconductor with a vortex lattice.

3.5.1 Tight-binding Hamiltonian

The Bogoliubov-de Gennes Hamiltonian H_{S} in the superconducting region $0 < z < L$ is

$$H_{\mathrm{S}} = \begin{pmatrix} H_0(\boldsymbol{k} + e\boldsymbol{A}) & \Delta \\ \Delta^* & -\sigma_y H_0^*(-\boldsymbol{k} + e\boldsymbol{A})\sigma_y \end{pmatrix}, \tag{3.35a}$$

$$\begin{aligned}
H_0(\boldsymbol{k}) = t_0 \sum_{\alpha=x,y,z} &[\tau_z \sigma_\alpha \sin k_\alpha a_0 + \tau_x \sigma_0 (1 - \cos k_\alpha a_0)] \\
&+ \beta \tau_0 \sigma_z - \mu \tau_0 \sigma_0.
\end{aligned} \tag{3.35b}$$

The cubic lattice constant of the tight-binding model is a_0 and t_0 is the nearest-neigbor hopping energy. In what follows we will set a_0 and t_0 both equal to unity.

In the strong-type-II limit the magnetic field $\boldsymbol{B} = B_0\hat{z}$ penetrates the superconductor uniformly, with vector potential $\boldsymbol{A} = (-B_0 y, 0, 0)$. The absolute value Δ_0 of the pair potential $\Delta = \Delta_0 e^{i\phi}$ can also be taken

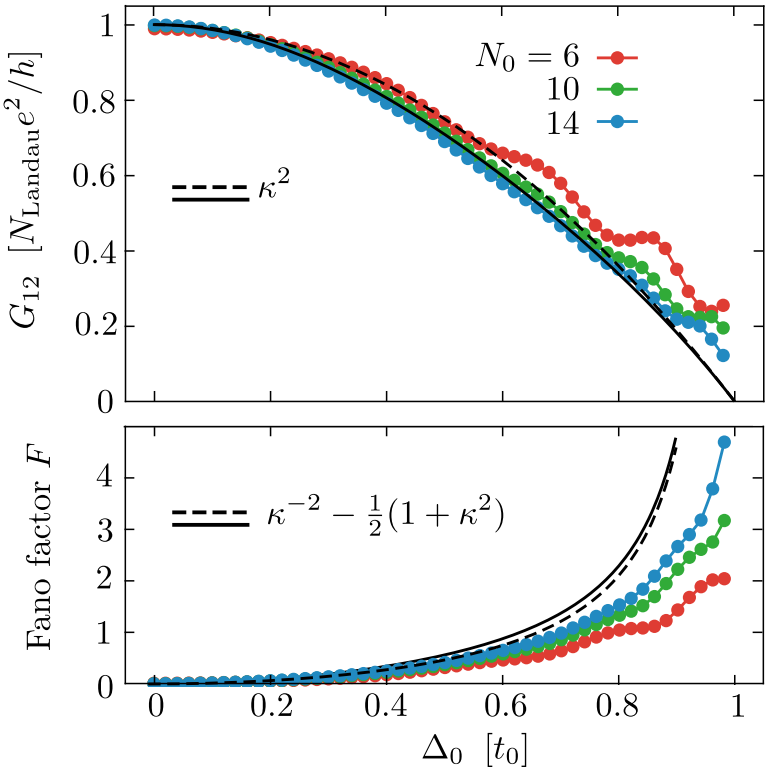

Figure 3.4: Data points: Electrical conductance (top panel) and Fano factor (bottom panel) in the superconducting vortex lattice (lattice constant d_0), as a function of the pair potential Δ_0 at fixed magnetization $\beta = 1$, calculated from the tight-binding model (lattice constant a_0) for different lattice constant ratios $N_0 = d_0/a_0$. The black curves are the analytical predictions from the charge renormalization factor κ, both in the approximation of a linearized dispersion (black dashed curve, $\kappa = \kappa_0 = \sqrt{1 - \Delta_0^2/\beta^2}$) and for the full nonlinear dispersion (black solid).

uniform, assuming that the size $\xi_0 = \hbar v_{\mathrm{F}}/\Delta_0$ of the vortex core is small compared to the magnetic length $l_m = \sqrt{\hbar/eB_0}$. For the analytical calculations this is the only requirement. For the numerics we also take ξ_0 small compared to the tight-binding discretization length a_0, and then ensure that a vortex core (where the phase field is undefined) does not coincide with a lattice point. This implies that a_0 is large compared to

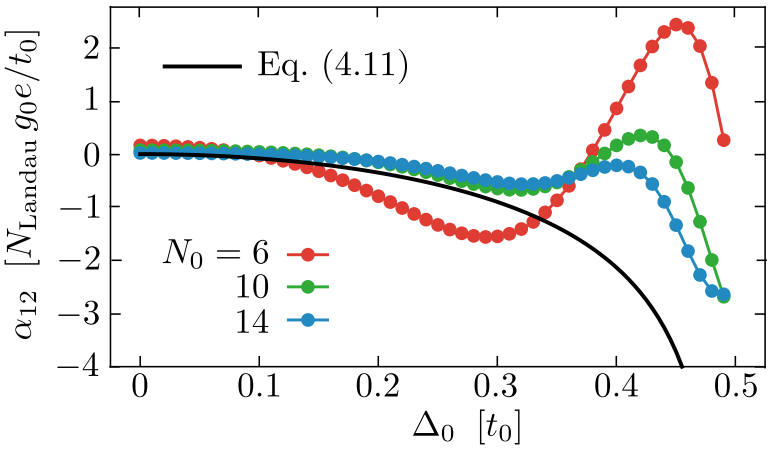

Figure 3.5: Dependence on Δ_0 for $\beta = 0.5$ of the thermo-electric coefficient (3.33), calculated from the infinite-system analytics (black solid curve) or obtained from finite-size numerics (colored data points).

the atomic lattice constant (which itself must be much smaller than ξ_0).

The vortices are arranged on a square lattice in the x–y plane, lattice constant $d_0 = N_0 a_0$, with two $h/2e$ vortices in a unit cell. The number

$$N_0 = (a_0^2 e B_0/h)^{-1/2} \tag{3.36}$$

is set at an integer value. The phase $\phi(\boldsymbol{r})$ winds around the vortex cores $\boldsymbol{R}_n$ according to

$$\nabla \times \nabla\phi = 2\pi\hat{z}\textstyle\sum_n \delta(\boldsymbol{r} - \boldsymbol{R}_n). \tag{3.37}$$

In the normal metal leads $z < 0$, $z > L$ we have $\Delta_0 \equiv 0$ and a large chemical potential μ_{N}, so only modes with a large longitudinal momentum k_z couple to the superconductor. We effectuate the $\mu_{\text{N}} \to \infty$ limit by removing the transverse x, y couplings in the leads, resulting in the Hamiltonian[1]

$$H_{\text{N}} = \nu_z \tau_z \sigma_z \sin k_z + \nu_z \tau_x \sigma_0 (1 - \cos k_z). \tag{3.38}$$

The gauge-invariant discretization of the Hamiltonian (3.35) in the magnetic Brillouin zone is detailed in Ref. 57. The scattering matrix is calculated using the Kwant code [52].

[1] We have checked that the continuum limit of the tight-binding Hamiltonian of Sec. 3.5.1 gives the same analytical results for the transport coefficients as calculated in Sec. 3.4, see Appendix A.

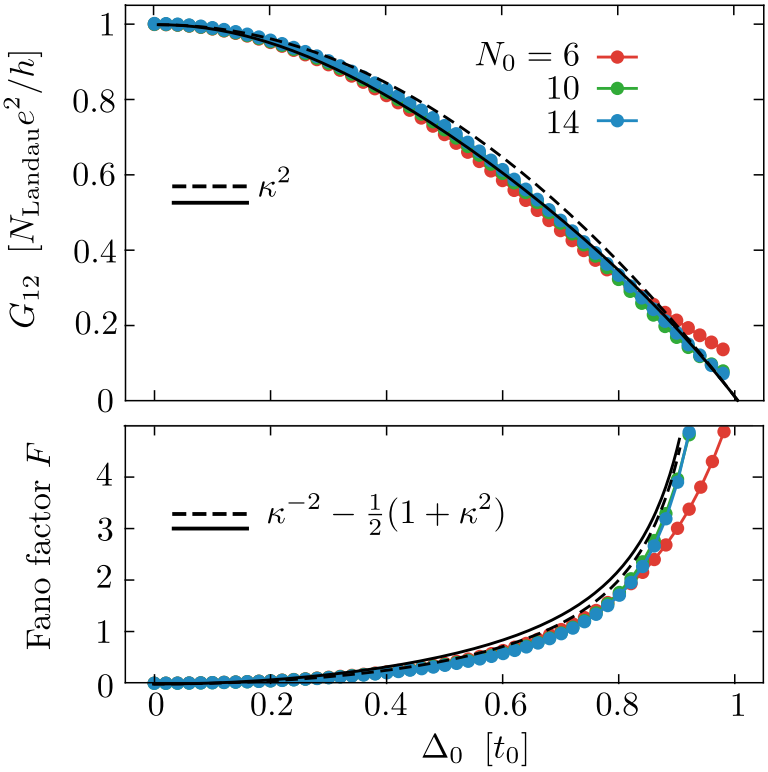

Figure 3.6: Same as Fig. 3.4, but for a magnetization β that is perpendicular rather than parallel to the magnetic field B.

3.5.2 Results

Results for the conductance and shot noise are shown in Fig. 3.4, as a function of Δ_0 for $\beta = 1$, $\mu = 0$. The analytical predictions (3.27) for the conductance and (3.32) for the Fano factor are given by the black curves. As a check, for these curves we have also calculated the charge renormalization factor κ from the full sinusoidal dispersion, without making the small-$\boldsymbol{k}$ expansion of Eq. (3.1) — the difference with $\kappa_0 = \sqrt{1 - \Delta_0^2/\beta^2}$ is small.

To assess finite-size effects in the numerics we show results for different values of the ratio $N_0 = d_0/a_0$ of magnetic unit cell and tight-binding unit cell. As expected, the agreement between numerics and analytics

improves with increasing N_0, for Δ_0/β not close to unity. (At $\Delta_0 = \beta$ the spectrum becomes gapless and the low-energy analytics breaks down.)

These are results at the Fermi level, $E = 0$. The energy dependence of the conductance determines the thermo-electric coefficient (3.33). We show numerical results for $\alpha_{12} \propto dG_{12}/dE$ in Fig. 3.5, for a smaller $\beta = 0.5$ to reduce the oscillations that disappear only slowly with increasing N_0.

3.5.3 Test for isotropy of the charge renormalization

So far we assumed that the internal magnetization β is parallel to the external magnetic field in the z-direction. This assumption is needed for our low-energy analytics, but numerically we can take an arbitrary angle between the magnetization $\boldsymbol{\beta} = (\beta_x, \beta_y, \beta_z)$ and the magnetic field, by replacing the term $\beta\tau_0\sigma_z$ in the Hamiltonian (3.35b) with $\tau_0 \boldsymbol{\beta} \cdot \boldsymbol{\sigma}$. Results for $\boldsymbol{\beta} = (\beta, 0, 0)$, so for a magnetization perpendicular to the magnetic field, are shown in Fig. 3.6. There is no qualitative difference with Fig. 3.4 for the parallel configuration, the quantitative difference is that the finite-size effects are smaller.

3.6 Conclusion

In summary, we have shown how the charge renormalization $e \mapsto \kappa e$ of Weyl fermions in a superconducting vortex lattice modifies the electrical and thermo-electrical transport properties.

In the electrical conductance, the current per vortex is reduced by a factor $\frac{1}{2}\kappa^2$ — a prefactor $1/2$ because of the Majorana nature of the quasiparticles and a factor κ^2 because of the effective charge. At the Weyl point $\kappa \to \kappa_0 = \sqrt{1 - \Delta_0^2/\beta^2}$ depends on the ratio of the superconducting gap Δ_0 and the separation 2β of the Weyl points of opposite chirality.

The charge-squared renormalization of the electrical conductance is a simple result, but perhaps not what one might have guessed by analogy with the fractional quantum Hall effect, where a $1/3$ fractional charge reduces the conductance by $1/3$ rather than $1/9$. The key difference is that here the quasiparticles are not in an eigenstate of charge; the charge renormalization is due to quantum fluctuations, which give uncorrelated reductions by $\kappa \times \kappa$ at entrance and exit. These quantum fluctuations of the charge are also responsible for the large shot noise power that we have found, with a diverging Fano factor (3.32) in the limit $\kappa \to 0$.

The energy dependence of the charge renormalization implies that charge transport parallel to the magnetic field B goes hand-in-hand with heat

transport. As a result, a nonzero thermo-electric coefficient α_{12} along the field lines appears in a chiral Landau level — something that would not be possible in the normal state: The Landau level contributes an energy-independent number of propagating modes along B (one mode per flux quantum) and the chirality suppresses backscattering, so the energy derivative in Eq. (3.33) would vanish in the normal state.

There is much recent interest in thermo-electricity of Weyl fermions in a Landau level [63–66], but that refers to currents perpendicular to B. Our findings show that charge renormalization in a Weyl superconductor provides a mechanism for a nonzero effect parallel to the field lines.

In our calculations we have assumed a clean system, without impurity scattering. However, we expect the transport properties to be robust against non-magnetic disorder, which in the effective low-energy Hamiltonian (3.5) would enter as a term proportional to σ_z that does not couple Landau levels of opposite chirality.

Appendix

3.A Calculation of transport properties from the continuum limit of the tight-binding model

In the tight-binding model of Sec. 3.5.1 the wave matching at the normal-superconductor (NS) interface is implemented by a nearest-neighbor coupling on a square lattice of the Hamiltonians (3.35) in S to (3.38) in N. Microscopically this results in different matching conditions on the wave function than the matching conditions (3.12) from the analytical treatment of Sec. 3.3. In this Appendix we check that the continuum limit of the tight-binding model still gives the same results for the transport properties as obtained in Sec. 3.4 from the main text. For simplicity, we set $\mu = 0$ and restrict our considerations to $E = 0$.

3.A.1 Matching condition

The linearized Hamiltonian for the normal metal reads

$$H_{\mathrm{N}} = \nu_z \tau_z \sigma_z k_z \tag{3.39}$$

and for the superconductor it reads

$$H_{\mathrm{S}} = \begin{pmatrix} \tau_z \boldsymbol{\sigma} \cdot (\boldsymbol{k} - e\boldsymbol{A}) + \beta\sigma_z & \Delta_0 e^{i\phi} \\ \Delta_0 e^{-i\phi} & -\tau_z \boldsymbol{\sigma} \cdot (\boldsymbol{k} + e\boldsymbol{A}) + \beta\sigma_z \end{pmatrix}. \tag{3.40}$$

The particle current operator is the same for both the normal metal and the superconductor,

$$J_p = \nu_z \tau_z \sigma_z \,, \tag{3.41}$$

therefore, at the NS interfaces the matching condition

$$\Psi(z = 0_-) = \Psi(z = 0_+) \,, \qquad \Psi(z = L + 0_-) = \Psi(z = L + 0_+), \tag{3.42}$$

will respect the particle current conservation. This matching condition corresponds to the continuum limit of the tight-binding model of the interface.

As done in Sec. 3.3.1, we start by examining a single NS interface at $z = L$, with a superconductor at $z < L$ and a normal metal at $z > L$. In contrast to the situation described in the main text, the incident modes in the superconductor from Eq. (3.10),

$$\begin{aligned} \Psi_{\mathrm{S}} &\propto \cos(\theta/2)|{+}{+}{-}\rangle_{\nu\tau\sigma} + \sin(\theta/2)|{-}{+}{-}\rangle_{\nu\tau\sigma}, \\ \Psi'_{\mathrm{S}} &\propto \cos(\theta'/2)|{+}{+}{+}\rangle_{\nu\tau\sigma} - \sin(\theta'/2)|{-}{+}{+}\rangle_{\nu\tau\sigma}. \end{aligned} \tag{3.43}$$

can no longer be continuously matched to an outgoing state in the normal lead

$$\Psi_{\mathrm{N}} \in \mathrm{span}(|{+}{+}{+}\rangle_{\nu\tau\sigma}, |{-}{+}{-}\rangle_{\nu\tau\sigma}, |{-}{-}{+}\rangle_{\nu\tau\sigma}, |{+}{-}{-}\rangle_{\nu\tau\sigma})\,. \tag{3.44}$$

To satisfy the matching condition (3.42), an evanescent wave is excited in the superconductor. (There are no evanescent modes in the normal metal.) Because all the incident modes reside in the $\tau = +1$ sector and different τ sectors are decoupled, in what follows we will focus on $\tau = +1$ sector, and omit the τ component of the spinor.

3.A.2 Evanescent modes

The evanescent modes are the eigenstates of the effective low energy Hamiltonian (3.5a) with $\mathrm{Im}(k_z) < 0$. In this section we will show how to construct them.

We first investigate the spectrum of H_+ for k_z in the vicinity of $-K$: $k_z = -K + \delta k_z$, $M(-K + \delta k_z) = \kappa(-K)\delta k_z + \mathcal{O}(\delta k_z^2)$, $\kappa(-K) \equiv \kappa > 0$, $\theta' = \theta(-K)$:

$$H_+ = \begin{pmatrix} \kappa\delta k_z & D \\ D^\dagger & -\kappa\delta k_z \end{pmatrix}, \qquad D = -i\partial_x - \partial_y + e\mathcal{A}_{+,x} - ie\mathcal{A}_{+,y}. \tag{3.45}$$

The states at zero energy satisfy

$$H_+\psi = 0\,. \tag{3.46}$$

Acting with H_+ from the left on both sides of the equation yields

$$H_+^2\psi = 0\,, \quad H_+^2 = \begin{pmatrix} (\kappa\delta k_z)^2 + DD^\dagger & 0 \\ 0 & (\kappa\delta k_z)^2 + D^\dagger D \end{pmatrix}, \tag{3.47}$$

therefore the two components of the state $\psi = (\psi_1, \psi_2)^T$ must be be eigenstates of $DD^\dagger$ and $D^\dagger D$ respectively, with the same eigenvalue. Suppose we can find the eigenstates of $D^\dagger D$:

$$D^\dagger D\phi_n = \epsilon_n\phi_n\,, \quad \epsilon_n > 0\,, \quad n = 1, 2\ldots \tag{3.48}$$

Note that $\epsilon_n = 0$ is not allowed as shown in Ref. 57, and $\epsilon_n \geq 0$ because they are the eigenvalues of a square of a Hermitian operator. The operator $DD^\dagger$ has one zero-mode: ψ_0, $D^\dagger\psi_0 = 0$. The remainder of the spectrum of $DD^\dagger$ can be obtained by acting with operator D on wavefunctions ϕ_n,

$$DD^\dagger(D\phi_n) = \epsilon_n D\phi_n \,. \tag{3.49}$$

This means that the sought wavefunction can be written as

$$\psi = \begin{pmatrix} \alpha D\phi_n \\ \beta\phi_n \end{pmatrix} \quad \text{or} \quad \psi = \begin{pmatrix} \psi_0 \\ 0 \end{pmatrix}. \tag{3.50}$$

The second possibility corresponds to the propagating zeroth Landau level. Therefore, we will now focus on the first possibility. Substituting the wavefunction of this form into eigenvalue equation (3.46) yields

$$\begin{pmatrix} \kappa\delta k_z & D \\ D^\dagger & -\kappa\delta k_z \end{pmatrix}\begin{pmatrix} \alpha D\phi_n \\ \beta\phi_n \end{pmatrix} = 0\,, \tag{3.51}$$

which gives us

$$\kappa\delta k_z = \pm i\sqrt{\epsilon_n}\,, \qquad \beta = \mp i\alpha\sqrt{\epsilon_n}. \tag{3.52}$$

We choose the lower sign in the solution in order to satisfy the condition $\mathrm{Im}(k_z) < 0$. With this we can obtain the evanescent modes of the full Hamiltonian $\mathcal{H}$,

$$\begin{aligned} \Psi &= e^{(-iK+\sqrt{\epsilon_n})z} e^{\frac{1}{2}i\theta'\nu_y\sigma_z}|+\rangle_\nu \begin{pmatrix} D\phi_n \\ i\sqrt{\epsilon_n}\phi_n \end{pmatrix}_\sigma \\ &= \begin{pmatrix} D\phi_n \cos\frac{\theta'}{2} \\ i\sqrt{\epsilon_n}\phi_n \cos\frac{\theta'}{2} \\ -D\phi_n \sin\frac{\theta'}{2} \\ i\sqrt{\epsilon_n}\phi_n \sin\frac{\theta'}{2} \end{pmatrix} e^{(-iK+\sqrt{\epsilon_n})z}\,, \end{aligned} \tag{3.53a}$$

where the spinor on the right hand side is written in the basis $|{+}{+}\rangle_{\nu\sigma}$, $|{+}{-}\rangle_{\nu\sigma}$, $|{-}{+}\rangle_{\nu\sigma}$, $|{-}{-}\rangle_{\nu\sigma}$. The evanescent modes corresponding to k_z around $+K$ can be obtained by acting with charge conjugation operator on Ψ,

$$\Psi' = \nu_y\sigma_y\mathcal{K}\Psi = \begin{pmatrix} i\sqrt{\epsilon_n}\phi_n^* \sin\frac{\theta'}{2} \\ -D^*\phi_n^* \sin\frac{\theta'}{2} \\ -i\sqrt{\epsilon_n}\phi_n^* \cos\frac{\theta'}{2} \\ -D^*\phi_n^* \cos\frac{\theta'}{2} \end{pmatrix} e^{(iK+\sqrt{\epsilon_n})z}\,. \tag{3.53b}$$

We can also obtain the two chiral Landau levels

$$\Psi'_S = e^{-iKz} e^{\frac{1}{2} i\theta' \nu_y \sigma_z} |+\rangle_\nu \begin{pmatrix} \psi_0 \\ 0 \end{pmatrix} = \begin{pmatrix} \psi_0 \cos\frac{\theta'}{2} \\ 0 \\ -\psi_0 \sin\frac{\theta'}{2} \\ 0 \end{pmatrix} e^{-iKz}, \tag{3.54a}$$

$$\Psi_S = \nu_y \sigma_y \mathcal{K} \Psi_S = \begin{pmatrix} 0 \\ \psi_0 \sin\frac{\theta'}{2} \\ 0 \\ \psi_0 \cos\frac{\theta'}{2} \end{pmatrix} e^{iKz}, \tag{3.54b}$$

which correspond to states in Eq. (3.43). From now on we will drop the prime at θ' and define $\theta = \theta(-K)$.

3.A.3 Transmitted wave

We will now consider an incoming wave which is Ψ'_{S} – the chiral Landau level at zero energy with momentum $k_z = -K$, cf. Eq. (3.54a). The solution for Ψ_{S} can be obtained using particle-hole symmetry. We want to find a superposition of evanescent modes Eq. (3.53) such that its profile at the interface $z = L$,

$$\Psi_{\mathrm{eva}} = \sum_n \alpha_n \begin{pmatrix} D\phi_n \cos\frac{\theta}{2} \\ i\sqrt{\epsilon_n}\phi_n \cos\frac{\theta}{2} \\ -D\phi_n \sin\frac{\theta}{2} \\ i\sqrt{\epsilon_n}\phi_n \sin\frac{\theta}{2} \end{pmatrix} + \alpha'_n \begin{pmatrix} i\sqrt{\epsilon_n}\phi_n^* \sin\frac{\theta}{2} \\ -D^*\phi_n^* \sin\frac{\theta}{2} \\ -i\sqrt{\epsilon_n}\phi_n^* \cos\frac{\theta}{2} \\ -D^*\phi_n^* \cos\frac{\theta}{2} \end{pmatrix}, \tag{3.55}$$

will satisfy the boundary condition

$$\Psi'_{\mathrm{S}} + \Psi_{\mathrm{eva}} = \Psi'_{\mathrm{N}}. \tag{3.56}$$

Writing it down explicitly we get

$$\begin{pmatrix} \psi_0 \cos\frac{\theta}{2} \\ 0 \\ -\psi_0 \sin\frac{\theta}{2} \\ 0 \end{pmatrix} + \sum_n \alpha_n \begin{pmatrix} D\phi_n \cos\frac{\theta}{2} \\ i\sqrt{\epsilon_n}\phi_n \cos\frac{\theta}{2} \\ -D\phi_n \sin\frac{\theta}{2} \\ i\sqrt{\epsilon_n}\phi_n \sin\frac{\theta}{2} \end{pmatrix} + \alpha'_n \begin{pmatrix} i\sqrt{\epsilon_n}\phi_n^* \sin\frac{\theta}{2} \\ -D^*\phi_n^* \sin\frac{\theta}{2} \\ -i\sqrt{\epsilon_n}\phi_n^* \cos\frac{\theta}{2} \\ -D^*\phi_n^* \cos\frac{\theta}{2} \end{pmatrix} = \begin{pmatrix} g_1 \\ 0 \\ 0 \\ g_2 \end{pmatrix}, \tag{3.57}$$

where g_1, g_2 are some functions of $\boldsymbol{r} = (x, y)$. If we project both sided of the equation on the second and third component of the spinor, we obtain

$$\begin{aligned} 0 &= \sum_n \alpha_n i\sqrt{\epsilon_n}\phi_n \cos\tfrac{\theta}{2} - \alpha'_n D^*\phi_n^* \sin\tfrac{\theta}{2}, \\ \psi_0 \sin\tfrac{\theta}{2} &= \sum_n -\alpha_n D\phi_n \sin\tfrac{\theta}{2} - \alpha'_n i\sqrt{\epsilon_n}\phi_n^* \cos\tfrac{\theta}{2}\,, \end{aligned} \tag{3.58}$$

or equivalently

$$\begin{aligned}\sum_n \alpha_n i\sqrt{\epsilon_n}\phi_n &= \sum_n \alpha'_n D^*\phi_n^* \sin\tfrac{\theta}{2}/\cos\tfrac{\theta}{2},\\ \sum_n \alpha_n D\phi_n &= \sum_n -\alpha'_n i\sqrt{\epsilon_n}\phi_n^* \cos\tfrac{\theta}{2}/\sin\tfrac{\theta}{2} - \psi_0\,.\end{aligned} \tag{3.59}$$

Substituting this back into Eq. (3.57) and projecting it on the first and fourth component we get

$$\begin{aligned}\begin{pmatrix} g_1 \\ g_2 \end{pmatrix} &= \sum_n \alpha_n \begin{pmatrix} D\phi_n \cos\frac{\theta}{2} \\ i\sqrt{\epsilon_n}\phi_n \sin\frac{\theta}{2} \end{pmatrix} + \alpha'_n \begin{pmatrix} i\sqrt{\epsilon_n}\phi_n^* \sin\frac{\theta}{2} \\ -D^*\phi_n^* \cos\frac{\theta}{2} \end{pmatrix} + \begin{pmatrix} \psi_0 \cos\frac{\theta}{2} \\ 0 \end{pmatrix}\\ &= \sum_n \alpha'_n \begin{pmatrix} -i\sqrt{\epsilon_n}\phi_n^* \cos^2\frac{\theta}{2}/\sin\frac{\theta}{2} \\ D^*\phi_n^* \sin^2\frac{\theta}{2}/\cos\frac{\theta}{2} \end{pmatrix} + \alpha'_n \begin{pmatrix} i\sqrt{\epsilon_n}\phi_n^* \sin\frac{\theta}{2} \\ -D^*\phi_n^* \cos\frac{\theta}{2} \end{pmatrix}\\ &\quad + \begin{pmatrix} -\psi_0 \cos\frac{\theta}{2} \\ 0 \end{pmatrix} + \begin{pmatrix} \psi_0 \cos\frac{\theta}{2} \\ 0 \end{pmatrix}\\ &= \sum_n \alpha'_n \begin{pmatrix} i\sqrt{\epsilon_n}\phi_n^* (\sin\frac{\theta}{2} - \cos^2\frac{\theta}{2}/\sin\frac{\theta}{2}) \\ -D^*\phi_n^* (\cos\frac{\theta}{2} - \sin^2\frac{\theta}{2}/\cos\frac{\theta}{2}) \end{pmatrix}\\ &= \sum_n \alpha'_n \begin{pmatrix} -i\sqrt{\epsilon_n}\phi_n^* \kappa/\sin\frac{\theta}{2} \\ -D^*\phi_n^* \kappa/\cos\frac{\theta}{2} \end{pmatrix},\end{aligned} \tag{3.60}$$

therefore, the transmitted wave has the form

$$\Psi'_N = \sum_n \alpha'_n \begin{pmatrix} -i\sqrt{\epsilon_n}\phi_n^* \kappa/\sin\frac{\theta}{2} \\ 0 \\ 0 \\ -D^*\phi_n^* \kappa/\cos\frac{\theta}{2} \end{pmatrix}. \tag{3.61}$$

3.A.4 Charge transfer

Since there is no reflection, we normalize the outgoing wave such that the outgoing particle current is 1:

$$\begin{aligned}
\langle\Psi_{\mathrm{N}}|J_p|\Psi_{\mathrm{N}}\rangle &= \sum_{nm}\alpha_n'^{*}\begin{pmatrix}-i\sqrt{\epsilon_n}\phi_n^*\kappa/\sin\frac{\theta}{2}\\0\\0\\-D^*\phi_n^*\kappa/\cos\frac{\theta}{2}\end{pmatrix}^{\dagger}\alpha_m'\begin{pmatrix}-i\sqrt{\epsilon_m}\phi_m^*\kappa/\sin\frac{\theta}{2}\\0\\0\\-D^*\phi_m^*\kappa/\cos\frac{\theta}{2}\end{pmatrix}\\
&= \sum_{nm}\alpha_n'^{*}\alpha_m'[\sqrt{\epsilon_n}\sqrt{\epsilon_m}(\phi_n^*)^{\dagger}\phi_m^*\kappa/\sin\tfrac{\theta}{2}\kappa/\sin\tfrac{\theta}{2}\\
&\quad+(\phi_n^*)^{\dagger}(D^*)^{\dagger}D^*\phi_m^*\kappa/\cos\tfrac{\theta}{2}\kappa/\cos\tfrac{\theta}{2}]\\
&= \sum_n|\alpha_n'|^2\epsilon_n[\kappa^2/\sin^2\tfrac{\theta}{2}+\kappa^2/\cos^2\tfrac{\theta}{2}]\\
&= (\kappa^2/\sin^2\tfrac{\theta}{2}+\kappa^2/\cos^2\tfrac{\theta}{2})\sum_n|\alpha_n'|^2\epsilon_n\overset{!}{=}1\,.
\end{aligned}\tag{3.62}$$

Albeit coefficients α_n' cannot be determined in a closed form, the information we obtained in Eqs. (3.61) and (3.62) is sufficient to calculate the transport properties. In particular, the transmitted electric charge is given by

$$\begin{aligned}
\langle\Psi_{\mathrm{N}}'|e\nu_z|\Psi_{\mathrm{N}}'\rangle &= e\sum_n|\alpha_n'|^2\epsilon_n[\kappa^2/\sin^2\tfrac{\theta}{2}-\kappa^2/\cos^2\tfrac{\theta}{2}]\\
&= e\frac{\kappa^2/\sin^2\frac{\theta}{2}-\kappa^2/\cos^2\frac{\theta}{2}}{\kappa^2/\sin^2\frac{\theta}{2}+\kappa^2/\cos^2\frac{\theta}{2}}\\
&= e\frac{1/\sin^2\frac{\theta}{2}-1/\cos^2\frac{\theta}{2}}{1/\sin^2\frac{\theta}{2}+1/\cos^2\frac{\theta}{2}}=\cos^2\theta/2-\sin^2\theta/2=e\kappa=Q_{\mathrm{eff}}\,,
\end{aligned}\tag{3.63}$$

which is the same result as Q_{N}' obtained in the main text in Eq. (3.14). The transmitted wave for the incident mode Ψ_{S} is $\Psi_{\mathrm{N}}=\nu_y\sigma_y\mathcal{K}\Psi_{\mathrm{N}}'$ (as required by the particle hole symmetry). Therefore, the corresponding transmitted charge is $\langle\Psi_{\mathrm{N}}|e\nu_z|\Psi_{\mathrm{N}}\rangle=-\kappa e=-Q_{\mathrm{eff}}$.

3.A.5 Transport properties

An analogous analysis can be performed for the interface at $z=0$, yielding the corresponding incident waves in the $z<0$ metallic lead: Φ_{N} and Φ_{N}',

which couple perfectly to the chiral Landau levels $\Psi_{\rm S}$, $\Psi'_{\rm S}$ respectively. This yields a transmission matrix

$$t = e^{iKL}|\Psi_{\rm N}\rangle\langle\Phi_{\rm N}| + e^{-iKL}|\Psi'_{\rm N}\rangle\langle\Phi'_{\rm N}|\,, \tag{3.64}$$

like in Eq. (3.18), with the difference that the modes in the superconductor can no longer be written explicitly in a closed form. Still we can compute the thermal conductance

$$G_{\rm thermal} = \frac{1}{2} g_0 N_{\rm Landau}\,{\rm Tr}\, t^\dagger t = g_0 \frac{e\Phi}{h}\,, \tag{3.65}$$

where we used that $\langle\Psi_N|\Psi'_N\rangle = 0$, as required by the unitarity of the scattering matrix. We can also compute the electric conductance

$$\begin{aligned} G_{12} &= \frac{e^2}{h} N_{\rm Landau}\,{\rm Tr}\,\frac{\nu_z+1}{2} t \nu_z t^\dagger \\ &= \frac{e^2}{h} N_{\rm Landau}\Big(\langle\Psi_{\rm N}|\nu_z|\Psi_{\rm N}\rangle\langle\Phi_{\rm N}|\frac{\nu_z+1}{2}|\Phi_{\rm N}\rangle \\ &\quad + \langle\Psi'_{\rm N}|\nu_z|\Psi'_{\rm N}\rangle\langle\Phi'_{\rm N}|\frac{\nu_z+1}{2}|\Phi'_{\rm N}\rangle\Big) \\ &= \frac{e^2}{h} N_{\rm Landau}\frac{1}{2}\Big[\kappa(1+\kappa) - \kappa(1-\kappa)\Big] = \frac{(e\kappa)^2}{h}\frac{e\Phi}{h}\,, \end{aligned} \tag{3.66}$$

Where we used the fact that

$$\begin{aligned} \langle\Psi_{\rm N}|\nu_z|\Psi'_{\rm N}\rangle &= \int d\boldsymbol{r} \begin{pmatrix} g_2^*(\boldsymbol{r}) \\ 0 \\ 0 \\ g_1^*(\boldsymbol{r}) \end{pmatrix}^\dagger \nu_z \begin{pmatrix} g_1(\boldsymbol{r}) \\ 0 \\ 0 \\ g_2(\boldsymbol{r}) \end{pmatrix} \\ &= \int d\boldsymbol{r}[g_2(\boldsymbol{r})g_1(\boldsymbol{r}) - g_1(\boldsymbol{r})g_2(\boldsymbol{r})] = 0\,, \end{aligned} \tag{3.67}$$

and similarly $\langle\Phi_{\rm N}|\nu_z|\Phi'_{\rm N}\rangle = 0$

The thermal and electric conductance obtained in Eqs. (3.65) and (3.66) are identical to the results obtained in the main text: Eqs. (3.25) and (3.27). Furthermore, a similar calculation shows that the shot noise power is also given by the same formula as in the main text: Eq. (3.31). This confirms that the tight-binding model is equivalent in the continuum limit to the analytics.

4 Universal chiral magnetic effect in the vortex lattice of a Weyl superconductor

4.1 Introduction

This chapter combines two topics of recent research on Weyl fermions in condensed matter. The first topic is the search for the chiral magnetic effect in equilibrium [47, 67–76]. The second topic is the search for Landau levels in a superconducting vortex lattice [34–36, 57]. What we will show is that the lowest Landau level in the Abrikosov vortex lattice of a Weyl superconductor supports the equilibrium chiral magnetic effect at the universal limit of $(e/h)^2$, unaffected by any renormalization of the quasiparticle charge by the superconducting order parameter. Let us introduce these two topics separately and show how they come together.

The first topic, the chiral magnetic effect (CME) in a Weyl semimetal, is the appearance of an electrical current I along lines of magnetic flux Φ, in response to a chemical potential difference $\mu_+ - \mu_-$ between Weyl fermions of opposite chirality. The universal value [55, 77, 78]

$$\frac{dI}{d\Phi} = \frac{e^2}{h^2}(\mu_+ - \mu_-) \tag{4.1}$$

follows directly from the product of the degeneracy $(e/h)\Phi$ of the lowest Landau level and the current per mode of $(e/h)(\mu_+ - \mu_-)$. A Weyl semimetal in equilibrium must have $\mu_+ = \mu_-$, hence a vanishing chiral magnetic effect — in accord with a classic result of Levitov, Nazarov, and Eliashberg [79, 80] that the combination of Onsager symmetry and gauge invariance forbids a linear relation between electrical current and magnetic field in equilibrium.

Because superconductivity breaks gauge invariance, a Weyl superconductor is not so constrained: As demonstrated in Ref. 47, one of the two chiralities can be gapped out by the superconducting order parameter. When a magnetic flux Φ penetrates uniformly through a thin film (no

vortices), an equilibrium current

$$\frac{dI}{d\Phi} = \pm \frac{ee^*}{h^2}\mu_\pm \tag{4.2}$$

appears along the flux lines, of a magnitude set by the equilibrium chemical potential $\mu_\pm$ of the ungapped chirality. The renormalized charge $e^* < e$ determines the degeneracy $(e^*/h)\Phi$ of the lowest Landau level in the superconducting thin film.

The second topic, the search for Landau levels in an Abrikosov vortex lattice, goes back to the discovery of massless Dirac fermions in d-wave superconductors [29, 30]. In that context scattering by the vortex lattice obscures the Landau level quantization [1, 3, 33], however, as discovered recently [57], the chirality of Weyl fermions protects the zeroth Landau level by means of a topological index theorem. The same index theorem enforces the $(e/h)\Phi$ degeneracy of the Landau level, even though the charge of the quasiparticles is renormalized to $e^* < e$. Does this topological protection extend to the equilibrium chiral magnetic effect, so that we can realize Eq. (4.2) with e^* replaced by e? That is the question we set out to answer in this work.

The outline of the chapter is as follows. In the next section we formulate the problem of a Weyl superconductor in a vortex lattice. We then show in Sec. 4.3 that a flux bias of the superconductor can drive the quasiparticles into a topologically distinct phase where one chirality is exponentially confined to the vortex cores. The unconfined Landau bands contain electron-like or hole-like Weyl fermions, while the vortex-core bands are charge-neutral Majorana fermions. The consequences of this topological phase transition for the chiral magnetic effect are presented in Sec. 4.4. We support our analytical calculations with numerical simulations and conclude in Sec. 4.5.

4.2 Formulation of the problem

We consider a multilayer heterostructure, see Fig. 4.1, composed of layers in the x–y plane of a magnetically doped topological insulator (such as Bi_2Se_3), separated in the z-direction by a normal-insulator spacer layer.

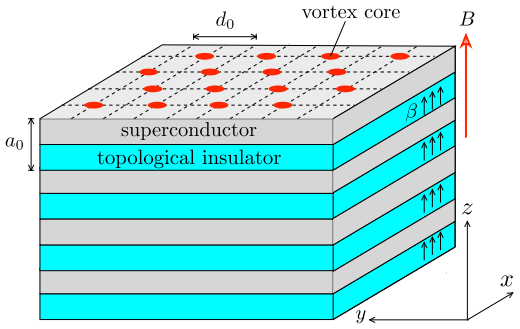

Figure 4.1: Cross-section through a heterostructure of alternating topological insulator layers and superconducting spacer layers. A perpendicular magnetization β separates a pair of Weyl cones of opposite chirality along k_z. Each Weyl cone is twofold degenerate in the electron-hole degree of freedom, mixed by the superconducting pair potential Δ_0. The mixing leaves the Weyl cones gapless, as long as the pair potential Δ_0 remains smaller than β.

The tight-binding Hamiltonian is [81]

$$H_0(\boldsymbol{k}) = \sum_{i=x,y,z} \tau_z \sigma_i \, t_i \sin k_i a_i + \beta \tau_0 \sigma_z + \tau_x \sigma_0 \sum_{i=x,y,z} t_i'(1 - \cos k_i a_i) - \mu \tau_0 \sigma_0, \tag{4.3}$$

where t_i, t_i' are nearest-neighbor hopping energies, a_i are lattice constants, and μ is the chemical potential. For simplicity we will equate $a_i = a_0$ and $t_i = t_i' = t_0$ for $i = x, y, z$.

The Pauli matrices σ_i ($i = x, y, z$, with $i = 0$ for the unit matrix) act on the spin degree of freedom of the surface electrons in the topological insulator layers. The $\tau_z = \pm 1$ index distinguishes the orbitals on the top and bottom surfaces. Magnetic impurities in the topological insulator layers produce a perpendicular magnetization, leading to an exchange splitting β. A Weyl point with a linear dispersion appears at $\boldsymbol{k} = (0, 0, \pm\beta/a_0 t_0)$. For ease of notation we will set a_0, t_0, and $\hbar$ to unity.

Following Meng and Balents [12], the spacer layer may have a spin-singlet s-wave pair potential $\Delta = \Delta_0 e^{i\phi}$. The pair potential induces superconductivity in the top and bottom surfaces of the topological insulator layers, as described by the Bogoliubov-De Gennes Hamiltonian

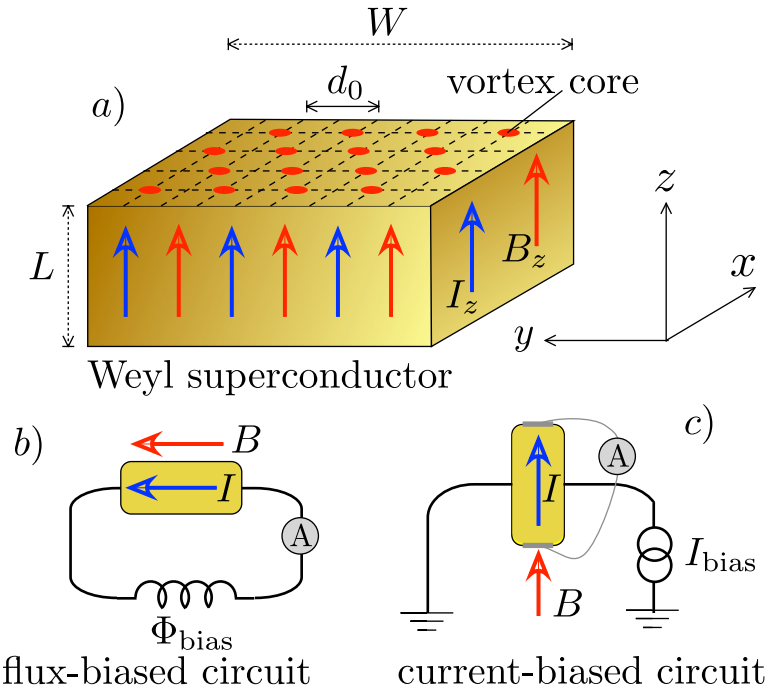

Figure 4.2: Panel a) shows a square vortex lattice in a Weyl superconductor, panels b) and c) show a circuit to measure the chiral magnetic effect (current I parallel to an external magnetic field B). The current exists in equilibrium because Weyl fermions having one of the two chiralities are confined to vortex cores by a flux bias (panel b) or a current bias (panel c).

$$\mathcal{H}(\boldsymbol{k}) = \begin{pmatrix} H_0(\boldsymbol{k} - e\boldsymbol{A}) & \Delta_0 e^{i\phi} \\ \Delta_0 e^{-i\phi} & -\sigma_y H_0^*(-\boldsymbol{k} - e\boldsymbol{A})\sigma_y \end{pmatrix}. \tag{4.4a}$$

We have introduced a vector potential $\boldsymbol{A}$ and take the electron charge $e > 0$. For definiteness we also fix the sign $\beta > 0$. The Fermi velocity $v_\mathrm{F} = a_0 t_0/\hbar$ is unity for our chosen units.

As shown in Fig. 4.2, the heterostructure can be placed in either a flux-biased or a current-biased circuit. We seek the current I_z in equilibrium, parallel to the external magnetic field $\boldsymbol{B} = \nabla \times \boldsymbol{A}$ in the z-direction.

The superconductor has length L parallel to B, while the dimensions in the perpendicular direction are $W \times W$, large compared to the London

penetration length λ. This is the key difference with Ref. 47, where $W < \lambda$ was assumed in order to prevent the formation of Abrikosov vortices. For $W \gg \lambda \gg l_m \gg \xi_0$ (with $l_m = \sqrt{\hbar/eB}$ the magnetic length and $\xi_0 = \hbar v_{\rm F}/\Delta_0$ the superconducting coherence length) we are in the vortex phase of a strong-type-II superconductor, where the magnetic field penetrates in the form of vortices of magnetic flux $\Phi_0 = h/2e$. The vortex lattice has two vortices per unit cell, we take the square array (lattice constant d_0) indicated in Fig. 4.2.

In the gauge with $\nabla \cdot \boldsymbol{A} = 0$ the superconducting phase is determined by

$$\nabla \times \nabla\phi(\boldsymbol{r}) = 2\pi\hat{z}\sum_n \delta(\boldsymbol{r} - \boldsymbol{R}_n), \quad \nabla \cdot \nabla\phi = 0. \tag{4.5}$$

The first equation specifies a 2π winding of the phase around each vortex core at $\boldsymbol{R}_n$, and the second equation ensures that the superconducting velocity

$$m\boldsymbol{v}_s = \tfrac{1}{2}\nabla\phi - e\boldsymbol{A} \tag{4.6}$$

has vanishing divergence. Since the vortex cores occupy only a small fraction $(\xi_0/l_m)^2$ of the volume, we may take a uniform pair potential amplitude $|\Delta| = \Delta_0$ and a uniform magnetic field strength $|\boldsymbol{B}| = B_0$. The dominant effect of the vortex lattice is the purely quantum mechanical scattering of quasiparticles by the superconducting phase [1].

The vector potential contains a constant contribution $A_z = \Lambda/e$ in the z-direction controlled by either the flux bias or the current bias [82]:

$$\Lambda = \begin{cases} (e/L)\Phi_{\rm bias} & \text{(flux bias)}, \\ e\mu_0(\lambda/W)^2 I_{\rm bias} & \text{(current bias)}. \end{cases} \tag{4.7}$$

4.3 Chirality confinement in a vortex lattice

In the absence of a vortex lattice, for $W < \lambda$, it was shown in Ref. 47 that a flux bias or current bias confines Weyl fermions of one definite chirality to the surfaces parallel to the magnetic field, gapping them out in the bulk. Here we consider the opposite regime $W \gg \lambda$ in which a vortex lattice forms in the Weyl superconductor. We will show that effect of the Λ bias is qualitatively different: both chiralities remain gapless in the bulk, but one of the two chiralities is confined to the vortex cores.

The analytics is greatly simplified if the magnetic field is along the same z-axis as the separation of the Weyl cones. The corresponding vector potential is

$$\boldsymbol{A}(\boldsymbol{r}) = (B_0 y, 0, \Lambda/e), \quad \Lambda = (e/L)\Phi_{\rm bias}, \tag{4.8}$$

where for definiteness we take $\Lambda \geq 0$. This is the flux-biased geometry of Fig. 4.2b. Numerical simulations indicate that the current-biased geometry of Fig. 4.2c, with $\boldsymbol{B}$ along the y-axis, is qualitatively similar — but we have not succeeded in obtaining a complete analytical treatment in that geometry.

4.3.1 Landau bands

We have calculated the eigenvalues and eigenfunctions of the tight-binding Hamiltonian (4.4) using the *Kwant* code [52] as described in Ref. 57. We take parameters $\beta = t_0$, $\Delta_0 = 0.5\, t_0$, $\mu = 0$. We arrange $h/2e$ vortices on the square lattice shown in Fig. 4.2a. The lattice constant $d_0 = Na_0$ of the vortex lattice determines the magnetic field $B_0 = (h/e)d_0^{-2}$. In the numerics the full nonlinear $\boldsymbol{k}$-dependence of $\mathcal{H}(\boldsymbol{k})$ is used, while for the analytical expressions we expand near $\boldsymbol{k} = 0$.

The zero-field spectra in Figs. 4.3a and 4.3b reproduce the findings of Ref. 47: For small Λ and provided that $\Delta_0 < \beta$ one sees two pairs of oppositely charged gapless Weyl cones, symmetrically arranged around $k_z = 0$ at momenta $K_\pm$ and $-K_\pm$ given by

$$K_\pm = \sqrt{(\beta \pm \Lambda)^2 - \Delta_0^2}. \tag{4.9}$$

The pair at $|k_z| = K_-$ is displaced relative to the other pair at $|k_z| = K_+$ by the flux bias Λ, becoming gapped when Λ is in the critical range

$$\Lambda \in (\beta - \Delta_0, \beta + \Delta_0) \equiv (\Lambda_{c1}, \Lambda_{c2}). \tag{4.10}$$

Application of a magnetic field in Figs. 4.3c and 4.3d shows the formation of chiral zeroth-order Landau bands: a pair of electron-like Landau levels of opposite chirality and a similar pair of hole-like Landau levels. The Landau bands have a linear dispersion in the z-direction, along the magnetic field, while they are dispersionless flat bands in the x–y plane.

For k_z near $K_\pm$ the electron-like and hole-like dispersions are given by [57]

$$\begin{aligned} E_{\text{electron}}(\boldsymbol{k}) &= (-\mu - k_z + K_+)\cos\theta, \\ E_{\text{hole}}(\boldsymbol{k}) &= (\mu + k_z - K_-)\cos\theta, \end{aligned} \tag{4.11a}$$

and similarly near $-K_\pm$ the dispersions are

$$\begin{aligned} E_{\text{electron}}(\boldsymbol{k}) &= (-\mu + k_z + K_-)\cos\theta, \\ E_{\text{hole}}(\boldsymbol{k}) &= (\mu - k_z - K_+)\cos\theta. \end{aligned} \tag{4.11b}$$

The k_z-dependent factor $\cos\theta$ renormalizes the charge and velocity of the quasiparticles, according to [47, 83]

$$\begin{aligned}\cos\theta(\boldsymbol{k}) &= \frac{|k_z|}{\sqrt{\Delta_0^2 + k_z^2}} \\ &\to \sqrt{1 - \frac{\Delta_0^2}{(\beta \pm \Lambda)^2}} \equiv \kappa_\pm \ \text{ when } \ |k_z| \to K_\pm.\end{aligned} \tag{4.12}$$

The degeneracy of a Landau band is not affected by charge renormalization [57], each electron-like or hole-like Landau band contains

$$\mathcal{N}_0 = \tfrac{1}{2}\Phi/\Phi_0 = (e/h)\Phi \tag{4.13}$$

chiral modes, determined by the ratio of the enclosed flux $\Phi = B_0 W^2$ and the *bare* single-electron flux quantum h/e.

While the dispersion of a Landau band in the Brillouin zone changes only quantitatively with the flux bias, it does have a pronounced qualitative effect on the *spatial* extension in the x–y plane. As shown in Fig. 4.4, the intensity profile $|\psi_\pm(x,y)|^2$ of a zeroth-order Landau level at $|k_z| = K_\pm$ peaks when $\boldsymbol{r} = (x,y)$ approaches a vortex core at $\boldsymbol{R}_n$. The dependence on the separation $\delta r = |\boldsymbol{r} - \boldsymbol{R}_n|$ is a power law [57],

$$|\psi_\pm|^2 \propto \delta r^{-1+\kappa_\pm}. \tag{4.14}$$

When Λ enters the critical range (4.10) this power law decay applies only to one of the two chiralities: the two Landau bands at $k_z = K_+$ and $k_z = -K_+$ with $dE/dk_z < 0$ still have the power law decay (4.14), but the other two bands with $dE/dk_z > 0$ merge at $k_z = 0$ and become *exponentially confined* to a vortex core. As we shall derive in the next subsection,

$$\begin{aligned}&|\psi_{\text{vortex}}|^2 \propto \exp(-\delta r/l_{\text{conf}}), \\ &l_{\text{conf}} = \tfrac{1}{2}\max\left(\frac{1}{\Lambda - \beta + \Delta_0}, \frac{1}{\beta - \Lambda + \Delta_0}\right).\end{aligned} \tag{4.15}$$

These two vortex-core bands are separated spatially, one in each of the two vortices in the unit cell. They form unpaired Majorana fermions, in contrast to the two Landau bands that overlap spatially and as a pair constitute a Dirac fermion.

All of this applies to magnetic fields in the regime $W \gg \lambda \gg l_m \gg \xi_0$ of a vortex lattice. At weaker fields, when $l_m \gtrsim \min(W, \lambda)$, no vortices can form and the analysis of Ref. 57 applies: The bands with chirality $dE/dk_z > 0$ are pushed out of the bulk and confined to the surfaces along the z-direction.

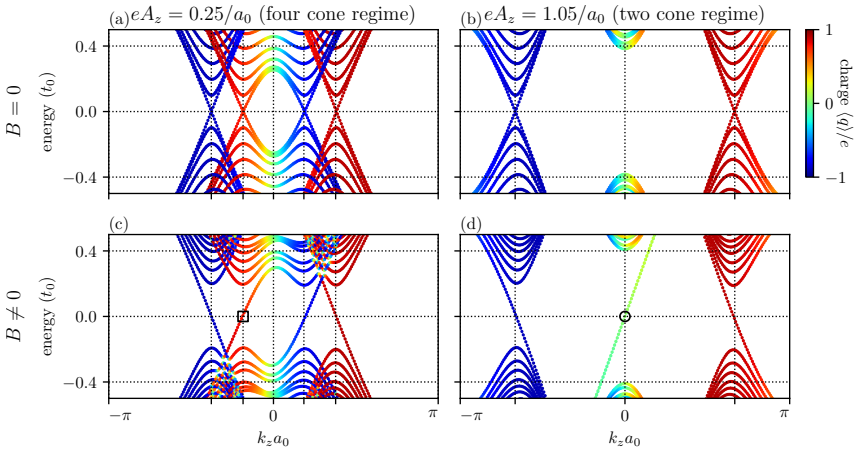

Figure 4.3: Dispersion relations of a Weyl superconductor at two values of the flux bias A_z (left and right column), without and with a magnetic field B (top and bottom row). In zero field and at a small value of the flux bias (panel a), there are four cones in the spectrum. As the flux bias increases the electron-like cones (red) are shifted to positive k_z, whereas the hole-like cones (blue) are shifted to negative k_z. At the critical value $eA_z = \beta - \Delta_0 = 0.5/a_0$ two cones of opposite chirality meet at $k_z = 0$, a gap opens and the system transitions into the two-cone regime (panel b). When a magnetic field is applied, each Weyl cone gives rise to a chiral zeroth Landau level (panel c). In the two-cone regime (panel d) a pair of chiral Landau levels forms charge-neutral Majorana modes (green). The spectra were calculated for the tight-binding Hamiltonian (4.4), with $\beta = t_0$, $\Delta = 0.5t_0$, and $\mu = 0$. The $B \neq 0$ data is for a square vortex lattice with lattice constant $d_0 = 18a_0$. For an electron-like Landau level marked with a square and for a Majorana mode marked with a circle we show the spatial probability density in Fig. 4.4.

4.3.2 Vortex core bands

To demonstrate the exponential confinement in a vortex core of the $\tau_z = +1$ chirality we expand the Hamiltonian (4.4) to first order in k_x, k_y at $k_z = 0$, $\mu = 0$,

$$\mathcal{H} = \begin{pmatrix} k_x\sigma_x + k_y\sigma_y & 0 \\ 0 & -k_x\sigma_x - k_y\sigma_y \end{pmatrix} + \begin{pmatrix} (\beta - \Lambda)\sigma_z & \Delta_0 e^{i\varphi} \\ \Delta_0 e^{-i\varphi} & (\beta - \Lambda)\sigma_z \end{pmatrix}. \tag{4.16}$$

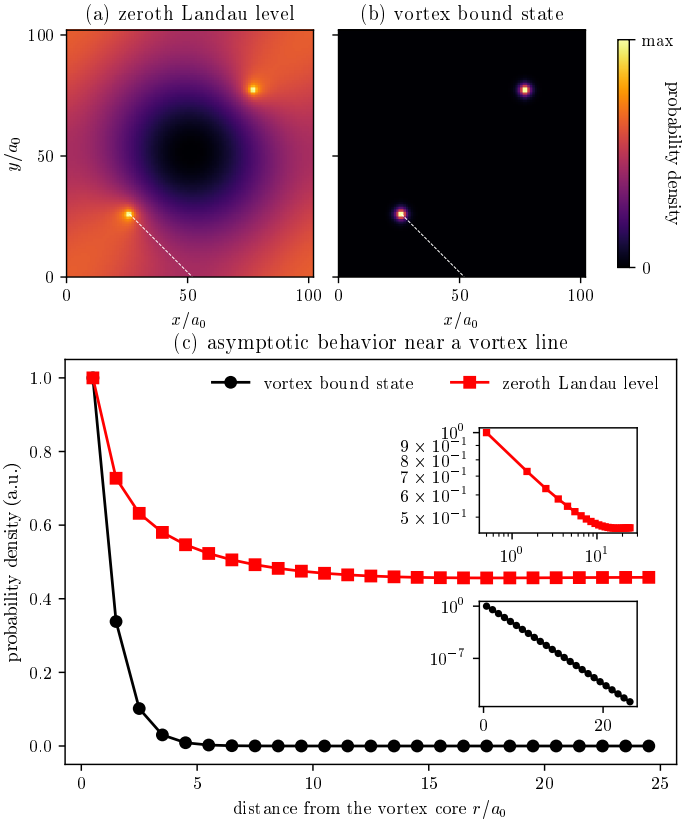

Figure 4.4: Spatial distribution of the probability density for an electron-like Landau band (panel *a*) and for a Majorana vortex-core band (panel *b*). Panel *c* shows both probability distributions as a function of the distance r from the vortex core, measured along the dashed white line in panels *a,b*. In the insets in panel *c* the same data is presented using a log-log scale (for the zeroth Landau level) and log-linear scale (for the vortex-core band). The Landau band is spread over the magnetic unit cell, with an *algebraic* divergence at the vortex cores, whereas the vortex-core band is *exponentially* localized at the vortices. The profiles were calculated for the same set of parameters as the spectra in Fig. 4.3, with the Landau band corresponding to the state marked with a square, and the vortex-core band corresponding to the state marked with a circle. To improve the spatial resolution, we used a larger ratio $d_0/a_0 = 102$.

The applied magnetic field does not contribute on length scales below l_m, so we only need to include the constant $eA_z = \Lambda$ term in the vector potential. The winding of the superconducting phase is accounted for by the factor $e^{i\varphi}$, in polar coordinates $(x, y, z) = (r\cos\varphi, r\sin\varphi, z)$ centered on the vortex core.

In view of the identity

$$\partial_x + i\partial_y = e^{i\varphi}\big(\partial_r + ir^{-1}\partial_\varphi\big), \tag{4.17}$$

with $\partial_q \equiv \partial/\partial q$, the Hamiltonian (4.16) reads

$$\mathcal{H} = \begin{pmatrix} (\beta-\Lambda)\sigma_z - D & \Delta_0 e^{i\varphi} \\ \Delta_0 e^{-i\varphi} & (\beta-\Lambda)\sigma_z + D \end{pmatrix}, \tag{4.18a}$$

$$D = \begin{pmatrix} 0 & e^{-i\varphi}(i\partial_r + r^{-1}\partial_\varphi) \\ e^{i\varphi}(i\partial_r - r^{-1}\partial_\varphi) & 0 \end{pmatrix}. \tag{4.18b}$$

We seek a solution $\mathcal{H}\Psi = 0$ of the form

$$\Psi = \big(\phi_1(r), e^{i\varphi}\phi_2(r), e^{-i\varphi}\phi_3(r), \phi_4(r)\big), \tag{4.19}$$

and denote $\Phi = (\phi_1, \phi_2, \phi_3, \phi_4)$. This produces the ordinary differential equation

$$\begin{aligned} -\frac{d\Phi}{dr} &= \begin{pmatrix} 0 & -i(\beta-\Lambda) & 0 & i\Delta_0 \\ i(\beta-\Lambda) & r^{-1} & i\Delta_0 & 0 \\ 0 & -i\Delta_0 & r^{-1} & i(\beta-\Lambda) \\ -i\Delta_0 & 0 & -i(\beta-\Lambda) & 0 \end{pmatrix}\Phi \\ &\equiv \big(M_1 + r^{-1}M_2\big)\Phi. \end{aligned} \tag{4.20}$$

In the critical regime $\Lambda_{c1} < \Lambda < \Lambda_{c2}$ the two positive eigenvalues of the matrix M_1 are $\Lambda - \Lambda_{c1}$ and $\Lambda_{c2} - \Lambda$. At large r, the normalizable solution of Eq. (4.20) decays $\propto e^{-\alpha r}$, with α the smallest positive eigenvalue of M_1:

$$\alpha = \min(\Lambda - \Lambda_{c1}, \Lambda_{c2} - \Lambda). \tag{4.21}$$

The confinement length $l_{\mathrm{conf}} = 1/2\alpha$ is thus given by Eq. (4.15).

4.4 Chiral magnetic effect

4.4.1 Charge renormalization

We summarize the formulas from Ref. 47 that show how charge renormalization by the superconductor affects the CME.

The equilibrium expectation value I_z of the electrical current in the z-direction is given by

$$I_z = \tfrac{1}{2} \sum_n \int \frac{dk_z}{2\pi} f(E) \langle j_z \rangle_E. \tag{4.22}$$

The sum over n is over transverse modes with energy $E_n(k_z) \equiv E$ at longitudinal momentum k_z, weighted by the Fermi function $f(E) = (1 + e^{E/k_B T})^{-1}$ at temperature T. The factor $1/2$ corrects for a double-counting of states in the Bogoliubov-De Gennes formalism. The expectation value of the current operator $j_z = -\partial H/\partial A_z$ in the state with energy E equals

$$\langle j_z \rangle_E = -\langle \partial H/\partial A_z \rangle_E = -\partial E/\partial A_z, \tag{4.23}$$

according to the Hellmann-Feynman theorem. Two other expectation values that we need are those of the velocity operator $v_z = \partial H/\partial k_z$ and the charge operator $Q = -e\partial H/\partial \mu$, given by

$$\langle v_z \rangle_E = \partial E/\partial k_z, \quad \langle Q \rangle_E = -e\partial E/\partial \mu. \tag{4.24}$$

Following Ref. 47 we also define the "vector charge"

$$\boldsymbol{Q} = (Q_x, Q_y, Q_z), \quad \text{with} \quad Q_\alpha(E) \equiv \frac{\langle j_\alpha \rangle_E}{\langle v_\alpha \rangle_E}, \tag{4.25}$$

which may be different from the average (scalar) charge $Q_0 \equiv \langle Q \rangle_E$ because the average of the current as the product of charge and velocity may differ from the product of the averages.

The CME is a contribution to I_z that is linear in the equilibrium chemical potential μ, measured relative to the Weyl points. We extract this contribution by taking the derivative $\partial_\mu I_z$ in the limit $\mu \to 0$. Two terms appear, an *on-shell* term from the Fermi level and an *off-shell* term from energies below the Fermi level,

$$\partial_\mu I_z = \mathcal{J}_{\text{on-shell}} + \mathcal{J}_{\text{off-shell}} \equiv \mathcal{J}_{\text{total}}, \tag{4.26a}$$

$$\mathcal{J}_{\text{on-shell}} = -\frac{1}{2e} \sum_n \int \frac{dk_z}{2\pi} f'(E) \langle Q \rangle_E \langle j_z \rangle_E, \tag{4.26b}$$

$$\mathcal{J}_{\text{off-shell}} = -\frac{1}{2} \sum_n \int \frac{dk_z}{2\pi} f(E) \frac{\partial^2}{\partial A_z \partial \mu} E_n(k_z). \tag{4.26c}$$

At low temperatures, when $-f'(E) \to \delta(E)$ becomes a delta function, the on-shell contribution $\mathcal{J}_{\text{on-shell}}$ involves only Fermi surface properties.

It is helpful to rewrite it as a sum over modes at $E = 0$. For that purpose we replace the integration over k_z by an energy integration weighted with the density of states:

$$\mathcal{J}_{\text{on-shell}} = -\frac{1}{4\pi e}\sum_n \int_{-\infty}^{\infty} dE\, f'(E) \left|\frac{\partial E}{\partial k_z}\right|^{-1} \langle Q\rangle_E \langle j_z\rangle_E. \tag{4.27}$$

In the $T \to 0$ limit a sum over modes remains,

$$\mathcal{J}_{\text{on-shell}} = \frac{1}{2}\frac{e}{h}\sum_n \frac{Q_0 Q_z}{e^2}\left(\operatorname{sign}\langle v_z\rangle\right)\Big|_{E_n=0}, \tag{4.28}$$

where we have restored the units of $\hbar = h/2\pi$.

4.4.2 On-shell contributions

We apply Eq. (4.28) to the vortex lattice of the flux-biased Weyl superconductor. Derivatives with respect to A_z are then derivatives with respect to the flux bias Λ. According to the dispersion relation (4.11a), the electron-like Landau band near K_+ has renormalized charges

$$Q_0 = e\kappa_+, \;\; Q_z = e\frac{\partial K_+}{\partial \Lambda} = \frac{e}{\kappa_+}, \tag{4.29}$$

in the limit $k_z \to K_+$, $\mu \to 0$. The charge renormalization factors cancel, so this Landau band with $\operatorname{sign}\langle v_z\rangle < 0$ contributes to $\mathcal{J}_{\text{on-shell}}$ an amount $-\frac{1}{2}e/h$ times the degeneracy $\mathcal{N}_0 = (e/h)\Phi$, totalling $-\frac{1}{2}(e/h)^2\Phi$.

Similarly, for the hole-like Landau band near $-K_-$ Eq. (4.11a) gives

$$Q_0 = -e\kappa_+, \;\; Q_z = -e\frac{\partial K_+}{\partial \Lambda} = -\frac{e}{\kappa_+}, \tag{4.30}$$

for the same contribution of $-\frac{1}{2}(e/h)^2\Phi$. The total on-shell contribution for this chirality is

$$\mathcal{J}_{\text{on-shell}}(|k_z| = K_+) = -(e/h)^2\Phi. \tag{4.31}$$

We can repeat the calculation for the electron-like band near K_- and the hole-like band near $-K_-$, the only change is the sign $\langle v_z\rangle > 0$, resulting in

$$\mathcal{J}_{\text{on-shell}}(|k_z| = K_-) = (e/h)^2\Phi. \tag{4.32}$$

We conclude that the Dirac fermions in the Landau bands of opposite chirality give identical opposite on-shell contributions $\pm(e/h)^2\Phi$ to $\partial_\mu I_z$.

The net result vanishes when Λ is outside of the critical region $(\Lambda_{c1}, \Lambda_{c2})$. When $\Lambda_{c1} < \Lambda < \Lambda_{c2}$ one of the two chiralities is transformed into unpaired Majorana fermions confined to the vortex cores. The vortex-core bands have $Q_0 = 0$ at $E = 0$, so they have no on-shell contribution, resulting in

$$\mathcal{J}_{\text{on-shell}} = \begin{cases} 0 & \text{if } \Lambda \notin (\Lambda_{c1}, \Lambda_{c2}), \\ (e/h)^2 \Phi & \text{if } \Lambda \in (\Lambda_{c1}, \Lambda_{c2}). \end{cases} \tag{4.33}$$

The coefficient $(e/h)^2$ contains the bare charge, unaffected by the charge renormalization.

4.4.3 Off-shell contributions

Turning now to the off-shell contributions (4.26c), we note that the Landau bands do not contribute in view of Eq. (4.11):

$$\frac{\partial^2}{\partial \Lambda \partial \mu} E(\boldsymbol{k}) = \pm \frac{\partial}{\partial \Lambda} \cos\theta(\boldsymbol{k}) = 0. \tag{4.34}$$

For the vortex-core bands, off-shell contributions cancel because of particle-hole symmetry.

This does not exclude off-shell contributions from states far below the Fermi level, where our entire low-energy analysis no longer applies. In fact, as we show in Figs. 4.5 and 4.6, we do find a substantial off-shell contribution to $\partial_\mu I_z$ in our numerical calculations (see App. 4.A for details). Unlike the on-shell contribution (4.33), which has a discontinuity at $\Lambda = \Lambda_{c1}, \Lambda_{c2}$, the off-shell contribution depends smoothly on the flux bias and can therefore be extracted from the data.

4.5 Conclusion

In summary, we have demonstrated that a flux bias in a Weyl superconductor drives a confinement/deconfinement transition in the vortex phase: For weak flux bias the subgap excitations are all delocalized in the plane perpendicular to the vortices. With increasing flux bias a transition occurs at which half of the states become exponentially localized inside the vortex cores. The localized states have a definite chirality, meaning that they all propagate in the same direction along the vortices. (The sign of the velocity is set by the sign of the external magnetic field B_0.)

As a physical consequence of this topological phase transition we have studied the chiral magnetic effect. The states confined to the vortex cores

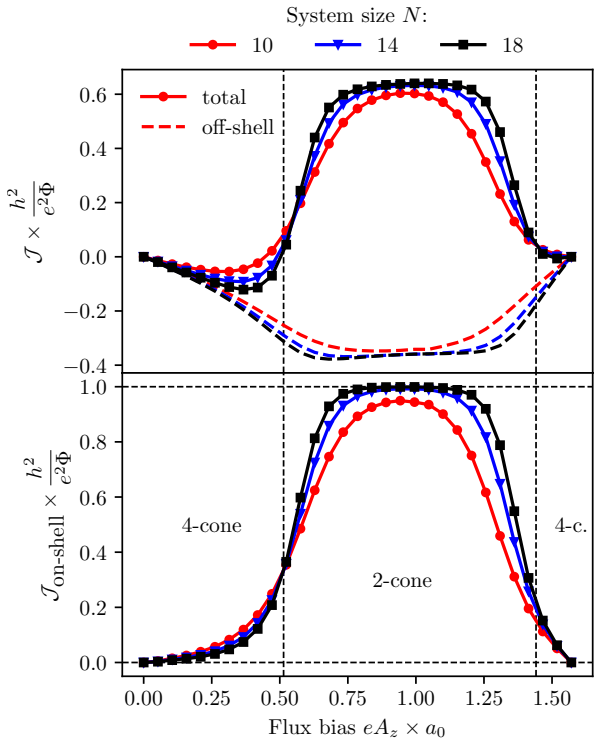

Figure 4.5: Numerical calculation of $\partial_\mu I_z$ at $\mu = 0.05\,t$ in the tight-binding Hamiltonian (4.4). The solid curves are the total current, while the dashed curves show only the off-shell contribution (4.26c). The vertical dashed lines mark $eA_z = \Lambda_{c1}, \Lambda_{c2}$ – the values of the flux bias which correspond to a topological phase transition into and out of the two-cone regime. The horizontal dashed lines mark the universal CME value of $(h/e)^2\Phi$. As the size $N = d/a_0$ of the magnetic unit cell increases, the numerically calculated value of the on-shell contribution approaches the universal value, which jumps at the topological phase transition.

are charge-neutral Majorana fermions, so they carry no electrical current. The states of opposite chirality, which remain delocalized, are charged, and because they all move in the same direction they can carry a nonzero current density j parallel to the vortices. This is an equilibrium supercurrent, proportional to the magnetic field B_0 and to the chemical potential μ (measured relative to the Weyl point).

We have calculated that the supercurrent along the vortices jumps at

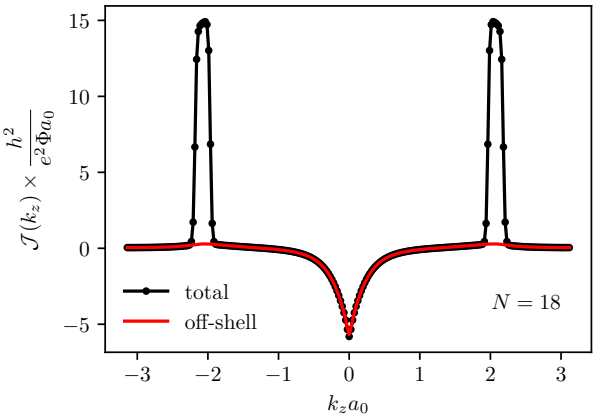

Figure 4.6: Same numerical calculation as in Fig. 4.5, but now for a fixed flux bias $eA_z = 1.05/a_0$ in the two-cone regime, showing the contributions to $\partial_\mu I_z$ from different momenta k_z along the magnetic field. We distinguish between the total current and the off-shell contribution. The difference between the two is the on-shell contribution, which peaks at the momenta where the Fermi level crosses the chiral Landau bands. The vortex-core bands at $k_z = 0$ have vanishing on-shell contribution.

the topological phase transition by an amount which for a large system size tends to the universal limit

$$j = \frac{e^2}{h^2} B_0 \mu. \tag{4.35}$$

Remarkably enough, the proportionality constant contains the bare electron charge e, even though the quasiparticles have a renormalized charge $e^* < e$. This electromagnetic response is generated by the axion term $(e/h)^2 \int dt \int d\boldsymbol{r}\, \theta(t)\, E_z B_z$ in the Lagrangian, where $\theta(t) = \mu t$ is the axion angle.

The chiral fermions confined in the vortex cores are a superconducting realization of the "topological coaxial cable" of Schuster *et al.* [84], where the fermions are confined to vortex lines in a Higgs field. There is one difference: the chiral fermions in the Higgs field are charge-e Dirac fermions, while in our case they are charge-neutral Majorana fermions. The difference manifests itself in the physical observable that serves as a signature of the confinement: for Schuster *et al.* this is a quantized current $dI/dV = e^2/h$ per vortex out of equilibrium, in our case it is a quantized current $dI/d\mu = \frac{1}{2} e/h$ per vortex in equilibrium.

Appendix

4.A Details of the numerical calculation

The numerical calculation was performed on a square lattice with two $h/2e$ vortices in a magnetic unit cell, using the discretization described in Ref. 57. We calculate separately the total induced current response

$$\partial_\mu I_z = \mathcal{J}_{\text{on-shell}} + \mathcal{J}_{\text{off-shell}} \equiv \mathcal{J}_{\text{total}}, \tag{4.36}$$

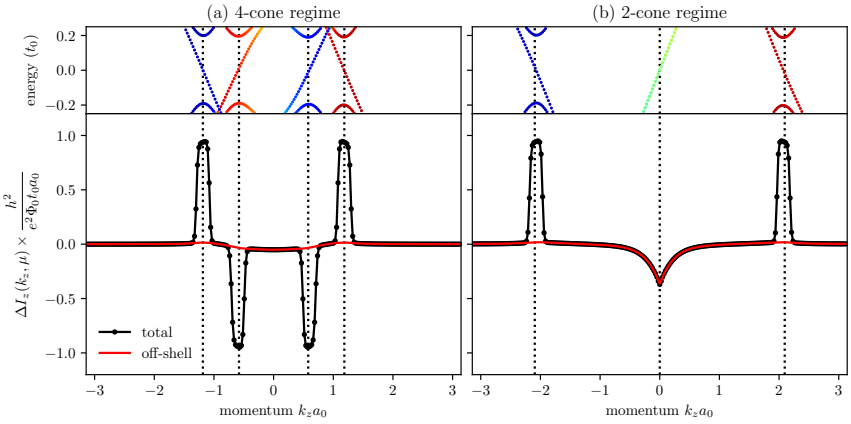

Figure 4.7: Bottom: momentum-resolved current response $\Delta I_z(\mu, k_z)$, as defined in Eqs. (4.37) and (4.39), in the four-cone regime at $eA_z = 0.25/a_0$ (panel a) and in the two-cone regime at $eA_z = 1.05/a_0$ (panel b). Top: low-energy dispersion relation for the corresponding system. The on-shell contribution to the current response, which is the difference between the total and off-shell contributions, only appears at momenta for which a band crosses the Fermi energy. In the four-cone regime four peaks are present, the contributions of which cancel out. In the two-cone regime the vortex-core band at $k_z = 0$ has a vanishing on-shell contribution, whereas the contribution of the other two Landau levels remains unchanged. The plots were obtained for a system size $N = 18$.

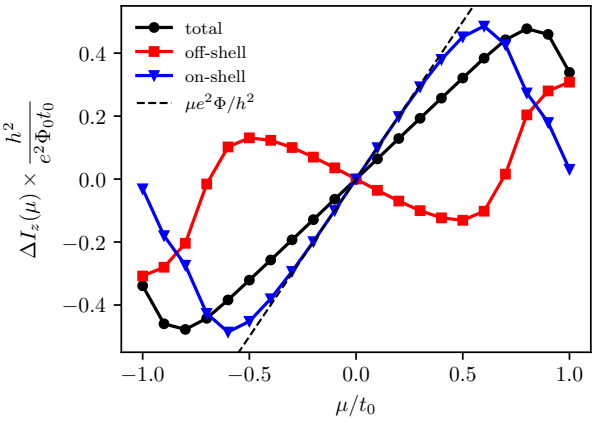

Figure 4.8: The current response $\Delta I_z(\mu)$, as defined in Eqs. (4.37) and (4.39), in the two-cone regime at $eA_z = 1.05/a_0$ for a finite chemical potential μ. The colored data points give the total response, as well as the off-shell and on-shell contributions. The dotted line $\mu e^2\Phi/h^2$ is the theoretical prediction (4.33) for the on-shell contribution to first order in μ, which is a good approximation to the numerical result for small μ. The plots were obtained for a system size $N = 18$.

and the off-shell contribution $\mathcal{J}_{\text{off-shell}}$. The defining equations (4.22) and (4.26c) are rewritten in terms of finite differences,

$$\begin{aligned}
\mathcal{J}_{\text{total}} &= \frac{1}{2}\lim_{\mu\to 0}\frac{1}{2\mu}\sum_n \int \frac{dk_z}{2\pi}\Big[f\big(E_n(k_z,\mu)\big)\langle j_z\rangle_{E_n(k_z,\mu)} \\
&\quad - f\big(E_n(k_z,-\mu)\big)\langle j_z\rangle_{E_n(k_z,-\mu)}\Big] \\
&= \frac{1}{2}\lim_{\mu\to 0}\frac{1}{2\mu}\int dk_z\,\Delta I_z^{\text{total}}(\mu,k_z) = \lim_{\mu\to 0}\frac{1}{\mu}\Delta I_z^{\text{total}}(\mu), \qquad (4.37)\\
\mathcal{J}_{\text{off-shell}} &= \frac{1}{2}\lim_{\mu\to 0}\frac{1}{2\mu}\sum_n \int \frac{dk_z}{2\pi} f\big(E_n(k_z,\mu=0)\big)\Big[\langle j_z\rangle_{E_n(k_z,\mu)} \qquad (4.38)\\
&\quad - \langle j_z\rangle_{E_n(k_z,-\mu)}\Big] \\
&= \frac{1}{2}\lim_{\mu\to 0}\frac{1}{2\mu}\int dk_z\,\Delta I_z^{\text{off-shell}}(\mu,k_z) = \lim_{\mu\to 0}\frac{1}{\mu}\Delta I_z^{\text{off-shell}}(\mu). \\
& \qquad (4.39)
\end{aligned}$$

We computed the values of the expressions on the right-hand-side at

finite μ. The k_z-integral was estimated from 256 values of k_z, equally spaced in the $[-\pi, \pi]$ interval. For the sum over transverse modes n we averaged over 4 values of both k_x and k_y. To smoothen the integrand we took a small nonzero temperature $T = 0.01$ in the Fermi function — much smaller than the energy of the first Landau level (which was $\gtrsim 0.2$ for the parameters we considered). In Fig. 4.7 we present the results prior to integration over k_z, for two different values of A_z. For $\mu = 0.05$ the finite differences have converged to the derivative – see Fig. 4.8.

5 Deconfinement of Majorana vortex modes produces a superconducting Landau level

5.1 Introduction

Deconfinement transitions in physics refer to transitions into a phase where particles can exist as delocalized states, rather than only as bound states. Unlike thermodynamic phase transitions, the deconfinement transition is not associated with a spontaneously broken symmetry but with a change in the momentum space topology of the ground state [85]. A prominent example in superconductors is the appearance of a Fermi surface for Bogoliubov quasiparticles when a superconductor becomes gapless [86–89]. Such a Bogoliubov Fermi surface has been observed recently [15].

Motivated by these developments we consider here the deconfinement transition for Majorana zero-modes in the vortex core of a topological superconductor. We will demonstrate, analytically and by numerical simulations, that the delocalized phase at zero chemical potential remains a highly degenerate zero-energy level — a superconducting counterpart of the Majorana Landau level in a Kitaev spin liquid [90, 91]. Unlike a conventional electronic Landau level, the Majorana Landau level has a non-uniform density profile: quantum interference of the electron and hole components creates spatial oscillations with a wave vector set by the Cooper pair momentum that drives the deconfinement transition.

The system of Ref. 15 is shown in Fig. 5.1. It is a thin layer of topological insulator deposited on a bulk superconductor, such that the proximity effect induces a pairing gap Δ_0 in the surface states. A superflow with Cooper pair momentum $\boldsymbol{K}$ lowers the excitation energy for quasiparticles with velocity $\boldsymbol{v}$ by the Doppler shift $\boldsymbol{v}\cdot\boldsymbol{K}$, closing the gap when vK exceeds Δ_0. Following Fu and Kane [14], we add a perpendicular magnetic field B to confine a Majorana zero-mode to the core of each $h/2e$ vortex that

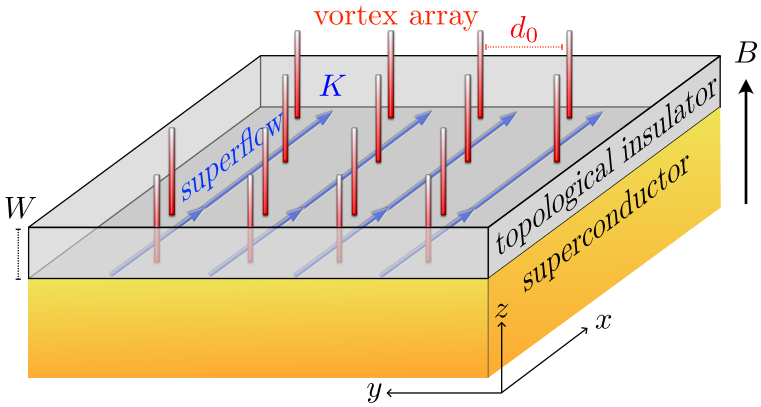

Figure 5.1: Schematic of the Fu-Kane heterostructure [14], a topological insulator with induced superconductivity (gap Δ_0) in a perpendicular magnetic field B. Vortices (red) bind midgap states known as Majorana zero-modes. Here we study the deconfinement transition in response to an in-plane supercurrent (blue arrows, momentum K). When $vK > \Delta_0$ the zero-modes delocalize into a Majorana Landau level.

penetrates the superconductor. We seek to characterize the deconfined phase that emerges when $vK > \Delta_0$.

5.2 Confined phase

To set the stage we first investigate the confined phase for $vK < \Delta_0$. Electrons on the two-dimensional (2D) surface of a 3D topological insulator have the Dirac Hamiltonian $v\boldsymbol{k}\cdot\boldsymbol{\sigma} - \mu$, with μ the chemical potential, v the energy-independent Fermi velocity, $\boldsymbol{k} = (k_x, k_y)$ the momentum operator in the x–y surface plane, and $\boldsymbol{\sigma} = (\sigma_x, \sigma_y)$ two Pauli spin matrices. (The 2×2 unit matrix σ_0 is implicit when the Hamiltonian contains a scalar term.) Application of a perpendicular magnetic field B (in the z-direction), adds an in-plane vector potential $\boldsymbol{A} = (A_x, A_y)$ to the momentum, $\boldsymbol{k} \mapsto \boldsymbol{k} - e\boldsymbol{A}$. The electron charge is $+e$ and for ease of notation we will set v and $\hbar$ both equal to unity in most equations.

The superconducting substrate induces a pair potential $\Delta = \Delta_0 e^{i\phi}$. The phase field $\phi(\boldsymbol{r})$ winds by $\pm 2\pi$ around each vortex, at position $\boldsymbol{R}_n$, as expressed by

$$\nabla \times \nabla\phi(\boldsymbol{r}) = \pm 2\pi\hat{z}\textstyle\sum_n \delta(\boldsymbol{r} - \boldsymbol{R}_n), \quad \nabla^2\phi = 0. \tag{5.1}$$

The pair potential couples electrons and holes in the 4×4 Bogoliubov-De Gennes (BdG) Hamiltonian

$$H = \begin{pmatrix} K\sigma_x + (\boldsymbol{k} - e\boldsymbol{A}) \cdot \boldsymbol{\sigma} & \Delta_0 e^{i\phi} \\ \Delta_0 e^{-i\phi} & K\sigma_x - (\boldsymbol{k} + e\boldsymbol{A}) \cdot \boldsymbol{\sigma} \end{pmatrix}, \tag{5.2}$$

at zero chemical potential, including a superflow momentum field $K \geq 0$ in the x-direction[1]. The superflow can be a screening current in response to a magnetic field in the y-direction [15], or it can result from an externally imposed flux bias or current bias. The Zeeman energy from an in-plane magnetic field has an equivalent effect [87] (although it was estimated to be negligible relative to the orbital effect of the field in the experiment [15]).

For $vK < \Delta_0$ a pair of Majorana zero-modes will appear in each vortex core, one at the top surface and one at the bottom surface. We consider these separately[2]. Setting $\Delta(\boldsymbol{r}) = \Delta_0(r)e^{\pm i\theta}$, in polar coordinates (r, θ) for a $\pm 2\pi$ phase vortex at the origin, we need to solve the zero-mode equation $H_\pm \Psi_\pm = 0$ with

$$H_\pm = \begin{pmatrix} K\sigma_x - (i\nabla + e\boldsymbol{A}) \cdot \boldsymbol{\sigma} & \Delta_0(r)e^{\pm i\theta} \\ \Delta_0(r)e^{\mp i\theta} & K\sigma_x + (i\nabla - e\boldsymbol{A}) \cdot \boldsymbol{\sigma} \end{pmatrix}. \tag{5.3}$$

The pair potential amplitude $\Delta_0(r)$ increases from 0 at $r = 0$ to a value $\Delta_0 > 0$ when r becomes larger than the superconducting coherence length $\xi_0 = \hbar v/\Delta_0$.

When $K = 0$ this is a familiar calculation [92], which is readily generalized to $K > 0$. The Majorana zero-mode has a definite chirality $\mathcal{C}$, meaning that its four-component wave function $\Psi_\pm$ is an eigenstate of the chirality operator $\Lambda = \mathrm{diag}\,(1, -1, -1, 1)$ with eigenvalue $\mathcal{C} = \pm 1$. One

[1] The term $K\sigma_x$ in the BdG Hamiltonian (5.2) is equivalent, upon a gauge transformation, to a gradient Kx in ϕ.

[2] The overlap of states on the top and bottom surfaces of the topological insulator thin film shifts the Majorana Landau away from $E = 0$ by the hybridization gap, while keeping the spatial structure of the wave functions intact. We include this effect in the calculations in App. 5.A.

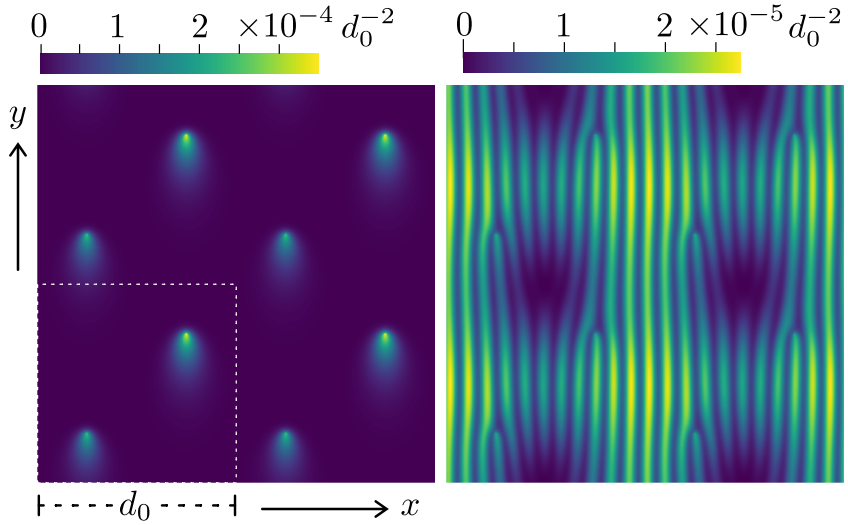

Figure 5.2: Intensity profile $|\Psi(x,y)|^2$ of a Majorana zero-mode in the vortex lattice[4]. The left panel shows the confined phase ($K < \Delta_0$), the right panel the deconfined phase ($K > \Delta_0$). The dotted square indicates the unit cell containing a pair of $h/2e$ vortices. These plots are for Majorana fermions of positive chirality, for negative chirality the density profile is inverted $y \mapsto -y$.

has $\Psi_+ = (i\psi_+, 0, 0, \psi_+)$, $\Psi_- = (0, i\psi_-, \psi_-, 0)$ with[3]

$$\psi_\pm(\boldsymbol{r}) = e^{\mp Ky} e^{\mp\chi(\boldsymbol{r})} \exp\left(-\int_0^r \Delta_0(r')\,dr'\right), \tag{5.4a}$$

$$\chi(\boldsymbol{r}) = \frac{e}{2\pi}\int d\boldsymbol{r}'\, B(\boldsymbol{r}') \ln|\boldsymbol{r}-\boldsymbol{r}'|. \tag{5.4b}$$

The factor $e^{\mp\chi(\boldsymbol{r})}$ is a power law for large r, so the zero-mode is confined exponentially to the vortex core as long as $K < \Delta_0$. When $K > \Delta_0$ the solution (5.4) is no longer normalizable, it diverges exponentially along the y-axis. This signals a transition into a deconfined phase, which we consider next.

[3] To understand how the solution (5.4) relates to the $K = 0$ solution in Ref. [92], note the (non-unitary) transformation $e^{Ky\Lambda} H_\pm e^{Ky\Lambda} = H_\pm + K\sigma_x$, with $\Lambda = \mathrm{diag}\,(1,-1,-1,1)$. The spinor $\Psi_\pm$ is an eigenstate of Λ with eigenvalue ± 1, so if $H_\pm \Psi_\pm = 0$ for $K = 0$, then $H_\pm e^{\pm Ky}\Psi_\pm = 0$ for $K \neq 0$.

[4] The data in Fig. 5.2 is obtained from the tight-binding Hamiltonian (5.14) of the topological insulator layer. The parameters are $\Delta_0 = 20\,\hbar v/d_0$, $d_0 = 302\,a_0$, $B =$

5.3 Deconfined phase

In Fig. 5.2 we show results from a numerical simulation of the deconfinement transition for the model Hamiltonian described below. The left panel shows zero-modes confined to a pair of vortex cores for $K < \Delta_0$, the right panel shows the deconfined state for $K > \Delta_0$. The decay $|\Psi| \propto e^{-Ky} e^{-\Delta_0 r}$ in the confined phase is anisotropic, with a decay rate Δ_0 along the x-axis and two different decay rates $\Delta_0 \pm K$ in the $\pm y$-direction. The direction into which the zero-mode decays more slowly is set by the chirality[5]: Fig. 5.2 shows $\mathcal{C} = +1$ with a slow decay in the $-y$ direction, for $\mathcal{C} = -1$ the slow decay is in the $+y$ direction.

In the deconfined phase the zero-mode density profile has a pronounced periodic modulation in the x-direction, parallel to the superflow, with bifuration points at the vortex cores. This striped pattern is unexpected for a Landau level. We present an analytical description.

Chiral symmetry protected Majorana Landau level — The chiral symmetry of the Hamiltonian (5.2) plays a key role in our analysis of the Majorana Landau level, similar to the role it plays for Landau level quantization in graphene [49, 50] and in a Weyl superconductor [57]. Chiral symmetry means that H at $\mu = 0$ anticommutes with Λ. The Hamiltonian then becomes block-off-diagonal in the basis of eigenstates of Λ,

$$U^\dagger H U = \begin{pmatrix} 0 & \Xi \\ \Xi^\dagger & 0 \end{pmatrix}, \quad U = \begin{pmatrix} 1 & 0 & 0 & 0 \\ 0 & 0 & 1 & 0 \\ 0 & 0 & 0 & 1 \\ 0 & 1 & 0 & 0 \end{pmatrix}, \tag{5.5a}$$

$$\Xi = \begin{pmatrix} k_- - eA_- + K & \Delta_0 e^{i\phi} \\ \Delta_0 e^{-i\phi} & -k_+ - eA_+ + K \end{pmatrix}, \tag{5.5b}$$

where we have abbreviated $k_\pm = k_x \pm i k_y$, $A_\pm = A_x \pm i A_y$.

A zero-mode is either a wave function $(u, 0)$ of positive chirality with $\Xi^\dagger u = 0$, or a wave function $(0, u)$ of negative chirality with $\Xi u = 0$. The difference between the number of normalizable eigenstates of either chirality is called the index of the Hamiltonian. It is topologically protected, meaning insensitive to perturbations [16].

---

h/ed_0^2, $\mu = 0$, $M_0 = 0$, $M_1 = 0.2\, a_0$. The vortex pair in a unit cell is at the positions $(x, y) = (d_0/4)(1, 1)$ and $(d_0/4)(3, 3)$. The superflow momentum K equals $0.8\, \Delta_0/v$ in the left panel and $2\, \Delta_0/v$ in the right panel.

[5] The anisotropic decay of the Majorana zero-mode in the left panel of Fig. 5.2 can be understood as the effect of the Magnus force which the superflow momentum $\boldsymbol{K} = K\hat{x}$ exerts on the axial spin $\boldsymbol{S} = \mathcal{C}\hat{z}$ of the Majorana fermions (as determined by their chirality $\mathcal{C} = \pm 1$). The direction of slow decay of the zero-mode is given by the cross product $\boldsymbol{K} \times \boldsymbol{S}$.

Vortices are strong scatterers [33], completely obscuring the Landau level quantization in a nontopological superconductor [1]. Here chiral symmetry ensures that the vortices cannot broaden the zeroth Landau level.

Helmholtz equation for the Majorana Landau level — Let us focus on the Landau level of positive chirality, described by the equation $\Xi^\dagger u = 0$. This 2×2 matrix differential equation can be simplified by the substitution

$$u(\boldsymbol{r}) = e^{-Ky-q(\boldsymbol{r})} e^{\frac{1}{2}i\phi(\boldsymbol{r})\sigma_z} \tilde{u}(\boldsymbol{r}), \tag{5.6}$$

$$\text{with } \partial_x q = -\tfrac{1}{2}\partial_y\phi + eA_y, \;\; \partial_y q = \tfrac{1}{2}\partial_x\phi - eA_x, \tag{5.7}$$

$$\Rightarrow \begin{pmatrix} -i\partial_x + \partial_y & \Delta_0 \\ \Delta_0 & i\partial_x + \partial_y \end{pmatrix} \tilde{u} = 0. \tag{5.8}$$

The fields $\boldsymbol{A}$, ϕ, and K no longer appear explicitly in the differential equation (5.8) for $\tilde{u}$, but they still determine the solution by the requirements of normalizability and single-valuedness of the zero-mode u.

Outside of the vortex core the spatial dependence of the pair potential amplitude Δ_0 may be neglected and one further simplification is possible: Substitution of $\tilde{u} = (f, g)$ gives $g = \Delta_0^{-1}(i\partial_x - \partial_y)f$ and a scalar second-order differential equation for f,

$$\nabla^2 f = \Delta_0^2 f. \tag{5.9}$$

In the context of classical wave equations this is the Helmholtz equation with imaginary wave vector.

Eq. (5.6) requires that $\tilde{u}$ and hence f have an exponential envelope e^{Ky} in the y-direction. The Helmholtz equation (5.9) then ties that to a plane wave $\propto e^{\pm iQx}$ in the x-direction, with wave vector $Q = \sqrt{K^2 - \Delta_0^2}$. This already explains the striped pattern in the numerical simulations of Fig. 5.2. For a more detailed comparison we proceed to a full solution of the Helmholtz equation.

Analytical solution of the Majorana Landau level wave function — The solutions of Eq. (5.9) for f are constrained by the requirements of normalizability and single-valuedness of u. To determine the normalizability constraint we use that the field $q(\boldsymbol{r})$ defined in Eq. (5.7) has the integral representation[6]

$$q(\boldsymbol{r}) = \frac{1}{2\Phi_0}\int d\boldsymbol{r}'\, B(\boldsymbol{r}') \ln|\boldsymbol{r} - \boldsymbol{r}'| - \tfrac{1}{2}\sum_n \ln|\boldsymbol{r} - \boldsymbol{R}_n|. \tag{5.10}$$

[6] The integral equation (5.10) for $q(\boldsymbol{r})$ follows from the definition (5.7), which implies that $\nabla^2 q(\boldsymbol{r}) = \hat{z}\cdot\nabla\times(e\boldsymbol{A} - \frac{1}{2}\nabla\phi) = eB - \pi\sum_n \delta(\boldsymbol{r} - \boldsymbol{R}_n)$. The Green function of this 2D Poisson equation is $(2\pi)^{-1}\ln|\boldsymbol{r} - \boldsymbol{r}'|$. Also note that $\Phi_0 \equiv \pi/e$ in units where $\hbar \equiv 1$.

We consider $\mathcal{N}$ vortices (each of $+2\pi$ vorticity) in a region S enclosing a flux $\Phi = \mathcal{N}\Phi_0$, with $\Phi_0 = h/2e$ the superconducting flux quantum[7]. If we set $B \to 0$ outside of S, the field $q(\boldsymbol{r}) \to \frac{1}{2}(\Phi/\Phi_0 - \mathcal{N}) \ln r = 0$ for $r \to \infty$. In view of Eq. (5.6), normalizability requires that $e^{-Ky} f$ is square integrable for $r \to \infty$. Near a vortex core $e^{-q} f \propto |\boldsymbol{r} - \boldsymbol{R}_n|^{1/2} f$ must be square integrable[8].

Concerning the single-valuedness, the factor $e^{i\phi/2}$ in Eq. (5.6) introduces a branch cut at each vortex position $\boldsymbol{R}_n$, across which the function f should change sign — to ensure a single-valued u. This is a local constraint: branch cuts can be connected pairwise, hence there is no sign change in f on a contour encircling a vortex pair.

We have obtained an exact analytical solution[9] of the Helmholtz equation in the limit that the separation of a vortex pair goes to zero. We place the two vortices at the origin of a disc of radius R, enclosing a flux h/e, with zero magnetic field outside of the disc. The envelope function then equals $e^{-q(r)} = r_{\min} e^{-r_{\min}^2/2R^2}$, with $r_{\min} = \min(r, R)$.

The two independent solutions are given by $\tilde{u} = (f_1, f_0)$ and $\tilde{u}' = \sigma_x \tilde{u}^*$, with

$$f_n = 2i^n e^{-in\theta} \mathrm{K}_n(\Delta_0 r) - \int_{-Q}^{Q} dp\, C_n(p) e^{ixp + y\sqrt{\Delta_0^2 + p^2}},$$
$$C_n(p) = \Delta_0^{-n} (\Delta_0^2 + p^2)^{-1/2} \big(p - \sqrt{\Delta_0^2 + p^2}\big)^n. \tag{5.11}$$

The vortex pair is at the origin, with $x + iy = re^{i\theta}$, and K_n is a Bessel function.

The corresponding zero-modes follow from Eq. (5.6),

$$u = e^{-q(r)} e^{-Ky} (e^{i\theta} f_1, e^{-i\theta} f_0), \quad u' = \sigma_x u^*. \tag{5.12}$$

For small r the zero-modes tend to a constant (the factor $1/r$ from K_1 is canceled by the factor r from e^{-q}). The large-r asymptotics follows upon an expansion of the integrand around the extremal points $\pm Q$, giving

$$f_n \to (-1)^n \frac{e^{Ky}}{\Delta_0^n} \left(\frac{(K+Q)^n e^{-iQx}}{iKx - Qy} - \frac{(K-Q)^n e^{iQx}}{iKx + Qy} \right). \tag{5.13}$$

[7] We assume there is an even number of vortices in S. If the number of vortices is odd, a zero-energy edge state along the perimeter of S will ensure that the total number of Majorana zero-modes remains even.

[8] This normalization requirement at the vortex core ties the chirality of the Majorana zero-modes to the sign of the vorticity. If we would have chosen -2π vortices the field $q(\boldsymbol{r})$ would tend to $+\frac{1}{2} \ln |r - \boldsymbol{R}_n|$ near a vortex core, and the product $e^{-q} f \propto |\boldsymbol{r} - \boldsymbol{R}_n|^{-1/2} f$ would not have been square integrable.

[9] Details of the solution of the Helmholtz equation are given in Apps. 5.B and 5.C.

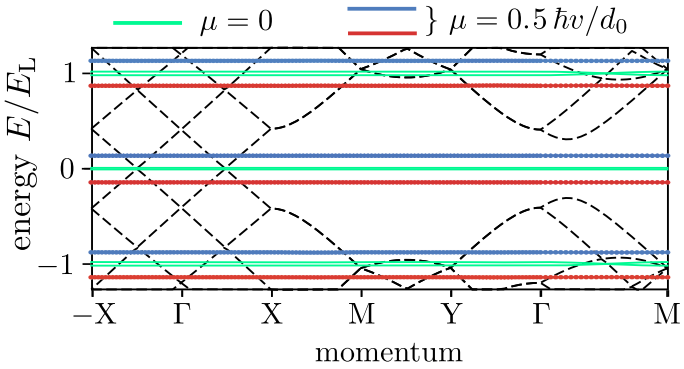

Figure 5.3: Dispersion relation of the topological superconductor, calculated from the model Hamiltonian (5.14) for zero magnetic field (black dashed lines, chemical potential $\mu = 0$) and in the presence of the magnetic vortex lattice (colored flat bands at charge $\pm q_{\rm eff} e$, for two values of μ). For both data sets $K = 2\Delta_0 = 20\,\hbar v/d_0$.

The zero-modes decay as $e^{-Ky} f_n \propto 1/r$ for $r \gg R$, which needs to be regularized for a square-integrable wave function [93, 94][10]. In a chain of vortices (spacing b), the superposition of the solution (5.13) decays exponentially in the direction perpendicular to the chain[9]. The decay length is $\lambda = bK/Q$ or $\lambda = bQ/K$ for a chain oriented along the x-axis or y-axis, respectively.

5.4 Numerical simulation

For a numerical study of the deconfinement transition we represent the topological insulator layer by the low-energy Hamiltonian [95, 96]

$$\begin{aligned} H_0(\boldsymbol{k}) &= (v/a_0)\textstyle\sum_{j=x,y}\sigma_j \sin k_j a_0 + \sigma_z M(k) - \mu, \\ M(k) &= M_0 - (M_1/a_0^2)\textstyle\sum_{j=x,y}(1-\cos k_j a_0), \end{aligned} \tag{5.14}$$

in the basis $\Psi = 2^{-1/2}(\psi_{\uparrow\rm upper} + \psi_{\uparrow\rm lower}, \psi_{\downarrow\rm upper} - \psi_{\downarrow\rm lower})$ of spin-up and spin-down states on the upper and lower surfaces [11]. The atomic lattice

[10] The $1/r$ decay of the deconfined Majorana zero-mode implies a density of states peak which decays slowly $\propto 1/\ln L$ as a function of the system size L. There is a formal similarity here with the zero-modes originating from vacancies in a 2D bipartite lattice [93, 94].

[11] In the basis $\Psi = (\psi_{\uparrow\rm upper}, \psi_{\downarrow\rm upper}, \psi_{\uparrow\rm lower}, \psi_{\downarrow\rm lower})$ the 4×4 Hamiltonian of the topological insulator layer is $H_0 = t_0 \sum_{j=x,y} \tau_z \sigma_j \sin k_j a_0 + \tau_x \sigma_0 M(k) - \mu$,

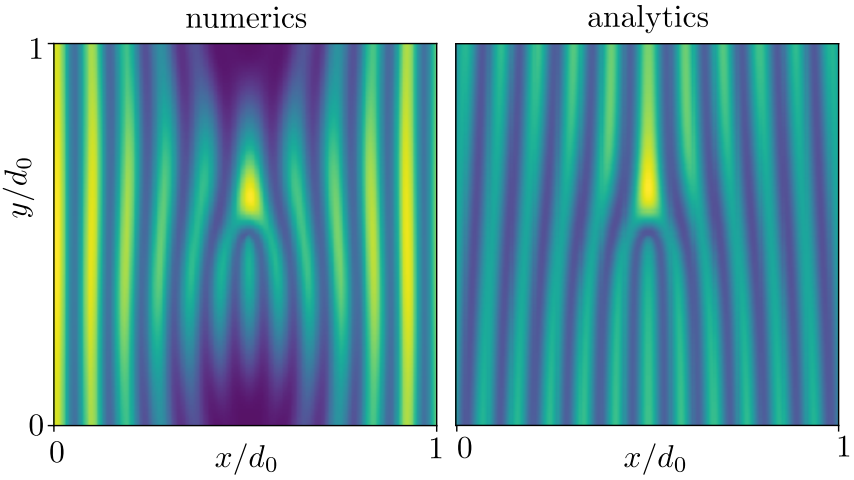

Figure 5.4: Left panel: Numerically calculated intensity profile $|\Psi(x,y)|^2$ of the zeroth Landau level in a vortex lattice with a pair of $h/2e$ vortices at the center of the unit cell ($K = 2\Delta_0 = 40\,\hbar v/d_0$, $\mu = 0$). Right panel: Analytical result from the solution of the Helmholtz equation (5.9) for a single h/e vortex[12].

constant is a_0, the Fermi velocity is v, and μ is the chemical potential. Hybridization of the states on the two surfaces introduces the mass term $M(k)$. We set $M_0 = 0$, to avoid the opening of a gap[2] at $k = 0$, but retain a nonzero $M_1 = 0.2\,a_0 v$ in order to eliminate the fermion doubling at $a_0\boldsymbol{k} = (\pi, \pi)$.

In the corresponding BdG Hamiltonian the electron block $H_0(\boldsymbol{k} - e\boldsymbol{A} + \boldsymbol{K})$ is coupled to the hole block $-H_0(\boldsymbol{k} + e\boldsymbol{A} - \boldsymbol{K})$ by the s-wave pair potential $\Delta_0 e^{i\phi}$, which we take the same for both layers. We assume a strong type-II superconductor, for which we can take a uniform magnetic field B and uniform pair potential amplitude Δ_0. The $+2\pi$ vortices are positioned on a square lattice (lattice constant $d_0 = 302\,a_0$) with two vortices per unit cell.

The spectrum is calculated using the *Kwant* tight-binding code [52][13].

with Pauli matrix τ_z acting on the layer index. A unitary transformation block-diagonalizes the Hamiltonian. One of the 2×2 blocks is given in Eq. (5.14), the other block has M replaced by $-M$.

[12]The comparison between numerics and analytics in Fig. 5.4 involves no adjustable parameters. To compare the same state in the degenerate zeroth Landau level we choose the state with left-right reflection symmetry. There are two of these, the other is compared in App. 5.E.

[13]Details of the method of numerical simulation, with supporting data, are given in

In Fig. 5.3 we show the dispersionless Landau levels, both for chemical potential $\mu = 0$ and for nonzero μ. The zeroth Landau level has energy $E_0 = \pm q_{\text{eff}}\mu$, with $q_{\text{eff}}e$ the charge expectation value. For the model Hamiltonian (5.2) we have[14] $q_{\text{eff}} = Q/K = \sqrt{1 - \Delta_0^2/K^2}$. The numerics at $K = 2\Delta_0$ gives a value 0.85, within 2% of $\sqrt{3/4} = 0.866$. The first Landau level is expected at energy $E_1 = E_{\text{L}} \pm q_{\text{eff}}\mu$ with $E_{\text{L}} = \sqrt{4\pi q_{\text{eff}}}\,\hbar v/d_0$, again in very good agreement with the numerics. Notice that the flatness of the dispersion persists at nonzero μ — even though the topological protection due to chiral symmetry[15] is only rigorously effective at $\mu = 0$.

In Fig. 5.4 we compare numerical and analytical results for the case that the two $h/2e$ vortices are both placed at the center of the unit cell. The agreement is quite satisfactory, given the different geometries (a vortex lattice in the numerics, a single h/e vortex in the analytics).

5.5 Striped local density of states

The striped pattern of the Majorana Landau level is observable by tunneling spectroscopy, which measures the local density of states

$$\rho(\boldsymbol{r}) = \textstyle\sum_{\boldsymbol{k}} \big[|\psi_e(\boldsymbol{r})|^2 f'(E_0 - eV) + |\psi_h(\boldsymbol{r})|^2 f'(E_0 + eV)\big], \qquad (5.15)$$

averaged over the 2D magnetic Brillouin zone, $\sum_{\boldsymbol{k}} = (2\pi)^{-2} \int dk_x dk_y$, weighted by the derivative of the Fermi function. If E_0 is much larger than temperature, the sign of the bias voltage V determines whether the electron component ψ_e or the hole component ψ_h contributes, so these can be measured separately.

As shown in Fig. 5.5, the oscillations are most pronounced for the hole component when $\mu > 0$ (or equivalently the electron component when $\mu < 0$). This asymmetry in the tunneling current for $V = \pm E_0$ is an additional experimental signature of the effect.

App. 5.A.

[14] The renormalized charge q_{eff} in the Majorana Landau level is calculated in App. 5.D. That calculation also gives the renormalized Fermi velocity $v_{\text{eff}} = \sqrt{v_x v_y} = \sqrt{q_{\text{eff}}}\, v$ that appears in the Landau level energy E_{L}.

[15] The chiral symmetry at $\mu = 0$ is broken by the mass term $M(k)$ in the Hamiltonian (5.14). This residual chiral symmetry breaking is visible in Fig. 5.3 as a very small splitting of the $\mu = 0$ Landau levels (green flat bands).

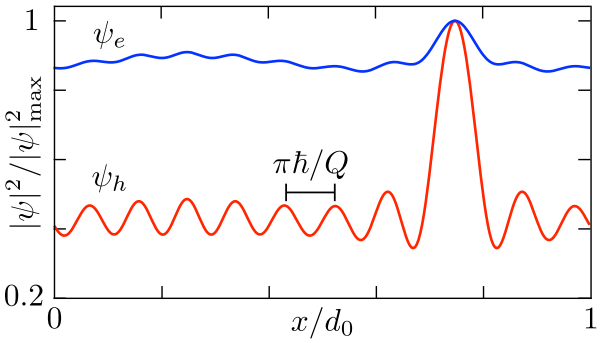

Figure 5.5: Electron and hole contributions to the local density of states in the zeroth Landau level, along a line parallel to the x-axis which passes close through a vortex core at $x = y = 3d_0/4$. The curves are plots of $\sum_{\boldsymbol{k}} |\psi_{e,h}(x,y)|^2$ normalized to unit peak height at the vortex core. The parameters are $K = 2\Delta_0 = 40\,\hbar v/d_0$, $\mu = 0.5\,\hbar v/d_0$. The expected oscillation period of $\pi\hbar/Q = 0.091\,d_0$ is indicated.

5.6 Conclusion

Concerning the experimental feasibility, we note that the gap closing due to a superflow has already been observed [15], and Majorana vortex lattices in a perpendicular field of 250 mT have been detected by scanning probes in several experiments [97] — so by combining these two ingredients the Majorana Landau level should become accessible. The main additional requirement is that the Fermi level is sufficiently small, $\mu < \min(E_{\rm L}, \Delta_0) \simeq 1\,\text{meV}$ at 250 mT, to benefit from the protection afforded by chiral symmetry. Experiments [98] where μ was tuned through the charge neutrality point give confidence that this is feasible.

The striped interference pattern in the local density of states, with wave number $Q = \sqrt{K^2 - (\Delta_0/\hbar v)^2}$ ($\simeq 2\pi/0.2\,\mu$m for $K = 2\Delta_0/\hbar v$ at typical values of $\Delta_0 = 1\,\text{meV}$ and $v = 10^5\,\text{m/s}$) should be accessible by scanning probe spectroscopy. Surface defects would themselves introduce Friedel oscillations in the density of states, but the highly directional pattern that is the hallmark of the Majorana Landau level would stand out.

The Majorana Landau level provides a realization of a flat band with extended wave functions, in which interaction effects are expected to be enhanced due to the quenching of kinetic energy. Interacting Majorana fermions in a Fu-Kane superconductor have been studied by placing vortices in close proximity inside a quantum dot [99]. The deconfinement

transition provides a means to open up the system and obtain a fully 2D flat band with widely separated vortices. An intriguing topic for further research is to investigate how the exchange of vortices operates on this highly degenerate manifold.

Appendices

5.A Details of the numerical simulation

5.A.1 Tight-binding model

The model Hamiltonian we consider is

$$\mathcal{H}_\pm = \begin{pmatrix} H_\pm(\boldsymbol{k} - e\boldsymbol{A} + \boldsymbol{K}) & \Delta_0 e^{i\phi} \\ \Delta_0 e^{-i\phi} & -H_\pm(\boldsymbol{k} + e\boldsymbol{A} - \boldsymbol{K}) \end{pmatrix}, \tag{5.16a}$$

$$H_\pm(\boldsymbol{k}) = \pm(v/a_0)\sigma_x \sin a_0 k_x \pm (v/a_0)\sigma_y \sin a_0 k_y \pm \sigma_z M(k) - \mu, \tag{5.16b}$$

$$M(k) = M_0 - (M_1/a_0^2)(2 - \cos a_0 k_x - \cos a_0 k_y). \tag{5.16c}$$

The Hamiltonian acts on a spinor with the four components

$$\Psi_\pm(\boldsymbol{k}) = \frac{1}{\sqrt{2}} \begin{pmatrix} [\psi_{\uparrow\text{upper}} \pm \psi_{\uparrow\text{lower}}](\boldsymbol{k}) \\ [\psi_{\downarrow\text{upper}} \mp \psi_{\downarrow\text{lower}}](\boldsymbol{k}) \\ -i[\psi_{\downarrow\text{upper}} \pm \psi_{\downarrow\text{lower}}]^*(-\boldsymbol{k}) \\ i[\psi_{\uparrow\text{upper}} \mp \psi_{\uparrow\text{lower}}]^*(-\boldsymbol{k}) \end{pmatrix}, \tag{5.17}$$

for spin-up and spin-down electrons on the upper and lower surface of the topological insulator layer. The first two elements of the spinor Ψ refer to electrons and the last two elements to holes. These are coupled by the s-wave pair potential Δ_0, which we take the same on both surfaces. The particle-hole symmetry relation is

$$\mathcal{H}_\pm(\boldsymbol{k}) = -\sigma_x \nu_y \mathcal{H}_\mp^*(-\boldsymbol{k}) \sigma_x \nu_y, \tag{5.18}$$

where the σ_α and τ_α Pauli matrices act on the spin and electron-hole degree of freedom, respectively.

For the mass term $M(k)$ we take $M_0 = 0$, $M_1 = 0.2\, a_0 v$, such that H_0 has a single gapless Dirac point at $\boldsymbol{k} = 0$. Near this Dirac point the upper and lower surface are uncoupled, so the eigenstate can equivalently be written in the single-surface basis $(\psi_\uparrow, \psi_\downarrow, -i\psi_\downarrow^*, i\psi_\uparrow^*)$. The effect of a gap opening due to a nonzero M_0 is examined at the end of this Appendix.

The Hamiltonian is discretized on a square lattice (lattice constant a_0) with nearest neighbor hopping (hopping energy v/a_0). The magnetic field B is uniform in the z-direction, vector potential $\boldsymbol{A} = -By\hat{x}$. The superflow momentum is $\boldsymbol{K} = K\hat{x}$. The amplitude Δ_0 of the pair potential is taken as a constant, the phase $\phi(x, y)$ winds by 2π around each vortex.

We take a square vortex lattice, with lattice constant $d_0 = Na_0$. The flux through each magnetic unit cell is h/e, so it contains a pair of $h/2e$ vortices. The integer N determines the magnetic field via $B = (Na_0)^{-2}h/e$. The vortices are placed on the diagonal of the magnetic unit cell, at the positions $(x, y) = (Na_0/4)(1, 1)$ and $(Na_0/4)(3, 3)$. By taking for N twice an odd integer, we ensure that the singularity in the phase field at the vortex core does not coincide with a lattice point. The phase field is discretized along the lines set out in App. B of Ref. 57. The eigenvalues and eigenfunctions of H are calculated using the *Kwant* tight-binding code [52].

5.A.2 Additional numerical results

Here we collect some additional results to those shown in the main text. In the confined phase $vK < \Delta_0$ we show in Fig. 5.6 the anisotropic decay rates of the Majorana zero-modes bound to a vortex core, as in the left panel of Fig. 5.2. The localization length $(\Delta_0/v - K)^{-1}$ of the zero-modes diverges at the transition.

Fig. 5.7 shows how at the deconfinement transition the quasi-continuum of excited states in the vortex core is reorganized into a sequence of Landau levels. The critical exponents for the gap closing are different on the two sides of the transition. In the confined phase the gap to the first excited state scales with the inverse localization length, so $\propto (\Delta_0/v - K)^1$. In the deconfined phase the gap scales with the Landau level separation $E_{\rm L} \propto \sqrt{q_{\rm eff}}$, so $\propto (K - \Delta_0/v)^{1/4}$.

In the deconfined phase $vK > \Delta_0$ we show in Fig. 5.8 the Landau levels in the vortex lattice (complementing Fig. 5.3). Fig. 5.9 shows the local density of states in the zeroth Landau level. This shows the variation over the entire unit cell of the vortex lattice, to complement the line cut through a vortex core shown in Fig. 5.5 of the main text.

5.A.3 Effect of overlap of top and bottom surface states

A nonzero mass term $\pm M_0\sigma_z\nu_z$ in the Hamiltonian (5.16) opens up a hybridization gap in the Dirac cone. Since the Majorana Landau level is

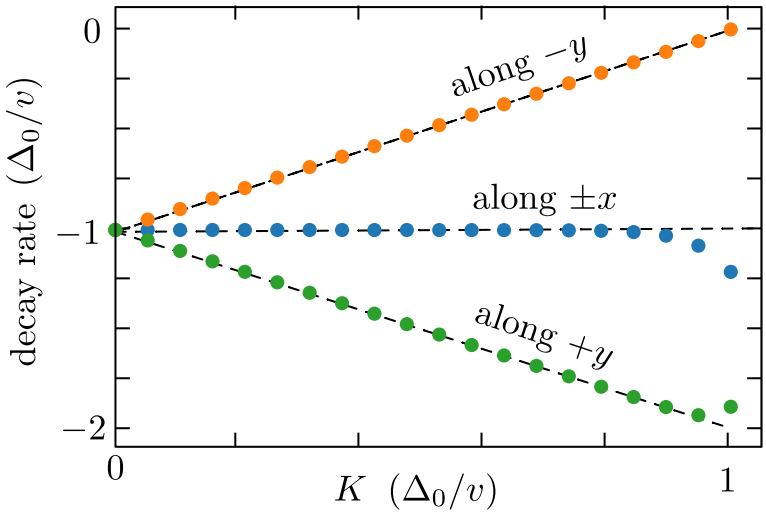

Figure 5.6: Decay rate of the Majorana mode confined to a vortex core. The data from the numerical simulation (colored points, $\Delta_0 = 20\, v/d_0$) closely follows the analytical prediction $|\Psi| \propto e^{-Ky} e^{-(\Delta_0/v)r}$ (dashed lines).

an eigenstate of the chirality operator $\Lambda = \sigma_z \nu_z$, the effect of this term is to displace the flat band away from $E = 0$ by an amount M_0. In Fig. 5.10 we show numerical results that demonstrate this. Provided that M_0 remains smaller than the Landau level separation E_L, we do not expect the overlap of top and bottom surface states to prevent the detection of the Majorana Landau level. This is helpful because the overlap will favor a strong proximity effect on both surfaces.

5.B Solution of the Helmholtz equation for the Majorana Landau level

The general solution of the 2D Helmholtz equation $\nabla^2 f = \Delta_0^2 f$ that governs the Majorana Landau level is a superposition of waves $e^{ipx \pm y\sqrt{p^2+\Delta_0^2}}$. Which superposition we need is determined by the requirement that $e^{-Ky-q(\boldsymbol{r})} f(x,y)$ is square integrable in the x–y plane, with $K > \Delta_0 > 0$. We denote $Q = \sqrt{K^2 - \Delta_0^2}$. For ease of notation we will set $\Delta_0 \equiv 1$ in this appendix.

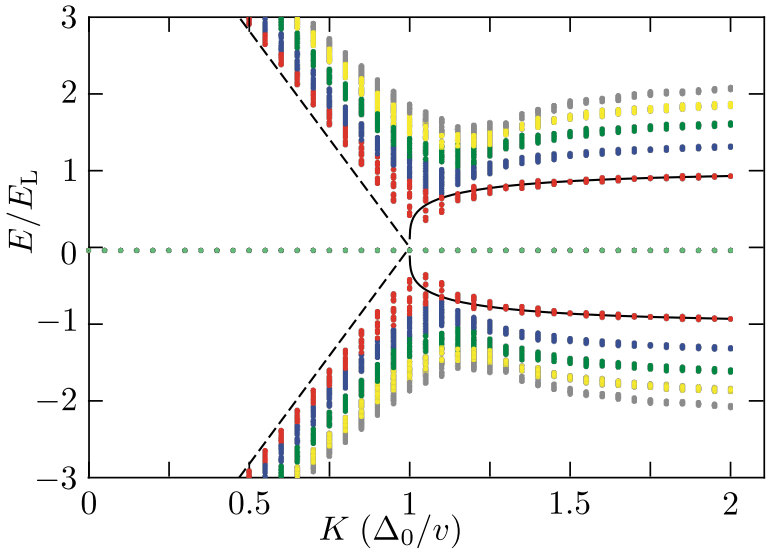

Figure 5.7: Excitation spectrum as a function of the superflow momentum (parameters as in Fig. 5.2). For $K < \Delta_0/v$ the states are confined to vortex cores and form a quasi-continuum, for $K > \Delta_0/v$ they are extended states arranged into a sequence of Landau levels (distinguished by different colors, the Majorana zero-modes are the light-green dots). The deconfinement transition at $K = \Delta_0/v$ is accompanied by a near closing of the gap to the first excited state. The dashed curves show the expected gap scaling $\propto (\Delta_0/v - K)$ and $\propto (K - \Delta_0/v)^{1/4}$ on the two sides of the transition.

We construct a class of solutions for the case

$$q(\boldsymbol{r}) = \epsilon r - \mathcal{N} \ln \min(r, 1), \quad \mathcal{N} = 1, 2, \ldots, \tag{5.19}$$

corresponding to $2\mathcal{N}$ vortices, each of vorticity $+2\pi$, at the origin. The positive infinitesimal $\epsilon > 0$ is introduced to regularize integrals at $r \to \infty$. The restriction to an even number of overlapping vortices means that the branch cut which connects vortices pairwise can be ignored. (We have not succeeded in finding an analytical solution that incorporates the branch cut, but of course in the numerics this is not a limitation.)

The superposition of elementary solutions $e^{ipx \pm y\sqrt{p^2+1}}$ that cancels the

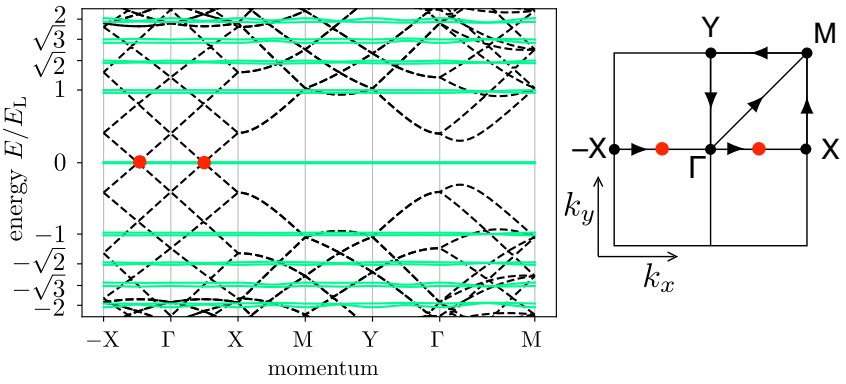

Figure 5.8: Dispersion relation in zero magnetic field (black dashed lines) and in the presence of the magnetic vortex lattice (green solid lines, the right panel shows the magnetic Brillouin zone). Both band structures are for $\mu = 0$, and the same parameters as in Fig. 5.3. The red dots indicate the Dirac points at $\boldsymbol{k} = (\pm Q, 0)$ in zero magnetic field. The Landau levels are at $\pm\sqrt{n}\,E_L$, $n = 0, 1, 2$, with $E_L = \sqrt{4\pi q_{\text{eff}}}\,\hbar v/d_0$.

exponential growth factor e^{-Ky} has the general form

$$f = \begin{cases} \int_{|p|>Q} dp\, C(p) e^{ipx+y\sqrt{p^2+1}} & \text{if } y < 0, \\ -\int_{|p|<Q} dp\, C(p) e^{ipx+y\sqrt{p^2+1}} & \\ \quad + \int dp\, D(p) e^{ipx-y\sqrt{p^2+1}} & \text{if } y > 0. \end{cases} \tag{5.20}$$

(We can use the symbol C twice without loss of generality because the integration ranges do not overlap.)

The solution should be continuously differentiable at $r \neq 0$, which is satisfied if $f(x, y)$ and $\partial_y f(x, y)$ are continuous functions of y at $y = 0$, $x \neq 0$. The continuity requirement is that the Fourier transform $\int \cdots e^{ipx} dp$ of $C(p)$ equals the Fourier transform of $D(p)$ for $x \neq 0$, which means that $C(p)$ and $D(p)$ differ by a polynomial $L(p)$ of p. [Recall that the Fourier transform of a polynomial is given by derivatives of $\delta(x)$.] Similarly, the requirement of a continuous derivative is that $\sqrt{p^2+1}\,C(p)$ and $-\sqrt{p^2+1}\,D(p)$ differ by a polynomial $T(p)$. The unique solution of these

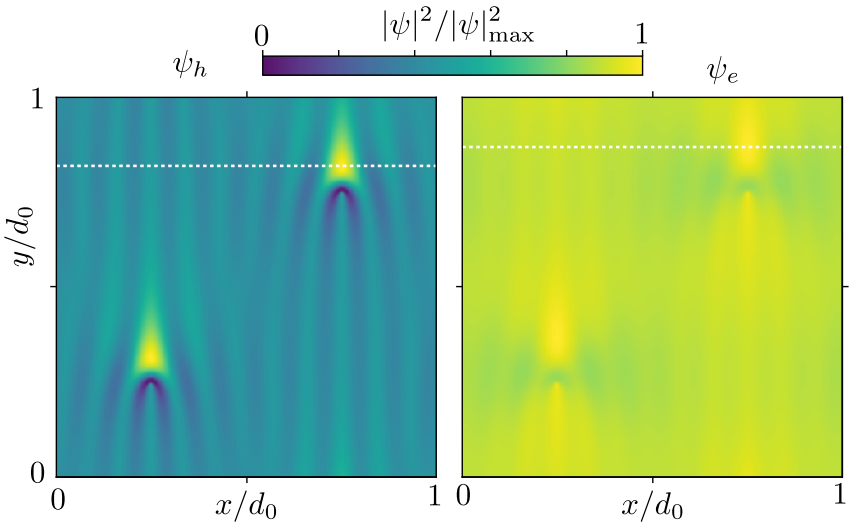

Figure 5.9: Local density of states in the unit cell of the vortex lattice, at the energy $E_0 > 0$ of the zeroth Landau level pushed above the Fermi level by a chemical potential $\mu > 0$. The color scale plot shows $\sum_{\boldsymbol{k}} |\psi_{e,h}(x,y)|^2$, summed over the magnetic Brillouin zone, normalized to unit maximum value. The white dotted line indicates the cut shown in Fig. 5.5 of the main text, at the same parameters. The electron contribution to the local density of states (right panel) and the hole contribution (left panel) can be measured separately by tunnel spectroscopy at voltages $V = E_0$ and $V = -E_0$, respectively.

two requirements is

$$\begin{aligned} C(p) &= \frac{\frac{1}{2}T(p)}{\sqrt{p^2+1}} - \tfrac{1}{2}L(p), \\ D(p) &= \frac{\frac{1}{2}T(p)}{\sqrt{p^2+1}} + \tfrac{1}{2}L(p). \end{aligned} \tag{5.21}$$

We are free to choose a convenient basis for the polynomials $T(p)$ and $L(p)$, we will choose one for which the integral over $D(p)$ has a closed-form expression. The basis polynomials $T_n(p)$ and $L_n(p)$, $n = 0, 1, 2, \ldots$ are

$$\begin{aligned} T_n(p) &= \left(p + \sqrt{p^2+1}\right)^n + \left(p - \sqrt{p^2+1}\right)^n, \\ L_n(p) &= \frac{\left(p + \sqrt{p^2+1}\right)^n}{\sqrt{p^2+1}} - \frac{\left(p - \sqrt{p^2+1}\right)^n}{\sqrt{p^2+1}}. \end{aligned} \tag{5.22}$$

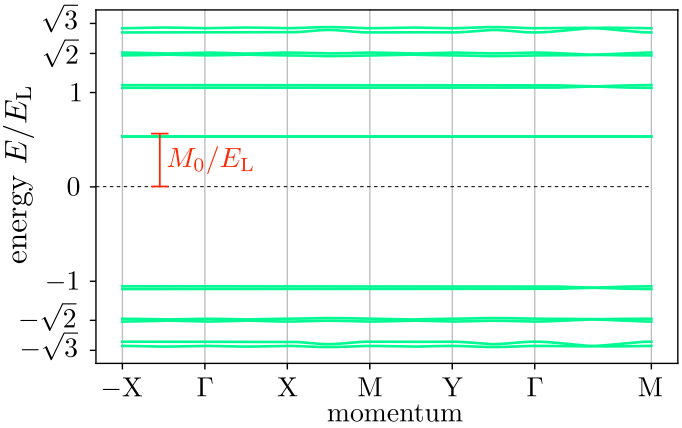

Figure 5.10: Same as Fig. 5.8, but now for a nonzero mass term M_0, to show how the hybridization gap shifts the zeroth Landau level away from $E = 0$. The plot shows the spectrum of the Hamiltonian $\mathcal{H}_+$ in Eq. (5.16), the spectrum of $\mathcal{H}_-$ has the zeroth Landau level shifted to $-M_0$ (so that the full spectrum is particle-hole symmetric). The parameters are $K = 2\Delta_0 = 20\,\hbar v/d_0$, $d_0 = 102\,a_0$, $M_0 = 0.02/a_0$, $M_1 = 0.2\,a_0$.

This choice of basis is related to a basis of Chebyshev polynomials $\mathcal{T}_n$, via the identities

$$\begin{aligned} T_n(p) &= 2(-i)^n \mathcal{T}_n(ip), \\ L_n(p) &= 2(-i)^{n-1} \sum_{m=0}^{n-1} \mathcal{T}_{2m-n+1}(ip). \end{aligned} \tag{5.23}$$

Note that

$$T_{-n}(p) = (-1)^n T_n(p), \quad L_{-n}(p) = -(-1)^n L_{-n}(p). \tag{5.24}$$

A complete basis for the pairs of polynomials $T(p), L(p)$ is therefore given by the two sets $\{T_n, L_n\} \cup \{T_n, -L_n\}$ with $n = 0, 1, 2, \ldots$, or equivalently by the single set $\{T_n, L_n\}$ with $n = 0, \pm 1, \pm 2, \ldots$. The corresponding basis of the functions $C(p)$ and $D(p)$ in Eq. (5.21) is

$$\begin{aligned} C_n(p) &= \frac{\frac{1}{2}T_n(p)}{\sqrt{p^2+1}} - \tfrac{1}{2}L_n(p) = \frac{\left(p - \sqrt{p^2+1}\right)^n}{\sqrt{p^2+1}}, \\ D_n(p) &= \frac{\frac{1}{2}T_n(p)}{\sqrt{p^2+1}} + \tfrac{1}{2}L_n(p) = \frac{\left(p + \sqrt{p^2+1}\right)^n}{\sqrt{p^2+1}}, \end{aligned} \tag{5.25}$$

with $n = 0, \pm 1, \pm 2, \ldots$.

We next use the Bessel function identities[16]

$$\mathrm{K}_n(r) = \begin{cases} \frac{1}{2i^n} e^{in\theta} \int_{-\infty}^{\infty} dp\, D_n(p) e^{ipx - y\sqrt{p^2+1}} & \text{if } y \geq 0, \\ \frac{1}{2i^n} e^{in\theta} \int_{-\infty}^{\infty} dp\, C_n(p) e^{ipx + y\sqrt{p^2+1}} & \text{if } y \leq 0, \end{cases} \tag{5.26}$$

where $r = \sqrt{x^2+y^2}$ and $e^{i\theta} = (x+iy)/r$, to write the solution (5.20) in the form

$$\begin{aligned} f_n(x,y) = &- \int_{-Q}^{Q} dp\, \frac{\left(p - \sqrt{p^2+1}\right)^n}{\sqrt{p^2+1}} e^{ixp + y\sqrt{p^2+1}} \\ &+ 2i^n e^{-in\theta} \mathrm{K}_n(r), \end{aligned} \tag{5.27}$$

which is Eq. (5.11) in the main text (upon restoring the units of Δ_0).

The function f_n is the first component of the spinor $\tilde{u} = (f, g)$, the second component is

$$g_n = (i\partial_x - \partial_y) f_n = f_{n-1}. \tag{5.28}$$

We now obtained an infinite countable set of solutions $\tilde{u}_n = (f_n, f_{n-1})$, $n = 0, \pm 1, \pm 2, \ldots$ of the Helmholtz equation, such that $e^{-Ky} e^{-\epsilon r} \tilde{u}_n$ is square integrable at infinity. The condition that $r^{\mathcal{N}} \tilde{u}$ is square integrable at the origin (containing $2\mathcal{N}$ overlapping vortices) selects a finite subset. For $r \to 0$ we have $f_n \simeq r^{-|n|}$ if $n \neq 0$ and $f_0 \simeq \ln r$. Normalizability requires that both $|n| \leq \mathcal{N}$ and $|n-1| \leq \mathcal{N}$, hence there are $2\mathcal{N}$ allowed values of $n \in \{-\mathcal{N}+1, -\mathcal{N}+2, \ldots \mathcal{N}-1, \mathcal{N}\}$.

All of this was for zero-modes $\Psi = (f, g, 0, 0)$ of positive chirality, in a lattice of $+2\pi$ vortices. Alternatively, we can consider zero-modes $\Psi = (0, 0, f, g)$ of negative chirality in a lattice of -2π vortices. The differential equations for f and g remain the same, but now the exponential factor that needs to be canceled is e^{Ky} rather than e^{-Ky}. The sign change gives the negative chirality solution

$$\begin{aligned} f_n(x,y) = &- \int_{-Q}^{Q} dp\, \frac{\left(p - \sqrt{p^2+1}\right)^n}{\sqrt{p^2+1}} e^{ixp - y\sqrt{p^2+1}} \\ &+ 2i^n e^{in\theta} \mathrm{K}_n(r), \end{aligned} \tag{5.29a}$$

$$g_n = (i\partial_x - \partial_y) f_n = -f_{n+1}. \tag{5.29b}$$

The $2\mathcal{N}$ zero-modes are now labeled by the index $n \in \{-\mathcal{N}, -\mathcal{N}+1, \ldots \mathcal{N}-2, \mathcal{N}-1\}$.

[16] The identities (5.26) follow from the integral representation $\mathrm{K}_n(r) = \frac{1}{2}(r/2)^n \int_0^\infty t^{-n-1} \exp(-t - \frac{1}{4}r^2/t)\, dt$, upon the substitution $p = \frac{1}{2}(t - 1/t)$.

5.C Chain of vortices

The regularization at infinity by the ϵ term in Eq. (5.19) is not needed if we have a periodic lattice of vortices. We demonstrate this by considering a linear chain of vortices at positions $\boldsymbol{R}_\ell$, spaced by b at an angle $\vartheta \in [0, \pi/2]$ with the x-axis. We take a linear superposition of the solutions $e^{-Ky} f_n(\boldsymbol{r} - \boldsymbol{R}_\ell)$ from Eq. (5.27), with complex weights,

$$F_n(\boldsymbol{r}) = \sum_{\ell=-\infty}^{\infty} e^{i\ell\kappa} e^{\ell K b \sin\vartheta} e^{-Ky} f_n(\boldsymbol{r} - \boldsymbol{R}_\ell). \tag{5.30}$$

We do not include the envelope e^{-q}, because it tends to unity for large r if we set $\epsilon \equiv 0$. The Bloch phase κ is arbitrary.

We substitute the large-r expansion (5.13),

$$F_n \to (-1)^n \sum_{\ell=-\infty}^{\infty} e^{i\ell\kappa} \Bigg(\frac{(K+Q)^n e^{-iQ(x-\ell b\cos\vartheta)}}{iK(x-\ell b\cos\vartheta) - Q(y-\ell b\sin\vartheta)} - \frac{(K-Q)^n e^{iQ(x-\ell b\cos\vartheta)}}{iK(x-\ell b\cos\vartheta) + Q(y-\ell b\sin\vartheta)} \Bigg). \tag{5.31}$$

We seek the decay of F_n in the direction perpendicular to the chain, so for large $|\rho|$ when $(x, y) = (-\rho\sin\vartheta, \rho\cos\vartheta)$.

We thus need to evaluate an infinite sum of the form[17]

$$S(\alpha, z) = \sum_{\ell=-\infty}^{\infty} \frac{e^{i\ell\alpha}}{z+\ell}, \quad \alpha \in (0, 2\pi), \quad z \in \mathbb{C}\backslash\mathbb{Z}, \tag{5.32a}$$

$$S(\alpha, z) = \frac{2\pi i}{e^{i\alpha z} - e^{i(\alpha-2\pi)z}}. \tag{5.32b}$$

In the limit $|\mathrm{Im}\, z| \to \infty$ this tends to

$$S(\alpha, z) \to \begin{cases} -2\pi i e^{-(2\pi-\alpha)\mathrm{Im}\, z} & \text{if } \mathrm{Im}\, z \to \infty, \\ 2\pi i e^{\alpha \mathrm{Im}\, z} & \text{if } \mathrm{Im}\, z \to -\infty. \end{cases} \tag{5.33}$$

Substitution of Eq. (5.32) into Eq. (5.31) gives, for $x = -\rho\sin\theta$, $y = \rho\cos\theta$,

$$F_n \to \frac{(-1)^n (K+Q)^n e^{iQ\rho\sin\vartheta}}{Qb\sin\vartheta - iKb\cos\vartheta} S(\alpha_+, z_-) + \frac{(-1)^n (K-Q)^n e^{-iQ\rho\sin\vartheta}}{Qb\sin\vartheta + iKb\cos\vartheta} S(\alpha_-, z_+), \tag{5.34}$$

[17] For a derivation of Eq. (5.32b), and its relation to the Lerch zeta function, see https://mathoverflow.net/q/379157/11260

where we abbreviated

$$\begin{aligned} \alpha_\pm &= \kappa \pm Qb\cos\vartheta \mod 2\pi, \\ z_\pm &= \frac{\rho}{b}\frac{\frac{1}{2}\sin 2\vartheta \pm iKQ}{K^2-\sin^2\vartheta}. \end{aligned} \tag{5.35}$$

Provided that $\alpha_\pm \neq 0 \mod 2\pi$, the decay is exponential: $|F_n| \simeq e^{-c|\rho|/\lambda}$, with (reinserting the units of Δ_0)

$$\lambda = b\frac{K^2-\Delta_0^2\sin^2\vartheta}{K\sqrt{K^2-\Delta_0^2}} \tag{5.36}$$

and c a coefficient of order unity that depends on the sign of ρ,

$$c = \begin{cases} \min(\alpha_+, 2\pi-\alpha_-) & \text{if } \rho>0, \\ \min(\alpha_-, 2\pi-\alpha_+) & \text{if } \rho<0. \end{cases} \tag{5.37}$$

For a chain oriented along the x-axis or y-axis we have λ equal to bK/Q or bQ/K, respectively.

5.D Renormalized charge in the Majorana Landau level

The charge expectation value of the deconfined zero-mode can be calculated by means of the block diagonalization approach of Ref. 57. Starting from the BdG Hamiltonian (5.2) we first make the gauge transformation $H \mapsto U^\dagger H U$ with $U = \begin{pmatrix} e^{i\phi} & 0 \\ 0 & 1 \end{pmatrix}$, resulting in

$$\begin{aligned} H &= \begin{pmatrix} (\boldsymbol{k}+\boldsymbol{a}+\boldsymbol{q})\cdot\boldsymbol{\sigma}-\mu & \Delta_0 \\ \Delta_0 & -(\boldsymbol{k}+\boldsymbol{a}-\boldsymbol{q})\cdot\boldsymbol{\sigma}+\mu \end{pmatrix}, \\ \boldsymbol{a} &= \tfrac{1}{2}\nabla\phi, \quad \boldsymbol{q} = \tfrac{1}{2}\nabla\phi - e\boldsymbol{A} + K\hat{x}. \end{aligned} \tag{5.38}$$

We have included the chemical potential μ.

For $K > \Delta_0$ in zero magnetic field there are gapless Dirac points at $\boldsymbol{k} = (k_x, k_y) = (\tilde{K}, 0)$ with

$$\tilde{K} = \pm\kappa K, \quad \kappa = \sqrt{1-\Delta_0^2/K^2}. \tag{5.39}$$

To focus on the effect of a magnetic field on states near $\tilde{K}$ we set $k_x = \tilde{K} + \delta k_x$ and consider δk_x small.

A unitary transformation $H \mapsto V^\dagger H V$ with

$$V = \begin{pmatrix} \sigma_0 \cos(\alpha/2) & \sigma_x \sin(\alpha/2) \\ -\sigma_x \sin(\alpha/2) & \sigma_0 \cos(\alpha/2) \end{pmatrix}, \qquad (5.40)$$
$$\tan\alpha = -\Delta_0/\tilde{K}, \;\; \cos\alpha = -(1+\Delta_0^2/\tilde{K}^2)^{-1/2} = -\kappa,$$

approximately block-diagonalizes the Hamiltonian; the 2×2 off-diagonal blocks contribute to the spectrum in second order in δk_x, $\boldsymbol{a}$, $\boldsymbol{q}$, and μ. The 2×2 block along the diagonal that describes the hole-like states near $\boldsymbol{k} = (\kappa K, 0)$ is given by

$$H_+ = \kappa\mu - (\kappa\delta k_x + \kappa a_x - q_x)\sigma_x + (k_y + a_y - \kappa q_y)\sigma_y, \qquad (5.41)$$

while the electron-like states near $\boldsymbol{k} = (-\kappa K, 0)$ are described by

$$H_- = -\kappa\mu + (\kappa\delta k_x + \kappa a_x + q_x)\sigma_x - (k_y + a_y + \kappa q_y)\sigma_y. \qquad (5.42)$$

The block diagonalization removes any interference between the electron and hole blocks, so this approximation cannot describe the striped density of states of Fig. 5.2 — for that we need the Helmholtz equation considered in the main text. Because the charge operator $\hat{Q} = -e\partial H_\pm/\partial\mu = \mp\kappa e$ commutes with $H_\pm$, the expectation value is given simply by

$$\langle\hat{Q}\rangle = \mp\kappa e \Rightarrow q_{\text{eff}} = \kappa. \qquad (5.43)$$

The Fermi velocity in the x-direction is renormalized by the same factor, $v_x = \kappa v$, while v_y is unaffected. This affects the Landau level energy $E_{\text{L}} = \sqrt{4\pi}\,\hbar v_{\text{eff}}/d_0$ of the anisotropic Dirac cone, via $v_{\text{eff}} = \sqrt{v_x v_y} = \sqrt{\kappa} v$.

5.E Comparison of numerics and analytics

In order to compare the analytic solution (5.11) of the Helmholtz equation with the numerical results from the tight-binding Hamiltonian (5.14) we proceed as follows. For the analytic solution we take a single pair of vortices located at $\boldsymbol{r} = 0$, in a uniform magnetic field with total flux h/e in a large disc centered at the origin. There are then two independent zero-modes u, u' given by Eq. (5.12) with $q(r) = -\ln r$.

For the numerical calculation we consider an infinite lattice of vortices, with pairs of vortices positioned at points $\boldsymbol{R_n} = d_0\boldsymbol{n}$, $\boldsymbol{n} \in \mathbb{Z}^2$, in a uniform magnetic field $B = (h/e)d_0^{-2}$, vector potential $\boldsymbol{A} = -B(y, 0)$.

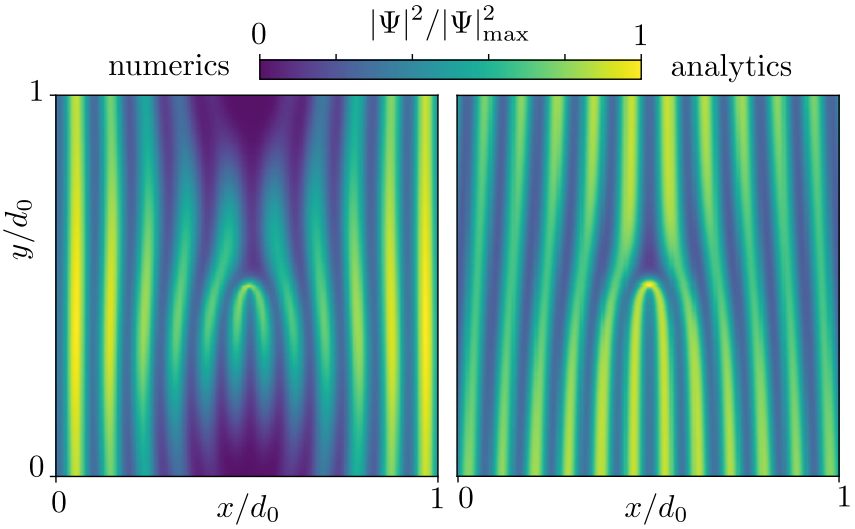

Figure 5.11: Comparison between numerical and analytical intensity profiles $|\Psi(x,y)|^2$, normalized to unit maximal value, for one of the two reflection-symmetric states in the zeroth Landau level. The parameter values are the same as in Fig. 5.4, which compared the other state.

The Hamiltonian commutes with the magnetic translation operator

$$\begin{aligned} \mathcal{T}_{\boldsymbol{n}} &= \begin{pmatrix} e^{ihn_y x/d_0} & 0 \\ 0 & e^{-ihn_y x/d_0} \end{pmatrix} T_{\boldsymbol{n}}\,, \\ T_{\boldsymbol{n}} \boldsymbol{r} T_{\boldsymbol{n}}^\dagger &= \boldsymbol{r} + d_0 \boldsymbol{n}\,. \end{aligned} \tag{5.44}$$

(The 2×2 matrix acts on the electron-hole degree of freedom.) The eigenvalue $e^{i\boldsymbol{k}\cdot\boldsymbol{n}}$ of the eigenstates defines the magnetic momentum $\boldsymbol{k} \in [0, 2\pi)^2$. At each value of $\boldsymbol{k}$ there are two independent zero-modes.

To make sure we are comparing the same state in the degenerate manifold we consider the operator product

$$\mathcal{P}_x = \begin{pmatrix} 0 & e^{\frac{1}{2}i\phi(\boldsymbol{r})} \\ e^{-\frac{1}{2}i\phi(\boldsymbol{r})} & 0 \end{pmatrix} \sigma_x P_x \begin{pmatrix} e^{-\frac{1}{2}i\phi(\boldsymbol{r})} & 0 \\ 0 & e^{\frac{1}{2}i\phi(\boldsymbol{r})} \end{pmatrix}, \tag{5.45}$$

with eigenvalues ± 1, which is a symmetry respected both by the analytic and by the numerical calculation. The operator P_x is the mirror symmetry operator in the x-direction,

$$P_x x P_x^\dagger = -x\,, \quad P_x y P_x^\dagger = y\,. \tag{5.46}$$

The magnetic momentum transforms under $\mathcal{P}_x$ as $k_x \mapsto -k_x$, $k_y \mapsto k_y$.

For the comparison we set $\boldsymbol{k} = 0$, which is invariant under the action of $\mathcal{P}_x$. Then we can take the two zero-modes obtained numerically to be eigenstates of $\mathcal{P}_x$, and compare them with the corresponding eigenstates obtained analytically. Those are

$$u_{\pm}(\boldsymbol{r}) = u(\boldsymbol{r}) \pm u'(\boldsymbol{r})\,, \tag{5.47}$$

which, in view of the fact that

$$f_n(-x, y) = f_n^*(x, y) \tag{5.48}$$

are eigenfunctions of $\mathcal{P}_x$ with eigenvalues ± 1. Figs. 5.4 and 5.11 compare the modulus squared of the $+1$ and -1 eigenstates of $\mathcal{P}_x$ respectively, with quite satisfactory correspondence.

6 Generalized eigenproblem without fermion doubling for Dirac fermions on a lattice

6.1 Introduction

Three-dimensional topological insulators are Nature's way of working around the Nielsen-Ninomiya no-go theorem [100], which forbids the existence of a single species of massless Dirac fermions on a lattice. The fermion doubling required by the theorem is present in a topological insulator slab, but the two species of Dirac fermions are spatially separated on opposite surfaces [101, 102]. On each surface the two-dimensional (2D) Dirac Hamiltonian

$$H_{\rm D} = \hbar v_{\rm F} \boldsymbol{k} \cdot \boldsymbol{\sigma} = -i\hbar v_{\rm F} \left(\sigma_x \frac{\partial}{\partial x} + \sigma_y \frac{\partial}{\partial y} \right) \tag{6.1}$$

emerges as the effective low-energy Hamiltonian, with a single Dirac cone at $\boldsymbol{k} = (k_x, k_y) = 0$.

Since it is computationally expensive to work with a three-dimensional (3D) lattice, one would like to be able to discretize the 2D Dirac Hamiltonian, without introducing a second Dirac cone. We can draw inspiration from lattice gauge theory, where a variety of strategies have been developed to avoid fermion doubling [103, 104]. The condensed matter context introduces its own complications, notably the lack of translational invariance and breaking of chiral symmetry by disorder and boundaries.

In Ref. 105 it was shown how the transfer matrix of the Dirac equation in a disorder potential can be discretized without fermion doubling. This allows for efficient calculation of the conductance and other transport properties in an open system [106–108]. Here we apply the same approach to the Hamiltonian of a closed system, in order to study the spectral statistics.

The Nielsen-Ninomiya theorem forbids a local discretization of the eigenvalue problem $H_{\rm D}\psi = E\psi$ without fermion doubling and without breaking

the chiral symmetry relation

$$\sigma_z H_{\mathrm{D}} = -H_{\mathrm{D}}\sigma_z. \tag{6.2}$$

One way to circumvent the no-go theorem, is to abandon the locality by introducing long-range hoppings in the discretized Dirac Hamiltonian [109]. Here we follow an alternative route, following Stacey [110], which is to work with a *generalized* eigenvalue problem

$$\mathcal{H}\psi = E\mathcal{P}\psi, \tag{6.3}$$

with *local* tight-binding operators $\mathcal{H}$ and $\mathcal{P}$ on both sides of the equation. Going beyond Ref. 110, we transform the operators $\mathcal{H}$ and $\mathcal{P}$ such that they remain, respectively, Hermitian and positive definite in the absence of translational invariance. This favors a stable and efficient numerical solution, and moreover guarantees that the resulting spectrum is real, not only in the continuum limit but at any grid size.

A key feature of our approach, compared with the more familiar approaches of Wilson fermions [111] and Susskind fermions [112], is that both the chiral symmetry (6.2) is preserved and the symplectic time-reversal symmetry[1]

$$\sigma_y H_{\mathrm{D}}^* \sigma_y = H_{\mathrm{D}}. \tag{6.4}$$

This also implies the conservation of the product of the chiral and symplectic symmetries, which is a particle-hole symmetry,

$$\sigma_x H_{\mathrm{D}}^* \sigma_x = -H_{\mathrm{D}}. \tag{6.5}$$

To demonstrate the capabilities of our approach we calculate the spectral statistics of a disordered system and show how the numerics distinguishes broken versus preserved chiral or symplectic symmetry in each of the four symmetry classes of random-matrix theory [113].

The outline of the chapter is as follows: In the next section we formulate the generalized eigenproblem, first following Stacey [110] for a translationally invariant system, and then including disorder. The symmetrization that produces a Hermitian $\mathcal{H}$ and positive definite $\mathcal{P}$ is introduced in Sec. 6.3. The locality of the discretization scheme is demonstrated by the construction of a locally conserved current in Sec. 6.4. By applying different

[1] The complex conjugation operation $\mathcal{K}$ in the symmetry relations (6.4) and (6.5) is taken in the position basis. In momentum representation the relations read $\sigma_y H^*(-\boldsymbol{k})\sigma_y = H(\boldsymbol{k})$ and $\sigma_x H^*(-\boldsymbol{k})\sigma_x = -H(\boldsymbol{k})$. Both symplectic and particle-hole symmetries are anti-unitary symmetries, with operators $\mathcal{T} = i\sigma_y\mathcal{K}$ and $\mathcal{C} = \sigma_x\mathcal{K}$ that square to -1 and $+1$, respectively.

types of disorder, in scalar potential, vector potential, or mass, we can access the different symmetry classes and obtain the characteristic spectral statistics for each, as we show in Sec. 6.5. We conclude in Sec. 6.6.

6.2 Construction of the generalized eigenproblem

6.2.1 Staggered discretization

If we discretize the Dirac Hamiltonian (6.1) on a lattice (lattice constant a), the replacement of the momentum k by $a^{-1}\sin ka$ produces a second Dirac cone at the edge of the Brillouin zone ($k = \pi/a$). To place our work into context, we summarize methods to remove this spurious low-energy excitation.

If one is willing to abandon the locality of the Hamiltonian, one can eliminate the fermion doubling by a discretization of the spatial derivative that involves all lattice points, $df/dx \mapsto \sum_n (-1)^n n^{-1} f(x - na)$. The resulting dispersion remains strictly linear in the first Brillouin zone. This discretization scheme goes by the name of SLAC fermions [109] in the high-energy physics literature. It has recently been implemented in a condensed matter context [114].

An alternative line of approach preserves the locality at the expense of a symmetry breaking. The simplest way is to couple the top and bottom surfaces of the topological insulator slab [95, 115]. The coupling adds a momentum dependent mass term $\mu\sigma_z(1 - \cos ka)$ which gaps out the second cone, while breaking both chiral symmetry and symplectic symmetry[2]. This is the Wilson fermion regularization of lattice gauge theory [111, 116]. The product of chiral and symplectic symmetry is preserved by Wilson fermions, which may be sufficient for some applications [117, 118].

It is possible to maintain the chiral symmetry by discretizing the Dirac Hamiltonian on a pair of staggered grids. Much of the lattice gauge theory literature is based on the Susskind discretization [112], which applies a different grid to each of the two components of the spinor wave function ψ. On a 2D lattice it reduces the number of Dirac cones in the Brillouin

[2] Breaking of the symplectic symmetry (6.4) does not necessarily imply breaking of time-reversal symmetry. While a mass term $\mu\sigma_z(1 - \cos ka)$ due to the coupling of top and bottom surfaces in a topological insulator slab breaks symplectic symmetry, time-reversal symmetry is preserved, because the time-reversal operation also changes the sign of μ.

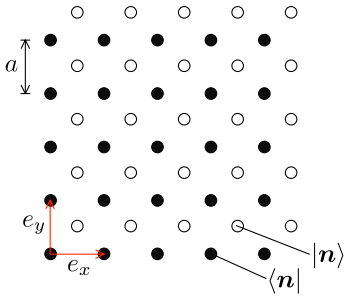

Figure 6.1: A pair of staggered grids (lattice constant a, lattice vectors e_x, e_y) used in the Stacey discretization of the 2D Dirac equation. The wave function and its spatial derivatives are evaluated at the open lattice points, in terms of the values on the four neighboring closed lattice points. The basis states $\langle\boldsymbol{n}|$ and $|\boldsymbol{n}\rangle$ on the two lattices are indicated.

zone from 4 to 2. Chiral symmetry is preserved, but symplectic symmetry is broken by the Susskind discretization (see App. 6.A).

Hammer, Pötz, and Arnold [119, 120] have developed an ingenious single-cone discretization method for the *time-dependent* Dirac equation. As in the Susskind discretization, different grids are used for each of the spinor components, but these are staggered not only in space but also in time. While this method is well suited for dynamical simulations [121, 122], it is not easily adapted to energy-resolved spectral studies.

An altogether different approach, introduced by Stacey [110, 123], is to evade the fermion-doubling no-go theorem by the replacement of the conventional eigenvalue problem $H_\mathrm{D}\psi = E\psi$ by a generalized eigenproblem $U\psi = E\Phi\psi$. There is now no obstruction to having a local U and Φ and also preserving chiral and symplectic symmetry.

The Stacey discretization of the transfer matrix was implemented in Ref. 105. In what follows we show how to apply it to the Hamiltonian, to solve the time-independent Dirac equation on a 2D lattice. In the next subsection we first summarize the results of Ref. 110 for a translationally invariant system, and then will present the modifications needed to apply the method in the presence of a disorder potential.

6.2.2 Translationally invariant system

We seek to discretize the Dirac equation $H_\mathrm{D}\psi = E\psi$ on a 2D square lattice (lattice constant a). We denote the discretized wave function by $\psi_{\boldsymbol{n}}$, with $\boldsymbol{n} = (n_x, n_y) \in \mathbb{Z}^2$ labeling the lattice points at $n_x e_x + n_y e_y$.

For ease of notation we will henceforth set v_{F}, $\hbar$, and a to unity.

Staggered discretization *a la* Stacey means that the wave function and its spatial derivatives are evaluated on a displaced lattice with sites at the center of the unit cells of the original lattice (see Fig. 6.1). The discretization rules are:

$$\frac{\partial\psi}{\partial x} \mapsto \tfrac{1}{2}(\psi_{\boldsymbol{n}+e_x} + \psi_{\boldsymbol{n}+e_x+e_y} - \psi_{\boldsymbol{n}} - \psi_{\boldsymbol{n}+e_y}), \tag{6.6a}$$

$$\frac{\partial\psi}{\partial y} \mapsto \tfrac{1}{2}(\psi_{\boldsymbol{n}+e_y} + \psi_{\boldsymbol{n}+e_x+e_y} - \psi_{\boldsymbol{n}} - \psi_{\boldsymbol{n}+e_x}), \tag{6.6b}$$

$$\psi \mapsto \tfrac{1}{4}(\psi_{\boldsymbol{n}} + \psi_{\boldsymbol{n}+e_x} + \psi_{\boldsymbol{n}+e_y} + \psi_{\boldsymbol{n}+e_x+e_y}). \tag{6.6c}$$

In distinction to Susskind staggering, the same discretization applies to each spinor component.

In momentum representation, $\psi(\boldsymbol{k}) = \sum_{\boldsymbol{n}} \psi_{\boldsymbol{n}} e^{-i\boldsymbol{k}\cdot\boldsymbol{n}}$, the discretized Dirac equation reads

$$U(\boldsymbol{k})\psi(\boldsymbol{k}) = E\Phi(\boldsymbol{k})\psi(\boldsymbol{k}), \tag{6.7}$$

with the $\boldsymbol{k}$-dependent operators

$$\begin{aligned} U &= -\tfrac{1}{2}i\sigma_x(e^{ik_x}-1)(e^{ik_y}+1) - \tfrac{1}{2}i\sigma_y(e^{ik_x}+1)(e^{ik_y}-1), \\ \Phi &= \tfrac{1}{4}(e^{ik_x}+1)(e^{ik_y}+1). \end{aligned} \tag{6.8}$$

The dispersion relation

$$E(\boldsymbol{k}) = \pm 2\sqrt{\tan^2(k_x/2) + \tan^2(k_y/2)} \tag{6.9}$$

has a single Dirac point at $\boldsymbol{k} = 0$. The Dirac point at the edge of the Brillouin zone has been converted into a pole by the Stacey discretization.

6.2.3 Including a disorder potential

We break translational invariance by including in the Dirac equation a spatially dependent scalar potential $V\sigma_0$, vector potential $A_x\sigma_x + A_y\sigma_z$, and mass $M\sigma_z$,

$$(-i\nabla + e\boldsymbol{A})\cdot\boldsymbol{\sigma}\psi + (V\sigma_0 + M\sigma_z)\psi = E\psi. \tag{6.10}$$

The electron charge e is set to unity in what follows. The Pauli matrices $\boldsymbol{\sigma} = (\sigma_x, \sigma_y)$ and σ_z act on the spin degree of freedom, with σ_0 the 2×2 unit matrix.

symmetry	symplectic	chiral	particle-hole	class
$V \neq 0 \neq M$	×	×	×	A
$V \neq 0 = M, \boldsymbol{A}$	✓	×	×	AII
$\boldsymbol{A} \neq 0 = V, M$	×	✓	×	AIII
$M \neq 0 = V, \boldsymbol{A}$	×	×	✓	D

Table 6.1: The four symmetry classes realized by single-cone Dirac fermions [113]. The table lists the broken (×) and preserved (✓) symmetries of the Dirac Hamiltonian, in the presence of a scalar potential V, vector potential $\boldsymbol{A}$, and mass M. Class A applies if at least two of the three $V, M, \boldsymbol{A}$ are nonzero.

On the surface of a topological insulator the mass term represents a perpendicular magnetization. Alternatively, we can consider a 2D topological superconductor with chiral p-wave pair potential, described by the Bogoliubov-de Gennes (BdG) Hamiltonian

$$H_{\mathrm{BdG}} = \left(\frac{k^2}{2m} + V - E_{\mathrm{F}}\right)\sigma_z + v_\Delta(\boldsymbol{k}\cdot\boldsymbol{\sigma}). \tag{6.11}$$

The Pauli matrices now act on the electron-hole degree of freedom, electrons and holes are coupled by the pair potential $\propto v_\Delta$. Since this coupling is linear in momentum k, the quadratic kinetic energy $k^2/2m$ can be neglected near $k = 0$. The difference $V - E_{\mathrm{F}}$ of electrostatic potential V and Fermi energy E_{F} then plays the role of the mass term M in Eq. (6.10).

The low-energy physics of the problem is governed by three symmetry relations, the chiral symmetry (6.2), the symplectic symmetry (6.4), and the particle-hole symmetry (6.5). Chiral symmetry is preserved by $\boldsymbol{A}$ and broken by V or M. Symplectic symmetry is preserved by V and broken by M or $\boldsymbol{A}$. If at least two of the three potentials $V, M, \boldsymbol{A}$ are nonzero all symmetries of the Dirac Hamiltonian are broken. Finally, if $V = 0$, $\boldsymbol{A} = 0$ while $M \neq 0$ the particle-hole symmetry (6.5) remains. Table 6.1 summarizes the symmetry classification [113].

The inclusion of the vector potential requires a separate consideration, in order to preserve gauge invariance. We delay that to Sec. 6.4, at first we only include V and M.

To incorporate the spatially dependent terms in the discretization scheme we write the operators U and Φ in the position basis. In view of the identity

$$e^{ik_\alpha} = \sum_{\boldsymbol{n}} |\boldsymbol{n}\rangle\langle\boldsymbol{n}|e^{ik_\alpha} = \sum_{\boldsymbol{n}} |\boldsymbol{n}\rangle\langle\boldsymbol{n} + e_\alpha|, \tag{6.12}$$

we have

$$U = -\tfrac{1}{2} i\sigma_x \Omega_{+-} - \tfrac{1}{2} i\sigma_y \Omega_{-+}, \quad \Phi = \tfrac{1}{4}\Omega_{++}, \tag{6.13}$$

$$\Omega_{ss'} = \sum_{\boldsymbol{n}} \Big(ss'|\boldsymbol{n}\rangle\langle \boldsymbol{n}| + s|\boldsymbol{n}\rangle\langle \boldsymbol{n}+e_x| + s'|\boldsymbol{n}\rangle\langle \boldsymbol{n}+e_y| + |\boldsymbol{n}\rangle\langle \boldsymbol{n}+e_x+e_y| \Big). \tag{6.14}$$

For later use we also define the factorization $\Phi = \Phi_x \Phi_y$, with commuting operators Φ_x, Φ_y given by

$$\Phi_\alpha = \tfrac{1}{2}(e^{ik_\alpha} + 1) = \tfrac{1}{2} \sum_{\boldsymbol{n}} \Big(|\boldsymbol{n}\rangle\langle \boldsymbol{n}| + |\boldsymbol{n}\rangle\langle \boldsymbol{n}+e_\alpha| \Big). \tag{6.15}$$

In these equations the ket states $|\boldsymbol{n}\rangle$ refer to sites on the displaced lattice (open lattice points in Fig. 6.1), while the bra states $\langle \boldsymbol{n}|$ refer to sites on the original lattice (closed lattice points). The inner product is defined such that the two sets of eigenstates of position are orthonormal, $\langle \boldsymbol{n}'|\boldsymbol{n}\rangle = \delta_{\boldsymbol{n},\boldsymbol{n}'}$.

We define the potential and mass operators,

$$V = \sum_{\boldsymbol{n}} V_{\boldsymbol{n}} |\boldsymbol{n}\rangle\langle \boldsymbol{n}|, \quad M = \sum_{\boldsymbol{n}} M_{\boldsymbol{n}} |\boldsymbol{n}\rangle\langle \boldsymbol{n}|, \tag{6.16}$$

where $V_{\boldsymbol{n}}$ and $M_{\boldsymbol{n}}$ denote the value at the open lattice point $\boldsymbol{n}$. With this notation we have the discretized Dirac equation

$$U\psi + (V\sigma_0 + M\sigma_z)\Phi\psi = E\Phi\psi. \tag{6.17}$$

The product $V\Phi\psi$ multiplies the value of V on an open lattice point with the average of the values of ψ on the four adjacent closed lattice points, and similarly for $M\Phi\psi$.

Eq. (6.17) is a generalized eigenvalue problem, with operators on both sides of the equation. Neither operator is Hermitian. This is problematic in a numerical implementation, and we will show in the next section how to resolve that difficulty.

6.3 Symmetrization of the generalized eigenproblem

We wish to rewrite Eq. (6.17) in the form $\mathcal{H}\psi = E\mathcal{P}\psi$, with Hermitian $\mathcal{H}$ and Hermitian positive definite $\mathcal{P}$. Such a symmetrization of the generalized eigenvalue problem allows for a stable and efficient numerical solution

[124, 125][3]. Moreover, it guarantees real eigenvalues E and eigenvectors ψ_E that satisfy the orthogonality relation $\langle\psi_E|\mathcal{P}|\psi'_E\rangle = 0$ if $E \neq E'$.

We multiply both sides of Eq. (6.17) by $\Phi^\dagger$ and note that

$$\Phi^\dagger U = \tfrac{1}{2}\sigma_x(1+\cos k_y)\sin k_x + \tfrac{1}{2}\sigma_y(1+\cos k_x)\sin k_y \tag{6.18}$$

is a Hermitian operator. In position basis, this reads

$$\Phi^\dagger U = -i\boldsymbol{D}\cdot\boldsymbol{\sigma}, \quad \boldsymbol{D} = (D_x, D_y), \tag{6.19a}$$

$$D_x = \tfrac{1}{8}\sum_{\boldsymbol{n}}\Big(2|\boldsymbol{n}\rangle\langle\boldsymbol{n}+e_x| + |\boldsymbol{n}\rangle\langle\boldsymbol{n}+e_x+e_y| + |\boldsymbol{n}\rangle\langle\boldsymbol{n}+e_x-e_y|\Big) - \text{H.c}, \tag{6.19b}$$

$$D_y = \tfrac{1}{8}\sum_{\boldsymbol{n}}\Big(2|\boldsymbol{n}\rangle\langle\boldsymbol{n}+e_y| + |\boldsymbol{n}\rangle\langle\boldsymbol{n}+e_x+e_y| + |\boldsymbol{n}\rangle\langle\boldsymbol{n}+e_y-e_x|\Big) - \text{H.c.} \tag{6.19c}$$

We thus arrive at the generalized eigenproblem

$$\begin{aligned} &\mathcal{H}\psi = E\mathcal{P}\psi, \quad \mathcal{P} = \Phi^\dagger\Phi, \\ &\mathcal{H} = -i\boldsymbol{D}\cdot\boldsymbol{\sigma} + \Phi^\dagger(V\sigma_0 + M\sigma_z)\Phi, \end{aligned} \tag{6.20}$$

with Hermitian $\mathcal{H}$ and positive semi-definite $\mathcal{P}$. Moreover, $\mathcal{P}$ is positive definite provided that Φ has no zero-modes, which is the case if the edges of the Brillouin zone (k_x or k_y equal to $\pm\pi$) are excluded from the spectrum. To ensure that, we can choose an odd number N_x, N_y of lattice points with periodic boundary conditions in the x- and y-directions (or alternatively, even N_x, N_y with antiperiodicity).

By way of illustration, we work out the expectation value

$$\langle\psi|\Phi^\dagger V\sigma_0\Phi|\psi\rangle = \sum_{\boldsymbol{n}} V_{\boldsymbol{n}}|\tfrac{1}{4}(\psi_{\boldsymbol{n}} + \psi_{\boldsymbol{n}+e_x} + \psi_{\boldsymbol{n}+e_y} + \psi_{\boldsymbol{n}+e_x+e_y})|^2, \tag{6.21}$$

so the value of the potential on an open lattice point is multiplied by the norm squared of the average of the wave function amplitudes on the four adjacent closed lattice points.

Eq. (6.20) is local in the sense that the operators $\mathcal{H}$ and $\mathcal{P}$ only couple nearby lattice sites. It can be converted into a conventional eigenvalue problem $\tilde{\mathcal{H}}\tilde{\psi} = E\tilde{\psi}$ with $\tilde{\psi} = \Phi\psi$ and $\tilde{\mathcal{H}}$ a *nonlocal* effective Hamiltonian:

$$\tilde{\mathcal{H}} = (\Phi^\dagger)^{-1}\mathcal{H}\Phi^{-1} = U\Phi^{-1} + \sigma_0 V + M\sigma_z. \tag{6.22}$$

[3]Both $\mathcal{H}$ and $\mathcal{P}$ should be Hermitian and one of these operators should be positive semi-definite to guarantee real eigenvalues of $\mathcal{H}\psi = E\mathcal{P}\psi$. Hermiticity alone is not sufficient, see the counterexample $\mathcal{H} = \sigma_x$, $\mathcal{P} = \sigma_z$ with eigenvalues $E = \pm i$.

In the translationally invariant case, the effective Hamiltonian reduces simply to

$$\tilde{\mathcal{H}} = 2\sigma_x \tan(k_x/2) + 2\sigma_y \tan(k_y/2). \tag{6.23}$$

Both chiral symmetry and symplectic symmetry are preserved on the lattice if present in the continuum description: $\sigma_z\tilde{\mathcal{H}} = -\tilde{\mathcal{H}}\sigma_z$ when $V = 0 = M$, and $\sigma_y\tilde{\mathcal{H}}^*\sigma_y = \tilde{\mathcal{H}}$ when $M = 0$.

6.4 Locally conserved particle current

In real space the effective Hamiltonian (6.22) produces infinitely long-range hoppings, as in the SLAC fermion discretization [109, 114]. The transformation to the generalized eigenproblem (6.20) restores the locality of the hoppings. One might wonder whether there is a physical content to this mathematical statement. Yes there is, as we show in this section the Stacey discretization allows for the construction of a locally conserved particle current.

We define the particle number

$$\langle\tilde{\psi}|\tilde{\psi}\rangle = \langle\psi|\Phi^\dagger\Phi|\psi\rangle, \tag{6.24}$$

corresponding to the density operator

$$\rho(\boldsymbol{n}) = \Phi^\dagger|\boldsymbol{n}\rangle\langle\boldsymbol{n}|\Phi. \tag{6.25}$$

With reference to the two staggered grids in Fig. 6.1, the particle density on an open lattice point $\boldsymbol{n}$ is given by the norm squared of the average of the wave function on the four adjacent closed lattice points,

$$\langle\psi|\rho(\boldsymbol{n})|\psi\rangle = |\tfrac{1}{4}(\psi_{\boldsymbol{n}} + \psi_{\boldsymbol{n}+e_x} + \psi_{\boldsymbol{n}+e_y} + \psi_{\boldsymbol{n}+e_x+e_y})|^2. \tag{6.26}$$

The current density operator is given by

$$j_\alpha(\boldsymbol{n}) = (\Phi_\alpha^\dagger)^{-1}\sigma_\alpha\rho(\boldsymbol{n})\Phi_\alpha^{-1}, \tag{6.27}$$

or equivalently,

$$\begin{aligned} j_x(\boldsymbol{n}) &= \sigma_x \sum_{\boldsymbol{n}} \Phi_y^\dagger|\boldsymbol{n}\rangle\langle\boldsymbol{n}|\Phi_y, \\ j_y(\boldsymbol{n}) &= \sigma_y \sum_{\boldsymbol{n}} \Phi_x^\dagger|\boldsymbol{n}\rangle\langle\boldsymbol{n}|\Phi_x, \end{aligned} \tag{6.28}$$

in terms of the operators Φ_x, Φ_y defined in Eq. (6.15). The current density in the state ψ then takes the form

$$\begin{aligned}\langle\psi|j_x(\boldsymbol{n})|\psi\rangle &= \tfrac{1}{4}(\psi_{\boldsymbol{n}}+\psi_{\boldsymbol{n}+e_y})^\dagger\sigma_x(\psi_{\boldsymbol{n}}+\psi_{\boldsymbol{n}+e_y}),\\ \langle\psi|j_y(\boldsymbol{n})|\psi\rangle &= \tfrac{1}{4}(\psi_{\boldsymbol{n}}+\psi_{\boldsymbol{n}+e_x})^\dagger\sigma_y(\psi_{\boldsymbol{n}}+\psi_{\boldsymbol{n}+e_x}).\end{aligned} \tag{6.29}$$

The current density at an open lattice point is evaluated by averaging the wave function at the two nearby closed lattice points connected by an edge perpendicular to the current flow.

The local conservation law

$$-\frac{\partial}{\partial t}\langle\psi|\rho(\boldsymbol{n})|\psi\rangle = \sum_{\alpha=x,y}\langle\psi|j_\alpha(\boldsymbol{n}+e_\alpha)-j_\alpha(\boldsymbol{n})|\psi\rangle \tag{6.30}$$

is derived in App. 6.B.

Knowledge of the current operator allows us to introduce the vector potential operator $\boldsymbol{A}=\sum_{\boldsymbol{n}}\boldsymbol{A}_{\boldsymbol{n}}|\boldsymbol{n}\rangle\langle\boldsymbol{n}|$ such that

$$\lim_{\boldsymbol{A}\to 0}\frac{\partial\mathcal{H}}{\partial\boldsymbol{A}_{\boldsymbol{n}}} = \boldsymbol{j}(\boldsymbol{n}). \tag{6.31}$$

This is satisfied if

$$\mathcal{H} = -i\boldsymbol{D}\cdot\boldsymbol{\sigma}+\Phi^\dagger\big(V\sigma_0+M\sigma_z\big)\Phi+\Phi_y^\dagger\sigma_x A_x\Phi_y+\Phi_x^\dagger\sigma_y A_y\Phi_x+\mathcal{O}(A^2). \tag{6.32}$$

In App. 6.C we check that the Hamiltonian (6.32) is gauge invariant to first order in A. Higher order terms are nonlocal and we will not include them.

6.5 Spectral statistics

We have solved the generalized eigenproblem

$$\begin{aligned}&\mathcal{H}\psi = E\mathcal{P}\psi,\ \ \mathcal{P}=\Phi^\dagger\Phi,\\ &\mathcal{H} = -i\boldsymbol{D}\cdot\boldsymbol{\sigma}+\Phi^\dagger\big(V\sigma_0+M\sigma_z\big)\Phi+\Phi_y^\dagger\sigma_x A_x\Phi_y+\Phi_x^\dagger\sigma_y A_y\Phi_x\end{aligned} \tag{6.33}$$

on a square lattice of size $N_x\times N_y$. Antiperiodic boundary conditions in the x- and y-direction account for the π Berry phase accumulated by the spin when it makes one full rotation. The dimensions N_x, N_y are even to

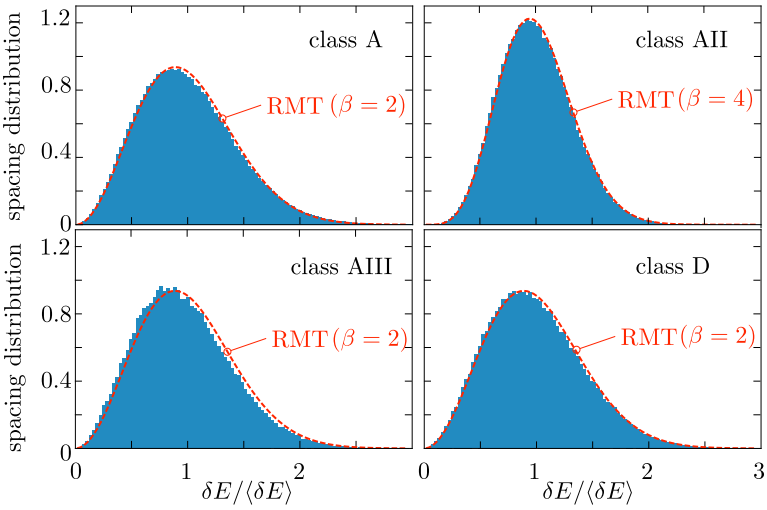

Figure 6.2: Histograms: Spacing distributions computed from the discretized Dirac Hamiltonian (6.33), with different types of disorder corresponding to the four symmetry classes in Table 6.1. The red dashed line is the prediction (6.34) from random-matrix theory in the presence of symplectic symmetry ($\beta = 4$) and in its absence ($\beta = 2$).

ensure a positive definite Φ (no zero-mode in the spectrum). The spectrum was calculated for $5 \cdot 10^4$ realizations of a random disorder, chosen independently on each site from a uniform distribution in the interval $(-\delta, \delta)$.

To access the four symmetry classes from Table 6.1 we took

- $A_x, A_y \equiv 0$ and random V, M with $\delta = 15/\sqrt{2}$ for class A;
- $M, A_x, A_y \equiv 0$ and random V with $\delta = 15$ for class AII;
- $V, M \equiv 0$ and random A_x, A_y with $\delta = \frac{1}{4}\sqrt{2}$ for class AIII;
- $V, A_x, A_y \equiv 0$ and random M with $\delta = 15$ for class D.

The relatively weak disorder in class AIII was chosen in view of the linearization in the vector potential. For that case we took $N_x = N_y = 150$, in the other symmetry classes with stronger disorder we took $N_x = N_y = 100$.

Symmetry class D is insulating for weak disorder in the mass $M \in (-\delta, \delta)$, it undergoes a metal-insulator transition at $\delta_c = 3.44$ [106]. This

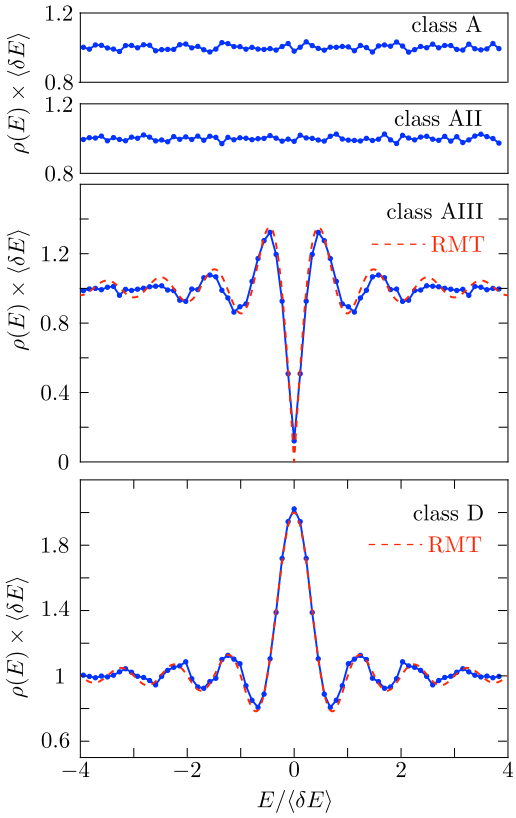

Figure 6.3: Density of states in the four symmetry classes, calculated numerically from the discretized Dirac Hamiltonian (blue solid lines) and compared with the RMT prediction (6.35) (red dashed lines). Chiral symmetry introduces a linear dip (class AIII), while particle-hole symmetry introduces a quadratic peak (class D).

is the thermal metal phase of a topological superconductor [126]. The thermal metal can be reached by vortex disorder, as in the network model studied in Ref. 127, or it can be reached by electrostatic disorder in the BdG Hamiltonian (6.11), as in the tight-binding models studied in Refs. 106, 128. Here we follow the latter approach, taking $\delta = 15$ much larger than δ_c, so that we are deep in the metallic regime.

In Fig. 6.2 we show the probability distribution of the level spacing δE in the bulk of the spectrum, far from $E = 0$, where the average spacing

$\langle E \rangle$ is energy independent. We compare with the Wigner surmise from random-matrix theory (RMT) [129],

$$P(s) = \begin{cases} \frac{32}{\pi^2} s^2 e^{-4s^2/\pi} & \text{in class A, AIII, D,} \\ \frac{2^{18}}{(9\pi)^3} s^4 e^{-64s^2/9\pi} & \text{in class AII,} \end{cases} \tag{6.34}$$

with $s = \delta E / \langle \delta E \rangle$. The characteristic difference between the two distributions is the decay $\propto s^\beta$ for small spacings, with $\beta = 4$ in the presence of symplectic symmetry, while $\beta = 2$ in its absence. (The case $\beta = 1$ of RMT is not realized in a spin-full system.)

In Fig. 6.3 we make a similar comparison for the density of states near $E = 0$. In class A and AII the ensemble averaged density of states $\rho(E)$ is flat in a broad energy range around $E = 0$. Chiral symmetry in class AIII introduces a linear dip in the density of states, while particle-hole symmetry in class D introduces a quadratic peak. The RMT predictions are [130]

$$\rho(E) = \frac{1}{\langle \delta E \rangle} \times \begin{cases} \frac{1}{2}\pi^2 |\varepsilon| \left[J_0^2(\pi\varepsilon) + J_1^2(\pi\varepsilon) \right] & \text{in class AIII,} \\ 1 + (2\pi\varepsilon)^{-1} \sin(2\pi\varepsilon) & \text{in class D,} \end{cases} \tag{6.35}$$

with $\varepsilon = E / \langle \delta E \rangle$. The mean level spacing $\langle \delta E \rangle$ is computed away from $E = 0$.

The good agreement between the numerical results from the disordered Dirac equation and the RMT predictions, evident in Figs. 6.2 and 6.3, is reached without any adjustable parameter.

6.6 Conclusion

In conclusion, we have developed and implemented a lattice fermion Hamiltonian that, unlike the familiar Wilson fermion and Susskind fermion Hamiltonians [111, 112], preserves both chiral symmetry and symplectic symmetry while avoiding fermion doubling. Our approach is a symmetrized version of Stacey's generalized eigenvalue problem [110], which allows for the construction of a locally conserved particle current. To demonstrate the universal applicability of the lattice fermion Hamiltonian we have shown how it can reproduce the characteristic spectral statistics for each of the four symmetry classes of Dirac fermions. We believe this to be the first demonstration of a single-cone discretization scheme with that capability.

Appendices

6.A Susskind discretization breaks symplectic symmetry

The staggered discretization of the 2D Dirac equation *a la* Susskind [112] produces a conventional eigenvalue problem, with a local Hamiltonian. There is a single Dirac cone in 1D but there are 2 Dirac cones in 2D. Chiral symmetry is preserved, but symplectic symmetry is broken. To contrast this with the symplectic-symmetry-preserving single-cone Stacey discretization used in the main text, we give a brief description of the Susskind discretization, first in 1D and then in 2D.

In 1D the staggering refers to the prescription that the derivative of the A component of the spinor $\psi = (\psi_A, \psi_B)$ is calculated at $x = n + 1/2$, while the derivative of the B component is calculated at $x = n - 1/2$. Hence the term $k_x\sigma_x$ in the Dirac Hamiltonian is substituted by

$$\begin{aligned} k_x\sigma_x\psi \mapsto -i\begin{pmatrix} \psi_B(n) - \psi_B(n-1) \\ \psi_A(n+1) - \psi_A(n) \end{pmatrix} \\ \Rightarrow H_{\rm D} \mapsto -i\begin{pmatrix} 0 & 1 - e^{-\partial_x} \\ e^{\partial_x} - 1 & 0 \end{pmatrix}. \end{aligned} \tag{6.36}$$

The exponential e^{∂_x}, with $\partial_x = \partial/\partial x$, is the translation operator: $e^{\partial_x}\psi(x) = \psi(x+1)$.

In momentum representation, $\partial_x \mapsto ik_x$, the discretized Hamiltonian reads

$$H = \sigma_x \sin k_x + \sigma_y(1 - \cos k_x). \tag{6.37}$$

The corresponding dispersion relation

$$E(k_x) = \pm\sqrt{2 - 2\cos k_x} \tag{6.38}$$

has a single Dirac cone at $k_x = 0$ in the Brillouin zone $-\pi < k_x \leq \pi$.

The 2D generalization is

$$\begin{aligned} H_{\mathrm{D}} \mapsto & -\tfrac{1}{2}i\begin{pmatrix} 0 & (1-e^{-\partial_x})(1+e^{\partial_y}) \\ (e^{\partial_x}-1)(1+e^{-\partial_y}) & 0 \end{pmatrix} \\ & -\tfrac{1}{2}i\begin{pmatrix} 0 & -i(1-e^{\partial_y})(1+e^{-\partial_x}) \\ i(e^{-\partial_y}-1)(1+e^{\partial_x}) & 0 \end{pmatrix} \\ = & \tfrac{1}{2}\big(\sigma_x+\sigma_y\big)\big(\sin(k_x-k_y)-\cos k_x+\cos k_y\big) \\ & +\tfrac{1}{2}(\sigma_x-\sigma_y)\big(\cos(k_x-k_y)+\sin k_x+\sin k_y-1\big). \end{aligned} \tag{6.39}$$

The resulting dispersion relation,

$$E(k_x,k_y)=\pm\sqrt{2-2\cos k_x\cos k_y}, \tag{6.40}$$

vanishes at $\boldsymbol{k}=(0,0)$ and $\boldsymbol{k}=(\pi,\pi)$. (This is the dispersion studied in Ref. 131.) Without staggering there would also have been Dirac cones at $\boldsymbol{k}=(0,\pi)$ and $(\pi,0)$, so the number of Dirac cones in the Brillouin zone has been halved by the Susskind discretization.

Chiral symmetry is preserved, H_{D} still anticommutes with σ_z in its discretized form (6.39). But symplectic symmetry is broken: $\sigma_y H^*\sigma_y \neq H$ after discretization. To ensure symplectic symmetry each Pauli matrix should be multiplied by an odd function of $\boldsymbol{k}$, while Eq. (6.39) contains a mixture of odd and even functions of $\boldsymbol{k}$.

6.B Derivation of the local conservation law for the particle current

To derive Eq. (6.30) we first note the identity

$$\frac{\partial}{\partial t}\langle\psi|O|\psi\rangle = i\langle\psi|\Phi^\dagger[\tilde{H},\tilde{O}]\Phi|\psi\rangle, \tag{6.41}$$

which holds for any operator O, with $\tilde{O}=(\Phi^\dagger)^{-1}O\Phi^{-1}$. The nonlocal effective Hamiltonian $\tilde{H}$ is defined in Eq. (6.22).

We take for O the density operator (6.25), so $\tilde{\rho}(\boldsymbol{n})=|\boldsymbol{n}\rangle\langle\boldsymbol{n}|$. This projector commutes with the operators V and M in $\tilde{H}$, what remains is the commutator with $U\Phi^{-1}$:

$$\begin{aligned} -\frac{\partial}{\partial t}\langle\psi|\rho(\boldsymbol{n})|\psi\rangle &= -i\langle\psi|\Phi^\dagger\big[U\Phi^{-1},|\boldsymbol{n}\rangle\langle\boldsymbol{n}|\big]\Phi|\psi\rangle \\ &= i\langle\psi|\Phi^\dagger|\boldsymbol{n}\rangle\langle\boldsymbol{n}|U|\psi\rangle - i\langle\psi|\Phi^\dagger U\Phi^{-1}|\boldsymbol{n}\rangle\langle\boldsymbol{n}|\Phi|\psi\rangle \\ &= i\langle\psi|\Phi^\dagger|\boldsymbol{n}\rangle\langle\boldsymbol{n}|U|\psi\rangle + \text{H.c.} \end{aligned} \tag{6.42}$$

In the last equality we used that $\Phi^\dagger U = U^\dagger \Phi$.

In terms of the current operator (6.27) we have

$$\begin{aligned} i\Phi^\dagger|\boldsymbol{n}\rangle\langle\boldsymbol{n}|U &= \tfrac{1}{2}\sum_{\alpha=x,y}(e^{-ik_\alpha}+1)j_\alpha(\boldsymbol{n})(e^{ik_\alpha}-1) \\ \Rightarrow i\Phi^\dagger|\boldsymbol{n}\rangle\langle\boldsymbol{n}|U + \text{H.c} &= \sum_{\alpha=x,y}\Big(e^{-ik_\alpha}j_\alpha(\boldsymbol{n})e^{ik_\alpha} - j_\alpha(\boldsymbol{n})\Big) \\ &= \sum_{\alpha=x,y}\Big(j_\alpha(\boldsymbol{n}+e_\alpha) - j_\alpha(\boldsymbol{n})\Big). \end{aligned} \tag{6.43}$$

Substitution into Eq. (6.42) gives the conservation law (6.30).

6.C Gauge invariant vector potential

To include the vector potential $\boldsymbol{A}(\boldsymbol{r})$ in a gauge invariant way in the discretized Dirac equation, we follow the procedure of minimal coupling: We first discretize without a vector potential, then perform a U(1) gauge transformation on the lattice, and finally replace the gradient of the phase field by the vector potential.

We define the gauge field operator

$$e^{i\theta} = \sum_{\boldsymbol{n}} e^{i\theta_{\boldsymbol{n}}}|\boldsymbol{n}\rangle\langle\boldsymbol{n}|, \tag{6.44}$$

with $\theta_{\boldsymbol{n}}$ the value of the phase $\theta(\boldsymbol{r})$ at site $\boldsymbol{n}$ on the displaced lattice (open points in Fig. 6.1). With this field we perform the U(1) gauge transformation

$$\begin{aligned} \tilde{\mathcal{H}} &\mapsto e^{i\theta}\tilde{\mathcal{H}}e^{-i\theta}, \\ \Rightarrow \mathcal{H} &\mapsto \Phi^\dagger e^{i\theta}(\Phi^\dagger)^{-1}\mathcal{H}\Phi^{-1}e^{-i\theta}\Phi \\ &= \Phi^\dagger e^{i\theta}U\Phi^{-1}e^{-i\theta}\Phi + \Phi^\dagger(V\sigma_0 + M\sigma_z)\Phi. \end{aligned} \tag{6.45}$$

In the last equation we have used that $e^{i\theta}$ commutes with V and M.

To proceed we apply the identity

$$\begin{aligned} &e^{-ik_\alpha}e^{i\theta}e^{ik_\alpha}e^{-i\theta} = e^{i\delta_\alpha\theta}, \\ &\delta_\alpha\theta = \sum_{\boldsymbol{n}}\big(\theta(\boldsymbol{n}+e_\alpha) - \theta(\boldsymbol{n})\big)|\boldsymbol{n}\rangle\langle\boldsymbol{n}| \end{aligned} \tag{6.46}$$

to the operator product

$$e^{i\theta}U\Phi^{-1}e^{-i\theta} = -2i\sum_{\alpha=x,y}\sigma_\alpha\frac{e^{i\theta}e^{ik_\alpha}e^{-i\theta}-1}{e^{i\theta}e^{ik_\alpha}e^{-i\theta}+1}$$
$$= -2i\sum_{\alpha=x,y}\sigma_\alpha\frac{e^{ik_\alpha}e^{i\delta_\alpha\theta}-1}{e^{ik_\alpha}e^{i\delta_\alpha\theta}+1}. \tag{6.47}$$

The gauge transformed Hamiltonian thus takes the form

$$\mathcal{H} = \Phi^\dagger\left(-2i\sum_{\alpha=x,y}\sigma_\alpha\frac{e^{ik_\alpha}e^{i\delta_\alpha\theta}-1}{e^{ik_\alpha}e^{i\delta_\alpha\theta}+1} + V\sigma_0 + M\sigma_z\right)\Phi. \tag{6.48}$$

The vector potential is then introduced by the Peierls substitution

$$\theta(\boldsymbol{n}+e_\alpha) - \theta(\boldsymbol{n}) = \int_{\boldsymbol{n}}^{\boldsymbol{n}+e_\alpha}\boldsymbol{A}(\boldsymbol{r})\cdot d\boldsymbol{l}, \tag{6.49}$$

where the line integral of the vector potential is taken along a lattice bond. With this prescription the substitution can also be applied to vector potentials that do not derive from a gauge field.

The Hamiltonian (6.48) is Hermitian but nonlocal. If the phase field varies slowly on the scale of the lattice spacing, the nonlocality can be eliminated by expanding

$$e^{i\delta_\alpha\theta} \approx 1 + i\delta_\alpha\theta \equiv 1 + iA_\alpha, \quad \boldsymbol{A} = \sum_{\boldsymbol{n}}\boldsymbol{A}_{\boldsymbol{n}}|\boldsymbol{n}\rangle\langle\boldsymbol{n}|. \tag{6.50}$$

Continuing the expansion to first order in A_α, we have

$$\frac{e^{ik_\alpha}e^{i\delta_\alpha\theta}-1}{e^{ik_\alpha}e^{i\delta_\alpha\theta}+1} = (e^{ik_\alpha}-1)(e^{ik_\alpha}+1)^{-1}$$
$$+ 2(e^{-ik_\alpha}+1)^{-1}iA_\alpha(e^{ik_\alpha}+1)^{-1} + \mathcal{O}(A_\alpha^2). \tag{6.51}$$

Substitution into Eq. (6.48) gives the Hamiltonian (6.32) to first order in the vector potential.

Bibliography

[1] M. Franz and Z. Tešanović, *Quasiparticles in the vortex lattice of unconventional superconductors: Bloch waves or Landau levels?*, Phys. Rev. Lett. **84**, 554 (2000).

[2] K. Yasui and T. Kita, *Quasiparticles of d-wave superconductors in finite magnetic fields*, Phys. Rev. Lett. **83**, 4168 (1999).

[3] L. Marinelli, B. I. Halperin, and S. H. Simon, *Quasiparticle spectrum of d-wave superconductors in the mixed state*, Phys. Rev. B **62**, 3488 (2000).

[4] N. B. Kopnin and V. M. Vinokur, *Magnetic quantization of electronic states in d-wave superconductors*, Phys. Rev. B **62**, 9770 (2000).

[5] Y. Morita and Y. Hatsugai, *Duality in the Azbel-Hofstadter problem and two-dimensional d-wave superconductivity with a magnetic duality*, Phys. Rev. Lett. **86**, 151 (2001).

[6] O. Vafek, A. Melikyan, M. Franz, and Z. Tešanović, *Quasiparticles and vortices in unconventional superconductors*, Phys. Rev. B **63**, 134509 (2001).

[7] D. Knapp, C. Kallin, and A. J. Berlinsky, *Dirac quasiparticles in the mixed state*, Phys. Rev. B **64**, 014502 (2001).

[8] O. Vafek, A. Melikyan, and Z. Tešanović, *Quasiparticle Hall transport of d-wave superconductors in the vortex state*, Phys. Rev. B **64**, 224508 (2001).

[9] A. Vishwanath, *Quantized thermal Hall effect in the mixed state of d-wave superconductors*, Phys. Rev. Lett. **87**, 217004 (2001).

[10] O. Vafek and A. Melikyan, *Index theoretic characterization of d-wave superconductors in the vortex state*, Phys. Rev. Lett. **96**, 167005 (2006).

[11] A. Melikyan and Z. Tešanović, *Dirac-Bogoliubov-deGennes quasiparticles in a vortex lattice*, Phys. Rev. B **76**, 094509 (2007).

[12] T. Meng and L. Balents, *Weyl superconductors*, Phys. Rev. B **86**, 054504 (2012). *Erratum:* Phys. Rev. B **96**, 019901 (2017).

[13] G. Bednik, A. A. Zyuzin, and A. A. Burkov, *Superconductivity in Weyl metals*, Phys. Rev. B **92**, 035153 (2015).

[14] L. Fu and C. L. Kane, *Superconducting proximity effect and Majorana fermions at the surface of a topological insulator*, Phys. Rev. Lett. **100**, 096407 (2008).

[15] Z. Zhu, M. Papaj, X.-A. Nie, H.-K. Xu, Y.-S. Gu, X. Yang, D. Guan, S. Wang, Y. Li, C. Liu, J. Luo, Z.-A. Xu, H. Zheng, L. Fu, and J.-F. Jia, *Discovery of segmented Fermi surface induced by Cooper pair momentum*, arXiv:2010.02216.

[16] Y. Aharonov and A. Casher, *Ground state of a spin-1/2 charged particle in a two-dimensional magnetic field*, Phys. Rev. A **19**, 2461 (1979).

[17] L. Alvarez-Gaumé, *Supersymmetry and the Atiyah-Singer index theorem*, Comm. Math. Phys. **90**, 161 (1983).

[18] D. Bohm, *Note on a Theorem of Bloch Concerning Possible Causes of Superconductivity*, Phys. Rev. **75**, 502 (1949).

[19] N. Yamamoto, *Generalized Bloch theorem and chiral transport phenomena*, Phys. Rev. D **92**, 085011 (2015).

[20] A. Kapustin and L. Spodyneiko, *Absence of Energy Currents in an Equilibrium State and Chiral Anomalies*, Phys. Rev. Lett. **123**, 060601 (2019).

[21] H. Watanabe, *A proof of the Bloch theorem for lattice models*, J. Stat. Phys. **177**, 717 (2019).

[22] S. L. Adler, *Axial-Vector Vertex in Spinor Electrodynamics*, Phys. Rev. **177**, 2426 (1969).

[23] J. S. Bell and R. Jackiw, *A PCAC puzzle:* $\pi^0 \to \gamma\gamma$ *in the* σ*-model*, Il Nuovo Cimento A **60**, 47 (1969).

[24] A. A. Burkov, *Chiral Anomaly and Diffusive Magnetotransport in Weyl Metals*, Phys. Rev. Lett. **113**, 247203 (2014).

[25] D. T. Son and B. Z. Spivak, *Chiral anomaly and classical negative magnetoresistance of Weyl metals*, Phys. Rev. B **88**, 104412 (2013).

[26] C.-L. Zhang, S.-Y. Xu, I. Belopolski, Z. Yuan, Z. Lin, B. Tong, G. Bian, N. Alidoust, C.-C. Lee, S.-M. Huang, T.-R. Chang, G. Chang, C.-H. Hsu, H.-T. Jeng, M. Neupane, D. S. Sanchez, H. Zheng, J. Wang, H. Lin, C. Zhang, H.-Z. Lu, S.-Q. Shen, T. Neupert, M. Z. Hasan, and S. Jia, *Signatures of the Adle-Bell-Jackiw chiral anomaly in a Weyl fermion semimetal*, Nature Comm. **7**, 10735 (2016).

[27] Q. Li, D. E. Kharzeev, C. Zhang, Y. Huang, I. Pletikosić, A. V. Fedorov, R. D. Zhong, J. A. Schneeloch, G. D. Gu, and T. Valla, *Chiral magnetic effect in $ZrTe_5$*, Nature Phys. **12**, 550 (2016).

[28] N. Bovenzi, M. Breitkreiz, P. Baireuther, T. E. O'Brien, J. Tworzydło, I. Adagideli, and C. W. J. Beenakker, *Chirality blockade of Andreev reflection in a magnetic Weyl semimetal*, Phys. Rev. B **96**, 035437 (2017).

[29] L. P. Gor'kov and J. R. Schrieffer, *de Haas–van Alphen effect in anisotropic superconductors in magnetic fields well below H_{c2}*, Phys. Rev. Lett. **80**, 3360 (1998).

[30] P. W. Anderson, *Anomalous magnetothermal resistance of high-T_c superconductors: Anomalous cyclotron orbits at a Dirac point*, arXiv:9812063.

[31] K. S. Novoselov, A. K. Geim, S. V. Morozov, D. Jiang, M. I. Katsnelson, I. V. Grigorieva, S. V. Dubonos, and A. A. Firsov, *Two-dimensional gas of massless Dirac fermions in graphene*, Nature **438**, 197 (2005).

[32] Yuanbo Zhang, Yan-Wen Tan, Horst L. Stormer, and Philip Kim, *Experimental observation of the quantum Hall effect and Berry's phase in graphene*, Nature **438**, 201 (2005).

[33] A. S. Mel'nikov, *Quantization of the quasiparticle spectrum in the mixed state of d-wave superconductors*, J. Phys. Condens. Matter **11**, 4219 (1999).

[34] G. Massarelli, G. Wachtel, J. Y. T. Wei, and A. Paramekanti, *Pseudo-Landau levels of Bogoliubov quasiparticles in nodal superconductors*, Phys. Rev. B **96**, 224516 (2017).

[35] E. M. Nica and M. Franz, *Landau levels from neutral Bogoliubov particles in two-dimensional nodal superconductors under strain and doping gradients*, Phys. Rev. B **97**, 024520 (2018).

[36] T. Liu, M. Franz, and S. Fujimoto, *Quantum oscillations and Dirac-Landau levels in Weyl superconductors*, Phys. Rev. B **96**, 224518 (2017).

[37] G. E. Volovik, *Superconductivity with lines of gap nodes: density of states in the vortex*, JETP Lett. **58**, 469 (1993).

[38] S. H. Simon and P. A. Lee, *Scaling of the quasiparticle spectrum for d-wave superconductors*, Phys. Rev. Lett. **78**, 1548 (1997).

[39] A. De Martino and R. Egger, *On the spectrum of a magnetic quantum dot in graphene*, Semicond. Sci. Technol. **25**, 034006 (2010).

[40] E. Brown, *Bloch electrons in a uniform magnetic field*, Phys. Rev. **133**, A1038 (1964).

[41] J. Zak, *Magnetic translation group*, Phys. Rev. **134**, A1602; A1607 (1964).

[42] H. J. Fischbeck, *Theory of Bloch electrons in a magnetic field*, Phys. Stat. Sol. **38**, 11 (1970).

[43] M. Diez, I. C. Fulga, D. I. Pikulin, M. Wimmer, A. R. Akhmerov, and C. W. J. Beenakker, *Phase-locked magnetoconductance oscillations as a probe of Majorana edge states*, Phys. Rev. B **87**, 125406 (2013).

[44] A. A. Soluyanov, D. Gresch, Z. Wang, Q. Wu, M. Troyer, X. Dai, and B. A. Bernevig, *Type-II Weyl semimetals*, Nature **527**, 495 (2015).

[45] T. Kawarabayashi, Y. Hatsugai, Y. Morimoto, and H. Aoki, *Generalized chiral symmetry and stability of zero modes for tilted Dirac cones*, Phys. Rev. B **83**, 153414 (2011).

[46] T. Kawarabayashi, Y. Hatsugai, Y. Morimoto, and H. Aoki, *Generalization of chiral symmetry for tilted Dirac cones*, Int. J. Mod. Phys. Conf. Series **11**, 145 (2012).

[47] T. E. O'Brien, C. W. J. Beenakker, and İ. Adagideli, *Superconductivity provides access to the chiral magnetic effect of an unpaired Weyl cone*, Phys. Rev. Lett. **118**, 207701 (2017).

[48] P. Baireuther, J. Tworzydło, M. Breitkreiz, İ. Adagideli, and C. W. J. Beenakker, *Weyl-Majorana solenoid*, New J. Phys. **19**, 025006 (2017).

[49] M. I. Katsnelson and M. F. Prokhorova, *Zero-energy states in corrugated bilayer graphene*, Phys. Rev. B **77**, 205424 (2008).

[50] J. Kailasvuori, *Pedestrian index theorem à la Aharonov-Casher for bulk threshold modes in corrugated multilayer graphene*, EPL **87**, 47008 (2009).

[51] C.-K. Lu and B. Seradjeh, *Zero modes of the generalized fermion-vortex system in magnetic field*, Phys. Rev. B **89**, 245448 (2014).

[52] C. W. Groth, M. Wimmer, A. R. Akhmerov, and X. Waintal, *Kwant: A software package for quantum transport*, New J. Phys. **16**, 063065 (2014).

[53] A. P. Schnyder and P. M. R. Brydon, *Topological surface states in nodal superconductors*, J. Phys. Condens. Matter **27**, 243201 (2015).

[54] D. J. Van Harlingen, *Phase-sensitive tests of the symmetry of the pairing state in the high-temperature superconductors*, Rev. Mod. Phys. **67**, 515 (1995).

[55] H. B. Nielsen and M. Ninomiya, *The Adler-Bell-Jackiw anomaly and Weyl fermions in a crystal*, Nucl. Phys. B **130**, 389 (1983).

[56] A. M. Turner and A. Vishwanath, *Beyond band insulators: Topology of semi-metals and interacting phases*, arXiv:1301.0330.

[57] M. J. Pacholski, C. W. J. Beenakker, and I. Adagideli, *Topologically protected Landau level in the vortex lattice of a Weyl superconductor*, Phys. Rev. Lett. **121**, 037701 (2018).

[58] C. W. J. Beenakker, *Annihilation of colliding Bogoliubov quasiparticles reveals their Majorana nature*, Phys. Rev. Lett. **12**, 070604 (2014).

[59] S. R. Elliott and M. Franz, *Majorana fermions in nuclear, particle, and solid-state physics*, Rev. Mod. Phys. **87**, 137 (2015).

[60] G. E. Volovik, *Fermion zero modes on vortices in chiral superconductors*, JETP Lett. **70**, 609 (1999).

[61] M. P. Anantram and S. Datta, *Current fluctuations in mesoscopic systems with Andreev scattering*, Phys. Rev. B **53**, 16390 (1996).

[62] U. Sivan and Y. Imry, *Multichannel Landauer formula for thermoelectric transport with application to thermopower near the mobility edge*, Phys. Rev. B **33**, 551 (1986).

[63] B. Skinner and L. Fu, *Large, nonsaturating thermopower in a quantizing magnetic field*, Science Adv. **4**, eaat2621 (2018).

[64] V. Kozii, B. Skinner, and L. Fu, *Thermoelectric Hall conductivity and figure of merit in Dirac/Weyl materials*, Phys. Rev. B **99**, 155123 (2019).

[65] W. Zhang, P. Wang, B. Skinner, R. Bi, V. Kozii, C.-W. Cho, R. Zhong, J. Schneeloch, D. Yu, G. Gu, L. Fu, X. Wu, and L. Zhang, *Observation of a thermoelectric Hall plateau in the extreme quantum limit*, Nature Comm. **11**, 1046 (2020).

[66] F. Han, N. Andrejevic, T. Nguyen, V. Kozii, Q. T. Nguyen, T. Hogan, Z. Ding, R. Pablo-Pedro, S. Parjan, B. Skinner, A. Alatas, E. Alp, S. Chi, J. Fernandez-Baca, S. Huang, L. Fu, and M. Li, *Quantized thermoelectric Hall effect induces giant power factor in a topological semimetal*, Nature Comm. **11**, 6167 (2020).

[67] M. M. Vazifeh and M. Franz, *Electromagnetic response of Weyl semimetals*, Phys. Rev. Lett. **111**, 027201 (2013).

[68] Y. Chen, S. Wu, and A. A. Burkov, *Axion response in Weyl semimetals*, Phys. Rev. B **88**, 125105 (2013).

[69] Jian-Hui Zhou, Hua Jiang, Qian Niu, and Jun-Ren Shi, *Topological invariants of metals and the related physical effects*, Chin. Phys. Lett. **30**, 027101 (2013).

[70] J. Ma and D. A. Pesin, *Chiral magnetic effect and natural optical activity in metals with or without Weyl points*, Phys. Rev. B **92**, 235205 (2015).

[71] Y. Alavirad and J. D. Sau, *Role of boundary conditions, topology, and disorder in the chiral magnetic effect in Weyl semimetals*, Phys. Rev. B **94**, 115160 (2016).

[72] S. Zhong, J. E. Moore, and I. Souza, *Gyrotropic magnetic effect and the magnetic moment on the Fermi surface*, Phys. Rev. Lett. **116**, 077201 (2016).

[73] P. Baireuther, J. A. Hutasoit, J Tworzydło, and C. W. J. Beenakker, *Scattering theory of the chiral magnetic effect in a Weyl semimetal: interplay of bulk Weyl cones and surface Fermi arcs*, New J. Phys. **18**, 045009 (2016).

[74] M. A. Zubkov, *Absence of equilibrium chiral magnetic effect*, Phys. Rev. D **93**, 105036 (2016).

[75] G. E. Volovik, *Chiral vortical effect generated by chiral anomaly in vortex-skyrmions*, JETP Lett. **105**, 303 (2017).

[76] T. Meng and J. C. Budich, *Unpaired Weyl nodes from long-ranged interactions: Fate of quantum anomalies*, Phys. Rev. Lett. **122**, 046402 (2019).

[77] D. Kharzeev, *The Chiral Magnetic Effect and anomaly-induced transport*, Progr. Part. Nucl. Phys. **75**, 133 (2014).

[78] A. A. Burkov, *Chiral anomaly and transport in Weyl metals*, J. Phys. Condens. Matter **27**, 113201 (2015).

[79] L. S. Levitov, Yu. V. Nazarov, and G. M. Eliashberg, *Magnetostatics of superconductors without an inversion center*, JETP Lett. **41**, 445 (1985).

[80] Yu. V. Nazarov, *Instability due to magnetically induced currents*, Sov. Phys. JETP **64**, 193 (1986).

[81] A. A. Burkov and L. Balents, *Weyl semimetal in a topological insulator multilayer*, Phys. Rev. Lett. **107**, 127205 (2011).

[82] M. Tinkham, *Introduction to Superconductivity* (Dover Publications, 2004).

[83] G. Lemut, M. J. Pacholski, I. Adagideli, and C. W. J. Beenakker, *Effect of charge renormalization on electric and thermo-electric transport along the vortex lattice of a Weyl superconductor*, Phys. Rev. B **100**, 035417 (2019).

[84] T. Schuster, T. Iadecola, C. Chamon, R. Jackiw, S.-Y. Pi, *Dissipationless conductance in a topological coaxial cable*, Phys. Rev. B **94**, 115110 (2016).

[85] G. E. Volovik, *Quantum phase transitions from topology in momentum space*, Lect. Notes Phys. **718**, 31 (2007).

[86] D. F. Agterberg, P. M. R. Brydon, and C. Timm, *Bogoliubov Fermi surfaces in superconductors with broken time-reversal symmetry*, Phys. Rev. Lett. **118**, 127001 (2017).

[87] Noah F. Q. Yuan and Liang Fu, *Zeeman-induced gapless superconductivity with a partial Fermi surface*, Phys. Rev. B **97**, 115139 (2018).

[88] S. Autti, J. T. Mäkinen, J. Rysti, G. E. Volovik, V. V. Zavjalov, and V. B. Eltsov, *Exceeding the Landau speed limit with topological Bogoliubov Fermi surfaces*, Phys. Rev. Res. **2**, 033013 (2020).

[89] J. M. Link and I. F. Herbut, *Bogoliubov-Fermi surfaces in noncentrosymmetric multi-component superconductors*, Phys. Rev. Lett. **125**, 237004 (2020).

[90] S. Rachel, L. Fritz, and M. Vojta, *Landau levels of Majorana fermions in a spin liquid*, Phys. Rev. Lett. **116**, 167201 (2016).

[91] B. Perreault, S. Rachel, F. J. Burnell, and J. Knolle, *Majorana Landau-level Raman spectroscopy*, Phys. Rev. B **95**, 184429 (2017).

[92] R. Jackiw and P. Rossi, *Zero modes of the vortex-fermion system*, Nucl. Phys. B **190**, 681 (1981).

[93] B. Sutherland, *Localization of electronic wave functions due to local topology*, Phys. Rev. B **34**, 5208 (1986).

[94] V. M. Pereira, F. Guinea, J. M. B. Lopes-dos Santos, N. M. R. Peres, and A. H. Castro-Neto, *Disorder induced localized states in graphene*, Phys. Rev. Lett. **96**, 036801 (2006).

[95] Wen-Yu Shan, Hai-Zhou Lu, and Shun-Qing Shen, *Effective continuous model for surface states and thin films of three-dimensional topological insulators*, New J. Phys. **12**, 043048 (2010).

[96] Song-Bo Zhang, Hai-Zhou Lu, and Shun-Qing Shen, *Edge states and integer quantum Hall effect in topological insulator thin films*, Scientif. Rep. **5**, 13277 (2015).

[97] Hao-Hua Sun and Jin-Feng Jia, *Detection of Majorana zero mode in the vortex*, npj Quantum Mat. **2**, 34 (2017).

[98] S. Cho, B. Dellabetta, A. Yang, J. Schneeloch, Z. Xu, T. Valla, G. Gu, M. J. Gilbert, and N. Mason, *Symmetry protected Josephson supercurrents in three-dimensional topological insulators*, Nature Comm. **4**, 1689 (2013).

[99] D. I. Pikulin and M. Franz, *Black hole on a chip: proposal for a physical realization of the SYK model in a solid-state system*, Phys. Rev. X **7**, 031006 (2017).

[100] H. B. Nielsen and M. Ninomiya, *A no-go theorem for regularizing chiral fermions*, Phys. Lett. B **105**, 219 (1981).

[101] M. Z. Hasan and C. L. Kane, *Topological insulators*, Rev. Mod. Phys. **82**, 3045 (2010).

[102] X.-L. Qi and S.-C. Zhang, *Topological insulators and superconductors*, Rev. Mod. Phys. **83**, 1057 (2011).

[103] J. B. Kogut, *The lattice gauge theory approach to quantum chromodynamics*, Rev. Mod. Phys. **55**, 775 (1983).

[104] D. B. Kaplan, *Chiral symmetry and lattice fermions*, Lecture Notes of the Les Houches Summer School, vol. 93 (2009).

[105] J. Tworzydło, C. W. Groth, and C. W. J. Beenakker, *Finite difference method for transport properties of massless Dirac fermions*, Phys. Rev. B **78**, 235438 (2008).

[106] M. V. Medvedyeva, J. Tworzydło, and C. W. J. Beenakker, *Effective mass and tricritical point for lattice fermions localized by a random mass*, Phys. Rev. B **81**, 214203 (2010).

[107] M. F. Borunda, J. Berezovsky, R. M. Westervelt, and E. J. Heller, *Imaging universal conductance fluctuations in graphene*, ACS Nano **5**, 3622 (2011).

[108] A. R. Hernández and C. H. Lewenkopf, *Finite-difference method for transport of two-dimensional massless Dirac fermions in a ribbon geometry*, Phys. Rev. B **86**, 155439 (2012).

[109] S. D. Drell, M. Weinstein, and S. Yankielowicz, *Strong-coupling field theories. II. Fermions and gauge fields on a lattice*, Phys. Rev. D **14**, 1627 (1976).

[110] R. Stacey, *Eliminating lattice fermion doubling*, Phys. Rev. D **26**, 468 (1982).

[111] K. G. Wilson, *Confinement of quarks*, Phys. Rev. D **10**, 2445 (1974).

[112] L. Susskind, *Lattice fermions*, Phys. Rev. D **16**, 3031 (1977).

[113] F. Evers and A. D. Mirlin, *Anderson transitions*, Rev. Mod. Phys. **80**, 1355 (2008).

[114] T. C. Lang and A. M. Läuchli, *Quantum Monte Carlo simulation of the chiral Heisenberg Gross-Neveu-Yukawa phase transition with a single Dirac cone*, Phys. Rev. Lett. **123**, 137602 (2019).

[115] Y.-F. Zhou, H. Jiang, X. C. Xie, and Q.-F. Sun, *Two- dimensional lattice model for the surface states of topological insulators*, Phys. Rev. B **95**, 245137 (2017).

[116] P. H. Ginsparg and K. G. Wilson, *A remnant of chiral symmetry on the lattice*, Phys. Rev. D **25**, 2649 (1982).

[117] B. Messias de Resende, F. Crasto de Lima, R. H. Miwa, E. Vernek, and G. J. Ferreira, *Confinement and fermion doubling problem in Dirac-like Hamiltonians*, Phys. Rev. B **96**, 161113(R) (2017).

[118] A. L. Araújo, R. P. Maciel, R. G. F. Dornelas, and G. J. Ferreira, *Interplay between boundary conditions and Wilson's mass in Dirac-like Hamiltonians*, Phys. Rev. B **100**, 205111 (2019).

[119] R. Hammer, W. Pötz, and A. Arnold, *A dispersion and norm preserving finite difference scheme with transparent boundary conditions for the Dirac equation in (1+1)D*, J. Comp. Phys. **256**, 728 (2014).

[120] R. Hammer, W. Pötz, and A. Arnold, *Single-cone real-space finite difference scheme for the time-dependent Dirac equation*, J. Comp. Phys. **265**, 50 (2014).

[121] R. Hammer and W. Pötz, *Dynamics of domain-wall Dirac fermions on a topological insulator: A chiral fermion beam splitter*, Phys. Rev. B **88**, 235119 (2013).

[122] W. Pötz, *Single-cone finite-difference schemes for the (2+1)-dimensional Dirac equation in general electromagnetic textures*, Phys. Rev. E **96**, 053312 (2017).

[123] C. M. Bender, K. A. Milton, and D. H. Sharp, *Consistent formulation of fermions on a Minkowski lattice*, Phys. Rev. Lett. **51**, 1815 (1983).

[124] G. Peters and J. H. Wilkinson, *$Ax = \lambda Bx$ and the generalized eigenproblem*, SIAM J. Numer. Anal. **7**, 479 (1970).

[125] S. McCormick, *A mesh refinement method for* $Ax = \lambda Bx$, Math. Comp. **36**, 485 (1981).

[126] N. Read and D. Green, *Paired states of fermions in two dimensions with breaking of parity and time-reversal symmetries and the fractional quantum Hall effect*, Phys. Rev. B **61**, 10267 (2000).

[127] A. Mildenberger, F. Evers, A. D. Mirlin, and J. T. Chalker, *Density of quasiparticle states for a two-dimensional disordered system: Metallic, insulating, and critical behavior in the class-D thermal quantum Hall effect*, Phys. Rev. B **75**, 245321 (2007).

[128] M. Wimmer, A. R. Akhmerov, M. V. Medvedyeva, J. Tworzydło, and C. W. J. Beenakker, *Majorana bound states without vortices in topological superconductors with electrostatic defects*, Phys. Rev. Lett. **105** , 046803 (2010).

[129] M. L. Mehta, *Random Matrices* (Academic Press, 2004).

[130] D. A. Ivanov, *The supersymmetric technique for random-matrix ensembles with zero eigenvalues*, J. Math. Phys. **43**, 126 (2002).

[131] R. Hammer and W. Pötz, *Staggered grid leap-frog scheme for the (2+1)D Dirac equation*, Comp. Phys. Comm. **185**, 40 (2014).

Samenvatting

Landau-niveaus zijn quantumtoestanden die ontstaan uit de periodieke cyclotronbeweging in een magnetisch veld van geladen deeltjes, zoals elektronen. De Landau-niveaus zijn verantwoordelijk voor bijzondere verschijnselen in de vaste stof, zoals het quantum-Hall-effect in twee-dimensionale halfgeleiders en het chirale magnetische effect in Weyl halfmetalen. Deze verschijnselen zijn interessant omdat zij een topologische oorsprong hebben.

Al zo'n dertig jaar geleden vroegen onderzoekers van het kaliber van Anderson, Schrieffer en Gorkov zich af of Landau-niveaux zouden kunnen optreden in supergeleiders, in het bijzonder in de hoge-temperatuur supergeleiders. Een supergeleider probeert het magnetisch veld buiten te dringen (het zogenaamde Meissner-effect), maar in de hoge-temperatuur supergeleiders kan het magneetveld toch binnendringen via wervelingen ("vortices"). Deze onderzoekslijn heeft niets opgeleverd, omdat al snel bleek dat die wervelingen de elektronen sterk verstrooien en de Landau-niveaux compleet tenietdoen.

De belangrijkste bijdrage van dit proefschrift is de ontdekking dat de Landau-niveaux wel stabiel blijven als de geladen deeltjes een zogenaamde chirale symmetrie bezitten. De chirale symmetrie beschermt de Landau-niveaux voor de verstoring door de wervelingen. Omdat de bescherming een gevolg is van een wiskundige stelling uit de topologie (het Atiyah-Singer indextheorema), spreken we van een topologische bescherming.

We onderzoeken twee type deeltjes met chirale symmetrie, die voorkomen in een Weyl supergeleider (hoofdstuk 2) en in een Fu-Kane supergeleider (hoofdstuk 5). In beide gevallen gaat het om massaloze deeltjes, in de Weyl supergeleider bewegen ze zich in drie dimensies, in de Fu-Kane supergeleider slechts in twee dimensies (namelijk aan het oppervlak van een topologische isolator).

De aanwezigheid van Landau-niveaus geeft aanleiding tot supergeleidende analogiën van het quantum-Hall-effect en het chirale magnetische effect, zoals we beschrijven in hoofdstukken 3 en 4. Een onverwachte ontdekking is dat er een elektrische stroom kan optreden die parallel loopt aan het magnetische veld, met een waarde die gekwantiseerd is. Deze stroom ontstaat zonder dat er een elektrisch veld aan te pas komt, het is een puur evenwichtsverschijnsel. Dit is een markante tegenstelling met het

bekende chirale magnetische effect, wat alleen buiten evenwicht optreedt.

In hoofdstuk 6 nemen we een zijspoor, door een meer technisch probleem op te lossen: de computersimulatie van massaloze deeltjes (Dirac fermionen) op een rooster. We ontwikkelen een methode om het welbekende verdubbelingsprobleem te omzeilen (het probleem dat de discretisatie van een differentiaalvergelijking op een rooster een verdubbeling van de massaloze deeltjes veroorzaakt). De methode maakt het mogelijk om de massaloze deeltjes die in de overige hoofdstukken van het proefschrift optreden op een computer te simuleren.

Summary

Landau levels are quantum states originating from the periodic cyclotron motion of charged particles, in particular electrons, in the magnetic field. They occur in a multitude of materials, leading to phenomena such as the quantum Hall effect in two-dimensional systems, and the chiral magnetic effect in Weyl semimetals. These effects are of interest, as they constitute a manifestation of topology in condensed matter systems.

Some thirty years ago, the physicists Anderson, Schrieffer and Gor'kov proposed that Landau levels could appear in superconductors, in particular in the high-temperature superconductors. A superconductor tries to expel the magnetic field (the so-called Meissner effect), but in high-temperature superconductors the field can still penetrate in the form of vortices. This proposal led nowhere, because it was soon understood that the vortices will strongly scatter the electrons, thereby fully destroying the Landau levels.

The main contribution of this thesis is the discovery that the Landau levels do remain stable if the charged particles have a so-called chiral symmetry. The chiral symmetry protects the Landau levels from the scattering by vortices. Because the protection is a consequence of a mathematical theorem in topology (the Atiyah-Singer index theorem), one speaks of a topological protection.

We investigate two types of particles with chiral symmetry, which appear in a Weyl superconductor (chapter 2) and in a Fu-Kane superconductor (chapter 5). In both systems these are massless particles, in the Weyl superconductor they move in three dimensions, in the Fu-Kane superconductor in two dimensions (on the surface of a topological insulator).

The presence of Landau levels gives rise to superconducting counterparts of the quantum Hall effect and the chiral magnetic effect, as we describe in chapters 3 and 4. An unexpected finding is the appearance of an electrical current parallel to the magnetic field, with a quantized magnitude. This current exists in the absence of any electric field, it is purely an equilibrium effect. All of this is marked contrast with the known chiral magnetic effect, which only exists out of equilibrium.

Chapter 6 diverges from the topics discussed above, by solving a more technical problem: the computer simulation of massless particles (Dirac

fermions) on a lattice. We develop a method to avoid the well known fermion doubling problem (the problem that the discretization of a differential equation on a lattice causes a doubling of the massless particles). This method makes it possible to simulate on a computer the massless particles studied in the other chapters of the thesis.

Curriculum Vitæ

I was born on 23rd of June 1993, in Otwock, Poland. Most of my youth I lived in Marki, where I attended the primary school. There I became interested in programming, which was a passion that I developed further in Władysław IV Secondary School in Warsaw, becoming a laureate of several national competitions. After graduating, I continued my education in Stanisław Staszic High School in Warsaw, where my main focus became physics. I obtained the laureate title of the national Physics Olympiad three times, having finished first and third on two of the occasions. This allowed me to participate in the International Physics Olympiads, in which I won a gold and a bronze medal.

In 2012 I entered the individual program of the bachelor's studies in physics at the University of Warsaw, in which I graduated with distinction in 2014 with a thesis titled *Electronic, magnetic and transport properties of zigzag graphene nanoribbon p–n junctions* under the supervision of professor Jacek Majewski. I continued my education on the master's program in physics at the same university, graduating with distinction in 2017 with a thesis *Thermal conduction and shot noise of Majorana surface states*, under the supervision of professor Jakub Tworzydło. During my studies I did a month-long internship in CERN within the COMPASS experiment. I also participated in the International Physicists' Tournament, in which our team earned the second place twice.

In 2017 I began my PhD studies at the Instituut-Lorentz of Leiden University in the Netherlands, under the supervision of professor Carlo Beenakker. My research was focused on the properties of topological materials, in particular Weyl and p-wave superconductors. I have attended several international schools and conferences, during which I had the opportunity to present the results of my research both orally and in a poster. During my studies I assisted with courses in Quantum Theory and Quantum Information, for which I was awarded the Teaching Assistant Prize.

After receiving my PhD diploma, I plan to continue my career in physics, studying further implications of the findings described in this thesis, as well as other novel phenomena in condensed matter.

List of publications

- N. V. Gnezdilov, M. Diez, M. J. Pacholski, and C. W. J. Beenakker, *Wiedemann-Franz-type relation between shot noise and thermal conduction of Majorana surface states in a three-dimensional topological superconductor*, Physical Review B **94**, 115415 (2016).

- M. J. Pacholski, C. W. J. Beenakker, and İ. Adagideli, *Topologically protected Landau level in the vortex lattice of a Weyl superconductor*, Physical Review Letters **121**, 037701 (2018). [Chapter 2]

- G. Lemut, M. J. Pacholski, İ. Adagideli, and C. W. J. Beenakker, *Effect of charge renormalization on the electric and thermoelectric transport along the vortex lattice of a Weyl superconductor*, Physical Review B **100**, 035417 (2019). [Chapter 3]

- İ. Adagideli, F. Hassler, A. Grabsch, M. J. Pacholski, and C. W. J. Beenakker, *Time-resolved electrical detection of chiral edge vortex braiding*, SciPost Physics **8**, 013 (2020).

- G. Lemut, M. J. Pacholski, O. Ovdat, A. Grabsch, J. Tworzydło, and C. W. J. Beenakker, *Localization landscape for Dirac fermions*, Physical Review B **101**, 081405 (2020).

- M. J. Pacholski, C. W. J. Beenakker, İ. Adagideli, *Universal chiral magnetic effect in the vortex lattice of a Weyl superconductor*, Annals of Physics **417**, 168103 (2020). [Chapter 4]

- F. Hassler, A. Grabsch, M. J. Pacholski, D. O. Oriekhov, O. Ovdat, İ. Adagideli, and C. W. J. Beenakker, *Half-integer charge injection by a Josephson junction without excess noise*, Physical Review B **102**, 045431 (2020).

- G. Lemut, A. Donís Vela, M. J. Pacholski, J. Tworzydło, and C. W. J. Beenakker, *Magnetic breakdown spectrum of a Kramers-Weyl semimetal*, New Journal of Physics **22**, 093022 (2020).

- M. J. Pacholski, G. Lemut, O. Ovdat, İ. Adagideli, and C. W. J. Beenakker, *Deconfinement of Majorana vortex modes produces a superconducting Landau level*, Physical Review Letters **126**, 226801 (2021). [Chapter 5]
- M. J. Pacholski, G. Lemut, J. Tworzydło, and C. W. J. Beenakker, *Generalized eigenproblem without fermion doubling for Dirac fermions on a lattice*, arXiv:2103.15615 (2021). [Chapter 6]
- A. Donís Vela, G. Lemut, M. J. Pacholski, C. W. J. Beenakker, *Chirality inversion of Majorana edge modes in a Fu-Kane heterostructure*, arXiv:2105.04433 (2021).
- G. Lemut, M. J. Pacholski, C. W. J. Beenakker, *Chiral charge transfer along magnetic field lines in a Weyl superconductor*, arXiv:2106.12327 (2021).